Study of charmonium decays to $K^0_S K\pi$ in the $B \to (K^0_S K\pi)K$ channels

R. Aaij *et al.*[*]
(LHCb Collaboration)

(Received 5 May 2023; accepted 27 June 2023; published 17 August 2023)

A study of the $B^+ \to K^0_S K^+ K^- \pi^+$ and $B^+ \to K^0_S K^+ K^+ \pi^-$ decays is performed using proton-proton collisions at center-of-mass energies of 7, 8 and 13 TeV at the LHCb experiment. The $K^0_S K\pi$ invariant mass spectra from both decay modes reveal a rich content of charmonium resonances. New precise measurements of the η_c and $\eta_c(2S)$ resonance parameters are performed and branching fraction measurements are obtained for B^+ decays to η_c, J/ψ, $\eta_c(2S)$ and χ_{c1} resonances. In particular, the first observation and branching fraction measurement of $B^+ \to \chi_{c0} K^0 \pi^+$ is reported as well as first measurements of the $B^+ \to K^0 K^+ K^- \pi^+$ and $B^+ \to K^0 K^+ K^+ \pi^-$ branching fractions. Dalitz plot analyses of $\eta_c \to K^0_S K\pi$ and $\eta_c(2S) \to K^0_S K\pi$ decays are performed. A new measurement of the amplitude and phase of the $K\pi$ S-wave as functions of the $K\pi$ mass is performed, together with measurements of the $K^*_0(1430)$, $K^*_0(1950)$ and $a_0(1700)$ parameters. Finally, the branching fractions of χ_{c1} decays to K^* resonances are also measured.

DOI: 10.1103/PhysRevD.108.032010

I. INTRODUCTION

Understanding strong interaction effects in exclusive weak decays of heavy hadrons is of importance to gain information on fundamental aspects of the phenomenology of strong and weak interactions. In two-body nonleptonic decays such as $B \to (\bar{c}c)K$, a simple factorization method has been adopted to compute nonleptonic decay amplitudes [1]. The method involves expressing the hadronic matrix elements of four-quark operators in the effective Hamiltonian inducing the decay as the product of two matrix elements of quark currents. It has been successful, such as in the description of the $B \to \eta_c K$ and $J/\psi K$ decays [2]. However, it clearly misses important effects, since it fails to describe the $B \to \chi_{c0} K$ mode. Indeed, in this mode the factorized amplitude involves the matrix element of the $(\bar{c}c)_{V,A}$ vector (V) and axial (A) currents between the vacuum and χ_{c0} resonance, which vanishes due to charmed vector current conservation and parity conservation. In contrast, the measured $B \to \chi_{c0} K$ branching fraction is sizable [3], clearly indicating that the nonfactorizable part of the amplitude plays an important role [4]. Additional observations of new $B \to \chi_{c0} X$ decay modes are therefore of interest.

The only established strange scalar meson is the $K^*_0(1430)$ resonance, whose parameters are yet to be precisely measured [3]. Scalar resonances decaying to $K\pi$ are particularly interesting, since many amplitude analyses of heavy-flavor decays involve a $K\pi$ system [5], whose theoretical description is a source of large systematic uncertainty. A widely used method of modeling the $K\pi$ S-wave relies on the results from Ref. [6], which consists of a large threshold enhancement described by a scattering length term and a relativistic Breit-Wigner (BW) function describing the $K^*_0(1430)$ resonance. A similar behavior is observed in the $K\pi$ S-wave measured in D^+ decays [7–9]. Still unresolved is the possible existence of a broad scalar resonance, $\kappa/K^*_0(700)$, claimed by several experiments [3]; its existence would suggest the possible presence of tetraquark states in the light meson system [10].

Further information has been obtained from the Dalitz plot analysis of η_c decays to $K\bar{K}\pi$ with the η_c meson produced in two-photon interactions, and in an extended $K\pi$ mass region [11]. Due to its large width, the description of the line shape of the $K^*_0(1430)$ resonance could be complicated by the effects of the opening of the $K\eta$ and $K\eta'$ thresholds. The decay of the $K^*_0(1430)$ resonance to $K\eta$ has been observed in a Dalitz-plot analysis of $\eta_c \to K^+ K^- \eta$ [12], and its branching fraction has been found to be small. Its decay to $K\eta'$ has been observed in Refs. [13,14]. Another resonance, $K^*_0(1950)$, seen in the $K\pi$ decay mode [6], is still to be confirmed. Evidence for the $K^*_0(1950) \to K\eta'$ decay mode has been found in a Dalitz-plot analysis of $\eta_c \to K^+ K^- \eta'$ decays [14].

In the Dalitz-plot analysis of the $\eta_c \to \eta\pi^+\pi^-$ decay, a new $a_0(1700)$ resonance has been observed in the $\eta\pi$ mass

[*]Full author list given at the end of the article.

spectrum [14] and recently confirmed in the $a_0(1700) \to K^0_S K$ decay mode [15]. The $a_0(1700)$ decay to $K^0_S K$ is therefore expected to contribute to $\eta_c/\eta_c(2S) \to K^0_S K\pi$ decays. To date, no Dalitz-plot analysis of $\eta_c(2S)$ has been performed.

The $\chi_{c1} \to K^0_S K\pi$ decay has been studied in Ref. [16] in $\psi(2S) \to \gamma K^0_S K\pi$ decays with 220 ± 16 events and a low background. By fitting to the $K\pi$ mass projections, partial branching fractions to K^* resonances have been measured. Given the small dataset, only upper limits have been obtained for some $\chi_{c1} \to K^* X$ decay modes, and therefore further measurements of these branching fractions are useful.

The $B^+ \to K^0_S K^+ K^- \pi^+$ and $B^+ \to K^0_S K^+ K^+ \pi^-$ decays have been previously studied in Refs. [17,18], but their branching fractions are yet to be measured. New large datasets may therefore help in clarifying several of the above-listed issues related to light-meson spectroscopy and B to charmonium decays.

This paper is organized as follows: Sec. II describes the LHCb detector; Sec. III, the signal candidate selection procedure; Sec. IV, the study of various mass spectra; Sec. V, the measurement of the charmonium-resonance parameters; Sec. VI, the efficiency evaluation; Secs. VII and VIII, the Dalitz plot analysis of the η_c and $\eta_c(2S)$ mesons, respectively; Sec. IX, the study of χ_{c1} decays; and Sec. X, the measurements of various branching fractions. Finally, Sec. XI summarizes the results.

II. DETECTOR, SIMULATION AND ANALYSIS

The LHCb detector [19,20] is a single-arm forward spectrometer covering the pseudorapidity range $2 < \eta < 5$, designed for the study of particles containing b or c quarks. The detector elements that are particularly relevant to this analysis are these: a silicon-strip vertex detector (VELO) [21] surrounding the pp interaction region that allows c and b hadrons to be identified from their characteristically long flight distance; a tracking system that provides a measurement of the momentum, p, of charged particles; and two ring-imaging Cherenkov detectors that are able to discriminate between different species of charged hadrons. Muons are identified by a system composed of alternating layers of iron and multiwire proportional chambers. The entire dataset collected with the LHCb experiment during runs 1 and 2 is used, corresponding to center-of-mass energies $\sqrt{s} = 7$, 8 and 13 TeV and comprising an integrated luminosity of 9 fb^{-1}. The online event selection starts with a trigger [22], which consists of a hardware stage, based on information from the calorimeter and muon systems, followed by a software stage, which applies a full event reconstruction. During offline selection, trigger signatures are associated with reconstructed particles. Since the trigger system uses the transverse momentum of the charged particles with respect to the beam axis, p_T, the phase-space and time acceptance is different for events where signal tracks were involved in the trigger decision (called trigger on signal or TOS throughout) and those where the trigger decision was made using information from the rest of the event only (no TOS). Data from both trigger conditions are used and studied separately for consistency tests and the evaluation of systematic uncertainties.

Simulation is required to model the effects of the detector acceptance and the imposed selection requirements. In the simulation, pp collisions are generated using PYTHIA [23] with a specific LHCb configuration [24]. Decays of unstable particles are described by EvtGen [25], in which final-state radiation is generated using PHOTOS [26]. The interaction of the generated particles with the detector, and its response, are implemented using the Geant4 toolkit [27] as described in Ref. [28].

Two types of simulations are performed: (1) where the B^+ is decayed according to a phase-space model and (2) where the B^+ decays as $B^+ \to (c\bar{c})K$, where $(c\bar{c})$ indicates a charmonium resonance decaying to $K^0_S K\pi$ by phase space.

III. EVENT SELECTION

The present work reports a study of the two B^+ decays[1]

$$B^+ \to K^0_S K^- K^+ \pi^+ \tag{1}$$

and

$$B^+ \to K^0_S K^+ K^+ \pi^-, \tag{2}$$

with $K^0_S \to \pi^+\pi^-$. Decays of the K^0_S are reconstructed in two categories: the first involving K^0_S mesons that decay early enough for the pions to be reconstructed inside the VELO; and the second containing K^0_S mesons that decay later such that track segments from the pions are outside the VELO. These categories are referred to as long K^0_S (indicated in the following with $K^0_{\rm SLL}$) and downstream K^0_S (indicated in the following with $K^0_{\rm SDD}$), respectively. While the $K^0_{\rm SLL}$ category has better mass, momentum and vertex resolution, there are approximately twice as many $K^0_{\rm SDD}$ candidates. Candidate B^+ particles are formed by combining the K^0_S candidate with three other charged tracks, having a total charge of one, performing a global vertex fit to the decay tree and requiring the B^+ candidate to originate from one of the primary pp collision vertices in the event. Selection criteria and efficiency measurements are performed separately for each K^0_S category. To suppress backgrounds, in particular combinatorial background formed from random combinations of unrelated tracks, the events satisfying the trigger requirements are filtered by

[1]The inclusion of charge-conjugate processes is implied throughout the paper.

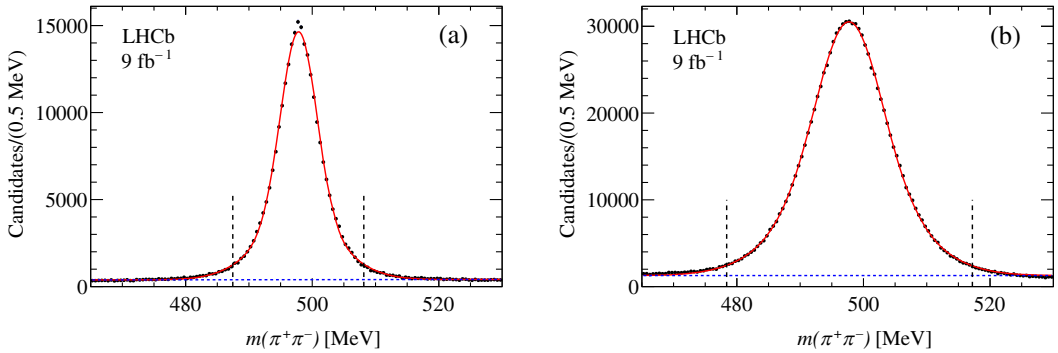

FIG. 1. Invariant $\pi^+\pi^-$ mass distribution for (a) $K^0_{\rm SLL}$ and (b) $K^0_{\rm SDD}$ candidates. The full (red) line indicates the fit results and the dashed (blue) line the background contribution. The vertical dashed lines indicate the region used to select the K^0_S signal.

a loose preselection, followed by a multivariate selection optimized separately for each data sample. Selection requirements are tuned to minimize correlation of the signal efficiency with kinematic variables, resulting in better control of the corresponding systematic uncertainties. Consequently, the selection relies minimally on the kinematics of the final-state particles and instead exploits the topological features that arise from the detached vertex of the B^+ candidate. These include the following: the impact parameters of the B^+ candidate and its decay products, the quality of the decay vertices of the B^+ and K^0_S candidates and the separation of these vertices from each other and from the primary vertex.

The preselection of K^0_S and B^+ candidates requires, for each track, the presence of appropriate particle identification (PID) information and imposes invariant mass selections around the known K^0_S and B^+ particle masses. The separation of signal from combinatorial background is achieved by means of a boosted decision tree (BDT) classifier [29,30], implemented using the TMVA toolkit [31]. The multivariate classifier chosen for this analysis is a BDT with a gradient boosting algorithm [32], separated for $K^0_{\rm SLL}$ and $K^0_{\rm SDD}$ data. The classifiers are trained using simulated signal decays, composed of samples (a) and (b) described in Sec. II with proportions corresponding to the resonance composition observed in the data (see Sec. IV). The simulation also matches the relative proportions of the dataset at the various center-of-mass energies. It is assumed that the efficiencies for the reconstruction of the decays displayed in Eqs. (1) and (2) are the same. For the background input to the training, data in the lower and upper sidebands of the B^+ signal region are used. The composition of the background sample reflects the data-taking conditions and the decays in Eqs. (1) and (2) are used in equal proportions.

The optimization of the BDT classifier working point is performed by scanning the figure of merit

$$S = \frac{N_{\rm sig}}{\sqrt{N_{\rm sig} + N_{\rm bkg}}}, \tag{3}$$

where $N_{\rm sig}$ ($N_{\rm bkg}$) represents the signal (combinatorial background) yield in the signal region. The yields are evaluated in a $\pm 2.5\sigma$ window around the B^+ mass, where σ is the mass resolution, through fits to the $K^0_S K^+K^-\pi$ mass spectra using two Gaussian functions sharing the same mean for the signal and a linear function for the background. Figure 1 shows the $\pi^+\pi^-$ invariant-mass distributions at the K^0_S candidate vertex, separated for $K^0_{\rm SLL}$ and $K^0_{\rm SDD}$, after selecting candidates using the optimized figure of merit S defined in Eq. (3).

The two $\pi^+\pi^-$ invariant mass distributions are fitted using the sum of two Gaussian functions sharing the same mean, with σ_1 and σ_2 resolutions, and a linear function for the background. An effective resolution is computed as $\sigma = f\sigma_1 + (1-f)\sigma_2$ where f is the fraction of the first Gaussian contribution. The resulting effective resolutions for the LL and DD categories are $\sigma_{\rm LL} = 2.53$ MeV and $\sigma_{\rm DD} = 6.46$ MeV. The K^0_S signals are selected within 3.0σ of the fitted K^0_S mass of 497.8 MeV.[2]

In order to facilitate the extraction of the B^+ and K^0_S signal and combinatorial background components from these invariant-mass spectra, no kinematic mass constraint is applied to the K^0_S and B^+ signals. To improve the mass resolution (see Sec. IV A), the energy of the selected candidate K^0_S is computed as

$$E_{K^0_S} = \sqrt{p^2_{K^0_S} + m^2_{K^0_S}}, \tag{4}$$

where $p_{K^0_S}$ is the reconstructed K^0_S momentum and $m_{K^0_S}$ the known K^0_S mass. Compared with the resolution obtained from the use of the K^0_S mass constraint, this method gives the same resolution for the $K^0_S KK\pi$ invariant mass and a slightly worse resolution, by ≈6%, for the $K^0_S K\pi$ invariant mass.

Particle identification of the three charged hadrons is performed using the output of a probabilistic neural

[2]Natural units with $\hbar = c = 1$ are used throughout this paper.

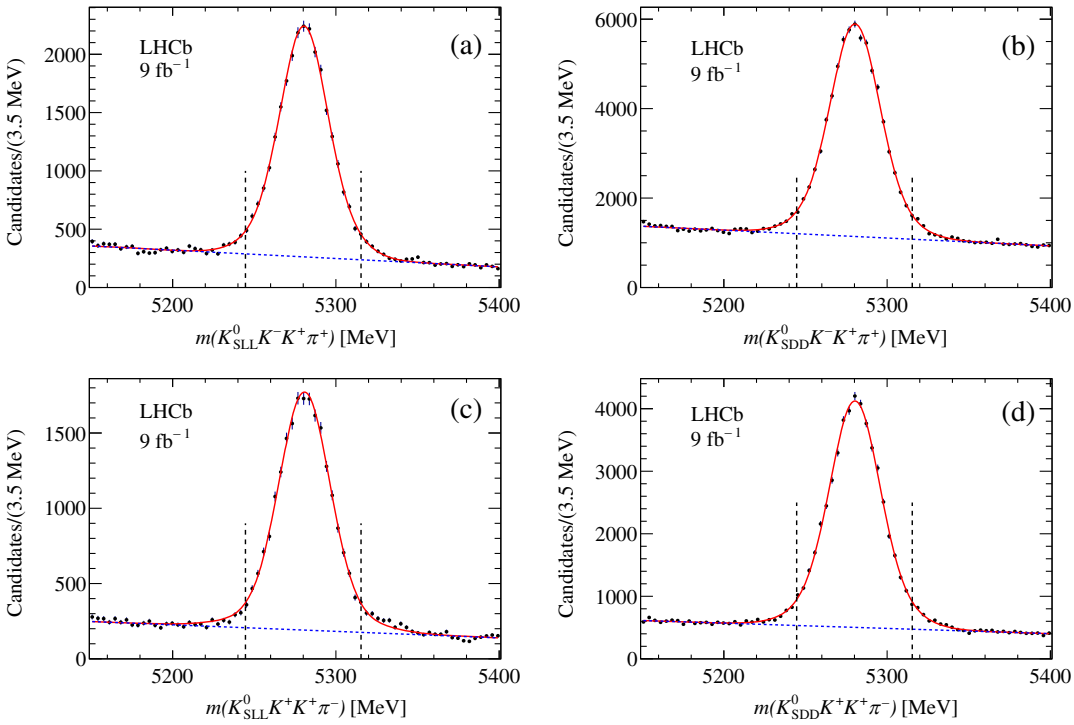

FIG. 2. Distributions of $K^0_S K^+K^-\pi^+$ invariant mass for (a) K^0_{SLL} and (b) K^0_{SDD} candidates and distributions of $K^0_S K^+K^+\pi^-$ invariant mass for (c) K^0_{SLL} and (d) K^0_{SDD} candidates. The full (red) lines indicate the signal component and the dashed (blue) lines the background. The vertical dashed lines indicate the regions used to select the B^+ signals.

network (NN) trained on the output of all the subdetectors. The figures of merit are expressed as $P_K = NN_K(1-NN_\pi)$ for kaon identification and $P_\pi = NN_\pi(1-NN_K)$ for pion identification, where NN_π and NN_K are the NN probabilities for pion and kaon identification, respectively. Thresholds are applied to these quantities to maximize the significance of the B^+ -candidate invariant-mass peak as a function of P_K or P_π.

Open charm production in the B^+ decays is significant, with the presence of several signals of D^+, D^0 and D_s^+ in two-body and three-body mass combinations. The largest contributions are due to $D^0 \to K^0_S K^+K^-$ decays in $B^+ \to K^0_S K^+K^-\pi^+$ decays $(17.4 \pm 0.2)\%$ and $\bar{D}^0 \to K^+\pi^-$ decays $(6.4 \pm 0.1)\%$ in $B^+ \to K^0_S K^+K^+\pi^-$ decays. As both D^0 signals have large signal to background ratios, they are removed from the B^+ -candidate samples. The $D^0 \to K^0_S K^+K^-$ contribution is removed by requiring $|m - m_0| > 3.5\sigma$, where m indicates the $K^0_S K^+K^-$ invariant mass, with $m_0 = 1864.6$ MeV and $\sigma = 4.5$ MeV for K^0_{SLL} data and $\sigma = 6.3$ MeV for K^0_{SDD} data. The background from $\bar{D}^0 \to K^+\pi^-$ decays is removed by requiring $|m - m_0| > 3.5\sigma$, where m indicates the $K^+\pi^-$ mass, with $m_0 = 1864.5$ MeV and $\sigma = 8.4$ MeV. In both cases the D^0 parameters are extracted from a fit to the data, using a Gaussian function and a linear polynomial for signal and background, respectively.

Figure 2 shows the $K^0_S K^+K^-\pi^+$ and $K^0_S K^+K^+\pi^-$ invariant mass spectra, after the optimized offline selection requirements, separated by K^0_S category. The distributions are fitted to a sum of two Gaussian functions sharing the same mean values and a linear background function. The fits give an average B^+ -mass value of 5280 MeV and an average width of $\sigma = 17.7$ MeV. Signal candidates are selected in a window of $\pm 2\sigma$ of the fitted B^+ mass, common to the four datasets. Table I lists the fitted yields and purities (P) in the B^+ signal region for the different datasets, where the purity is defined as $P = N_{\rm sig}/(N_{\rm sig} + N_{\rm bkg})$. The dependence of P on the collision energy and data-taking conditions is approximately uniform for all the four datasets, simplifying the Dalitz-plot analyses reported in the following. Approximately

TABLE I. Fitted B^+ signal yield and purity for $B^+ \to K^0_S K^+K^-\pi^+$ and $B^+ \to K^0_S K^+K^+\pi^-$ final states separated by K^0_S type.

Final state	B^+ signal yield	B^+ purity [%]
$K^0_S K^+K^-\pi^+$		
K^0_{SLL}	21460 ± 220	80.0 ± 0.2
K^0_{SDD}	52690 ± 420	69.5 ± 0.2
$K^0_S K^+K^+\pi^-$		
K^0_{SLL}	17730 ± 220	82.0 ± 0.3
K^0_{SDD}	40730 ± 320	79.9 ± 0.2

0.02% of events contain multiple B^+ decay candidates, as selected with the above procedure, and therefore their effect is considered negligible. An inspection of the $\pi^+\pi^-$ mass spectra for $K^0_{\rm SLL}$ and $K^0_{\rm SDD}$ candidates after all selections, and in the B^+ signal region, shows K^0_S signals with negligible background.

IV. MASS SPECTRA

The $K^0_S K\pi$ invariant-mass spectra for events in the B^+ signal region, summed over the $K^0_{\rm SLL}$ and $K^0_{\rm SDD}$ datasets, are shown in Fig. 3 for $B^+ \to K^0_S K^+ K^- \pi^+$ and $B^+ \to K^0_S K^+ K^+ \pi^-$ final states. The lower and upper mass sidebands around the B^+ signal peak are defined in the ranges $[-6\sigma, -4\sigma]$ and $[4\sigma, 6\sigma]$, respectively, with $\sigma = 17.7$ MeV. The corresponding $K^0_S K\pi$ invariant mass spectra, representative of background candidates, are superimposed onto the $K^0_S K\pi$ invariant mass spectrum from the B^+ signal region. The $B^+ \to K^0_S K^+ K^+ \pi^-$ final state has two kaons with the same charge and therefore both combinations are included in the $K^0_S K\pi$ invariant-mass spectrum.

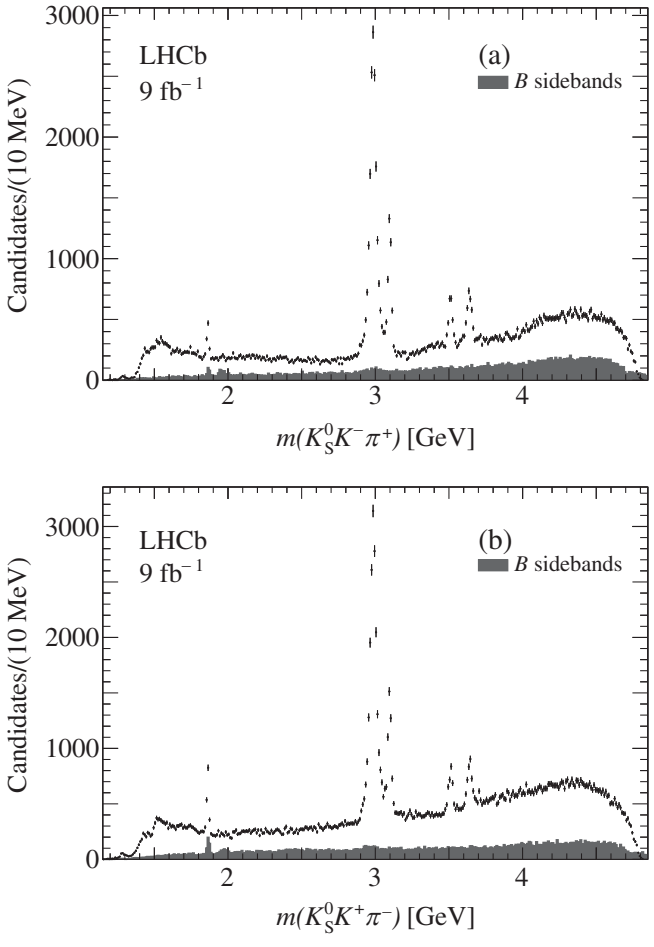

FIG. 3. Invariant $K^0_S K\pi$ mass distributions for (a) $B^+ \to K^0_S K^+ K^- \pi^+$ and (b) $B^+ \to K^0_S K^+ K^+ \pi^-$ candidates (two entries per event).

There are 119,198 entries and 159,694 combinations in the $K^0_S K\pi$ invariant mass spectra from the two B^+ decay modes, respectively. The $K^0_S K\pi$ invariant-mass distributions show a signal at threshold in the position of the $f_1(1285)$ resonance and a broad complex structure in the 1.5 GeV mass region. A $D^0 \to K^0_S K\pi$ signal can be observed, due to the open-charm final state $B^+ \to \bar{D}^0 K^+$. Prominent signals of η_c, J/ψ, χ_{c1}, and $\eta_c(2S)$ can be observed in both invariant-mass spectra. A broad enhancement in the η_c mass region is present in the $K^0_S K\pi$ mass spectrum from B^+ sidebands. The effect can be understood as due to the presence of prompt $\eta_c \to K^0_S K\pi$ decays [33] reconstructed using an incorrect decay chain. The structure above 1.9 GeV that appears mostly in the sidebands is due to the reflection from $D^0 \to K^0_S \pi^+ \pi^-$ decays, where one pion is misidentified as a kaon. The strong η_c signal present in the data allows for a test of the agreement between data and simulation for the PID. PID is removed for each final-state kaon and pion in turn on both data and simulation, and the η_c event losses due to the kaon (3%) and the pion (0.4%) identification are compared. The results for data and simulation agree within 2σ and this effect is therefore ignored.

A. Mass resolution

The mass resolution is obtained from simulated data. In this analysis it is used to perform fits to the invariant-mass spectra and obtain resonance parameters in which the effects of the mass resolution are expected to be significant, in particular in fitting narrow charmonium states. As the resolution functions are mass dependent, they are evaluated in specific mass intervals, namely the η_c–J/ψ mass region, defined in the [2.90–3.15] GeV region, and the χ_{c1}–$\eta_c(2S)$ mass region, defined in the $[3.46 - 3.70]$ GeV region. Due to the presence of two types of reconstructed K^0_S with different resolutions, the mass resolution is computed separately for $K^0_{\rm SLL}$ and $K^0_{\rm SDD}$ data. The resulting mass-difference distributions are well described by the sum of a Gaussian and a crystal ball function. The width (σ) of the dominant Gaussian contribution is 8.8 MeV (9.9 MeV) in the η_c–J/ψ mass region and 10.3 MeV (12.0 MeV) in the χ_{c1}–$\eta_c(2S)$ mass region for the $K^0_{\rm SLL}$ ($K^0_{\rm SDD}$) data.

V. MEASUREMENT OF CHARMONIUM-RESONANCE PARAMETERS

The measurements of charmonium-resonance parameters are performed with binned fits to the $K^0_S K\pi$ invariant-mass spectra separately in the η_c–J/ψ and the χ_{c1}–$\eta_c(2S)$ mass regions in the ranges shown in Figs. 4 and 5, respectively. In both invariant-mass regions, the $B^+ \to K^0_S K^+ K^- \pi^+$ and $B^+ \to K^0_S K^+ K^+ \pi^-$ data are fitted separately. Since the experimental resolutions for $K^0_{\rm SLL}$ and $K^0_{\rm SDD}$ data are different, a simultaneous fit to the two

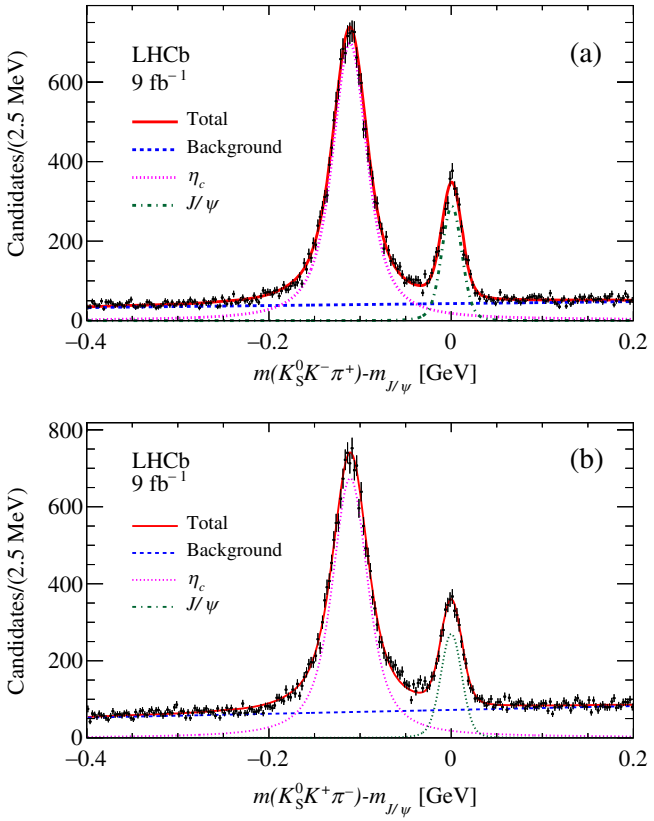

FIG. 4. Invariant $K^0_S K\pi$ invariant mass distributions, with the known J/ψ mass subtracted, in the η_c–J/ψ mass region for (a) $B^+ \to K^0_S K^+ K^- \pi^+$ and (b) $B^+ \to K^0_S K^+ K^+ \pi^-$ candidates. The results of the fits are overlayed.

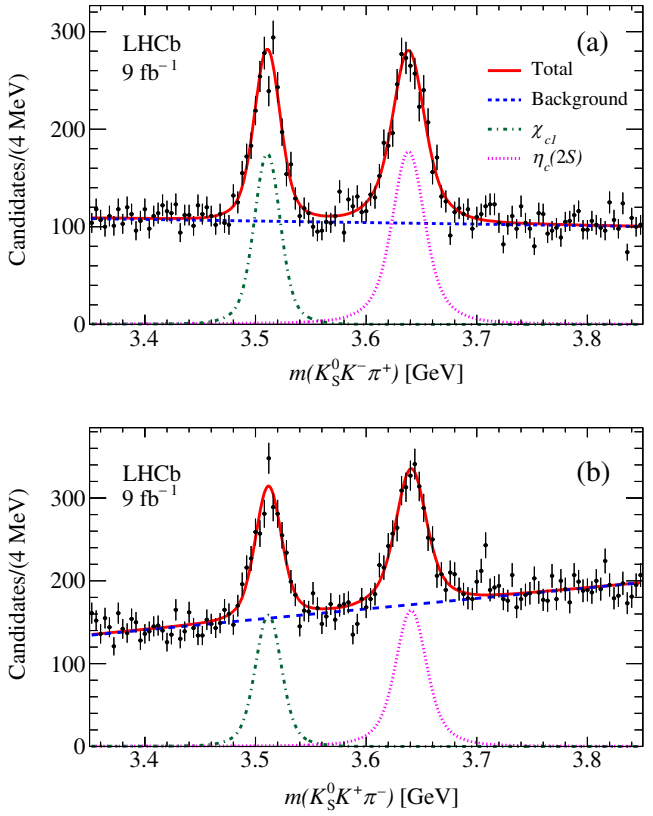

FIG. 5. Invariant $K^0_S K\pi$ mass distributions in the χ_{c1}–$\eta_c(2S)$ mass region for (a) $B^+ \to K^0_S K^+ K^- \pi^+$ and (b) $B^+ \to K^0_S K^+ K^+ \pi^-$ candidates. The results of the fits are overlayed.

invariant-mass spectra is performed, sharing only the resonance parameters. In the fit to the η_c–J/ψ mass region, the J/ψ width is fixed to the known value [3] and the $K^0_S K\pi$ mass value is shifted by the J/ψ mass: $m' = m - m_{J/\psi}$, where $m_{J/\psi}$ is fixed to the known value [3]. Here, all resonances are described by simple nonrelativistic BW functions

$$BW(m) = \frac{1}{(m_0 - m) - i\Gamma/2}, \tag{5}$$

convolved with the appropriate mass resolution functions. The backgrounds, which are due to a combination of $B \to K^0_S KK\pi$ decays and incoherent $K^0_S K\pi$ production, are represented by first-order polynomials. Table II lists the fitted resonance parameters and yields, together with fit p values. A comparison with PDG [3] averages shows improvements both in the mass and width of the η_c resonance, with the J/ψ mass in good agreement with the known value. A small negative shift, consistent with zero, can be seen on the fitted J/ψ mass. The good description of the J/ψ line shape, whose observed width is dominated by the mass resolution, demonstrates the good agreement of the mass resolution in data and simulation.

Systematic uncertainties include the following sources. The bin width is varied from 2.5 to 3.0 MeV and the background shape is changed from linear to a second-order polynomial. The η_c component is allowed to interfere with the background that has a significant contribution from the B^+ decay. The interference is parametrized as

$$f(m) = |A_{\rm nres}|^2 + |A_{\rm res}|^2 + c \cdot 2\,{\rm Re}(A_{\rm nres} A^*_{\rm res}), \tag{6}$$

where $A_{\rm nres}$ is the nonresonant amplitude and $|A_{\rm nres}|^2$ is described by a linear function. The resonant contribution is constructed as $A_{\rm res} = \alpha \cdot {\rm BW}(m) \cdot \exp(i\phi)$, where α and ϕ are free parameters and BW(m) is the Breit-Wigner function of Eq. (5) describing the η_c line shape convolved with the experimental resolution. The coherence factor, c, is a free parameter. It is found that the interference model produces a small improvement in the description of the data with fitted phases of $\phi = 1.596 \pm 0.009$ rad and $\phi = 1.631 \pm 0.011$ rad, both close to $\pi/2$, for $B^+ \to K^0_S K^+ K^- \pi^+$ and $B^+ \to K^0_S K^+ K^+ \pi^-$ data, respectively. The deviations of the fitted resonance parameters from those obtained without interference are included as systematic uncertainties.

TABLE II. Fitted η_c, J/ψ, $\eta_c(2S)$, and χ_{c1} parameters. For the J/ψ the $m' = m - m_{J/\psi}$ value is reported. The first uncertainty is statistical, the second systematic.

Final state	p-value [%]	Resonance	Mass [MeV]	Width [MeV]	Yield
$K^0_S K^+ K^- \pi^+$	16.3	η_c	$2984.84 \pm 0.23 \pm 1.01$	$30.0 \pm 0.7 \pm 0.2$	17700 ± 190
		J/ψ	$-0.27 \pm 0.11 \pm 0.61$	0.0929 (fixed)	3386 ± 70
$K^0_S K^+ K^+ \pi^-$	1.5	η_c	$2985.19 \pm 0.24 \pm 1.88$	$29.4 \pm 0.8 \pm 0.8$	17210 ± 210
		J/ψ	$-0.81 \pm 0.11 \pm 0.67$		3310 ± 80
Average		η_c	$2985.01 \pm 0.17 \pm 0.89$	$29.7 \pm 0.5 \pm 0.2$	
		J/ψ	$-0.54 \pm 0.08 \pm 0.45$		
$K^0_S K^+ K^- \pi^+$	46.6	$\eta_c(2S)$	$3636.92 \pm 0.71 \pm 1.50$	$11.70 \pm 2.04 \pm 1.39$	1960 ± 80
		χ_{c1}	$3509.32 \pm 0.70 \pm 0.84$	0.88 (fixed)	1300 ± 50
$K^0_S K^+ K^+ \pi^-$	5.3	$\eta_c(2S)$	$3639.28 \pm 0.84 \pm 3.83$	$9.18 \pm 2.67 \pm 1.70$	1720 ± 100
		χ_{c1}	$3510.35 \pm 0.69 \pm 1.00$		1460 ± 70
Average		$\eta_c(2S)$	$3637.90 \pm 0.54 \pm 1.40$	$10.77 \pm 1.62 \pm 1.08$	
		χ_{c1}	$3509.84 \pm 0.69 \pm 0.64$		

The systematic uncertainty associated with the background model is evaluated by varying the BDT classifier selection working point, resulting in a variation of the B^+ purity of around $\pm 5\%$. The average value of the absolute values of the two resulting variations of the resonance parameters is used to quantify the systematic uncertainty associated to the background level. Starting with the fitted functions from the reference fit, 400 pseudoexperiments are generated and fitted. The average value of the deviations of the fitted parameters is included as a systematic uncertainty.

TABLE III. Summary of systematic uncertainties on J/ψ and η_c resonance parameters.

Contribution	$m(\eta_c)$ [MeV]	$\Gamma(\eta_c)$ [MeV]	$\Delta m(J/\psi)$ [MeV]
$B^+ \to K^0_S K^+ K^- \pi^+$			
Bin width	0.03	0.12	0.08
Background	0.04	0.01	0.01
Interference	0.84	0.09	0.15
Fit bias	0.01	0.02	0.04
Momentum scale	0.56		0.56
BDT variation	0.07	0.12	0.16
Resolution	0.00	0.01	0.00
Squared sum	1.01	0.19	0.61
$B^+ \to K^0_S K^+ K^+ \pi^-$			
Bin width	0.02	0.01	0.03
Background	0.11	0.09	0.05
Interference	1.79	0.74	0.36
Fit bias	0.00	0.09	0.07
Momentum scale	0.56		0.56
BDT variation	0.10	0.06	0.05
Resolution	0.00	0.01	0.00
Squared sum	1.88	0.75	0.67

The momentum-scale uncertainty is evaluated as $0.03Q$ [34], where Q is evaluated as the difference between the η_c mass and the sum of the masses of the decay particles. The uncertainties on the resonance parameters arising from the limited sizes of the simulation samples, used to obtain the resolution functions, are obtained by fitting the $K^0_S K\pi$ invariant-mass spectrum from 400 pseudoexperiments where, in each fit, all the parameters describing the resolution functions are varied randomly from a Gaussian distribution defined by their statistical uncertainties. Table III gives the resulting contributions to the systematic uncertainties which are then added in quadrature.

A similar model is used to fit the χ_{c1}–$\eta_c(2S)$ mass region, shown in Fig. 5, with the fit results summarized in Table II together with the inverse-variance-weighted averages of the fitted parameters from the two B^+ decay modes. In this case, the χ_{c1} width is fixed to the known value [3]. The inverse-variance method is also used, here and in the following, to evaluate average systematic uncertainties. A comparison of the results listed in Table II with PDG [3] measurements shows improvements both in the mass and width of the $\eta_c(2S)$ resonance, with the χ_{c1} mass in good agreement with the known value. Systematic uncertainties on the fit parameters are evaluated in a similar way as for the η_c–J/ψ fit except now the $\eta_c(2S)$ is allowed to interfere with the background. The fit with interference returns relative phases of $\phi = 1.52 \pm 0.05$ rad and $\phi = 1.82 \pm 0.09$ rad for the $B^+ \to K^0_S K^+ K^- \pi^+$ and $B^+ \to K^0_S K^+ K^+ \pi^-$ final states, respectively (similarly close to $\pi/2$). The presence of signals corresponding to the $h_c(1P)$ and $\chi_{c2}(1P)$ resonances is explored by adding additional components to the fit function and resonance parameters fixed to the known values [3]; their yields are found to be consistent with zero. A summary of the systematic uncertainties, together with their quadratic sum, is given in Table IV.

TABLE IV. List of the systematic uncertainties on the χ_{c1} and $\eta_c(2S)$ parameters.

Final state	$m(\eta_c(2S))$ [MeV]	$\Gamma(\eta_c(2S))$ [MeV]	$m(\chi_{c1})$ [MeV]
$B^+ \to K^0_S K^+ K^- \pi^+$			
Bin width	0.13	0.17	0.09
Background	0.01	0.99	0.05
Interference	1.30	0.09	0.29
Fit bias	0.02	0.22	0.00
Momentum scale	0.75		0.75
BDT variation	0.09	0.93	0.25
Squared sum	1.50	1.39	0.84
$B^+ \to K^0_S K^+ K^+ \pi^-$			
Bin width	0.22	0.15	0.10
Background	0.14	1.15	0.09
Interference	3.75	0.70	0.64
Fit bias	0.05	0.55	0.04
Momentum scale	0.75		0.75
BDT variation	0.10	0.87	0.11
Squared sum	3.83	1.70	1.00

A. First observation of $B^+ \to \chi_{c0} K^0_S \pi^+$

Figure 6 shows the K^+K^- invariant-mass spectrum for $B^+ \to K^0_S K^+ K^- \pi^+$ candidates in the χ_{c0}–χ_{c2} mass region, where a prominent χ_{c0} signal can be seen, together with a weaker signal at the χ_{c2} mass. Also superimposed is the K^+K^- invariant-mass spectrum from the B^+ sidebands, where no χ_{c0} signal can be seen. For this B^+ decay mode, the PDG [3] reports a branching-fraction upper limit of $\mathcal{B}(B^+ \to \chi_{c0} K^*) < 2.1 \times 10^{-4}$ [35].

Using a similar method as for the fit to the other charmonium resonances, a simultaneous binned fit of the K^+K^- mass spectrum for the $K^0_{\rm SLL}$ and $K^0_{\rm SDD}$ data is performed. The background is parametrized by a second-order polynomial; the resonance parameters for the χ_{c0} state are unconstrained, while those for the χ_{c2} component are fixed to their known values. The χ_{c0} signal is described by the relativistic spin-0 Breit-Wigner function

$$BW(m) = \frac{1}{m_0^2 - m^2 - i m_0 \Gamma}, \tag{7}$$

where m_0 is the resonance mass. The mass dependent width Γ is written as

$$\Gamma = \Gamma_0 \frac{q}{q_0} \frac{m_0}{m}, \tag{8}$$

where Γ_0 is the resonance width and q (q_0) is the momentum of either decay particle in the two-body (resonance) rest frame. The χ_{c2} signal, due to its narrow width, is described by a simple Breit-Wigner function [Eq. (5)]; both distributions are convolved with the experimental resolution function modeled, as described in Sec. IV A, by the sum of a crystal ball function and a Gaussian function having $\sigma = 11.9$ MeV. In this fit, the measured χ_{c0} mass and width are both shifted by approximately 5 MeV with respect to their known values [3].

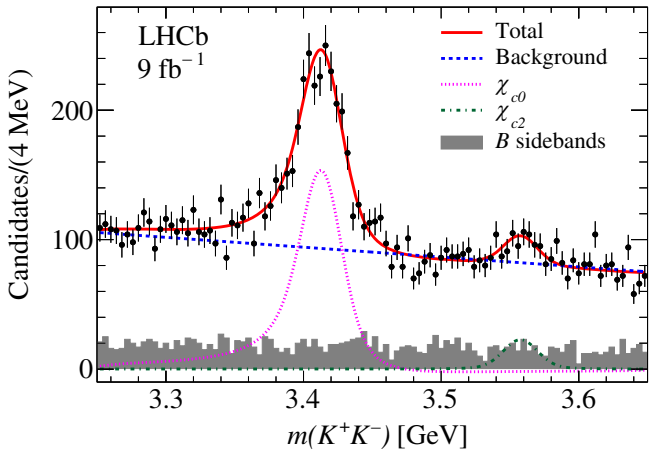

FIG. 6. Invariant K^+K^- mass distribution in the $\chi_{c0} - \chi_{c2}$ mass region for $B^+ \to K^0_S K^+ K^- \pi^+$ decays. The two K^0_S datasets are combined. The results of the fit are overlayed. The curves also include interference terms and therefore the χ_{c0} line shape takes slightly negative values.

Allowing for interference of the χ_{c0} resonance with a nonresonant K^+K^- component, as described in Eq. (6), results in the data description shown in Fig. 6, with a p value $= 27.9\%$ and χ_{c0} parameters

$$\begin{aligned} m(\chi_{c0}) &= 3413.6 \pm 1.3 \text{ MeV}, \\ \Gamma(\chi_{c0}) &= 12.8 \pm 2.8 \text{ MeV}, \end{aligned} \tag{9}$$

consistent with PDG averages [3]. The χ_{c0} yield is $N_{\chi_{c0}} = 1920 \pm 90$ and the relative phase $\phi = -1.290 \pm 0.073$ rad. The fit also returns a χ_{c2} yield of $N_{\chi_{c2}} = 190 \pm 30$. To evaluate the significance of the χ_{c2} signal, a fit without its contribution is performed. This results in a χ^2 variation of $\Delta\chi^2 = 22.5$ for the difference of one parameter, which gives a statistical significance of 4.6σ.

VI. EFFICIENCY

Two types of efficiencies are evaluated, total and local. The total efficiency describes the effects of the reconstruction on the B^+ decay to the 4-body final state, needed to evaluate the relative charmonium branching fractions. The local efficiencies are evaluated in specific $K^0_S K\pi$ mass regions, i.e. the η_c–J/ψ and χ_{c1}–$\eta_c(2S)$ mass regions, where Dalitz-plot analyses are performed and descriptions of the $K^0_S K\pi$ detection efficiency are needed. The efficiencies are evaluated by generating simulation samples that undergo the same reconstruction and analysis selections as the data. The efficiency is evaluated as the

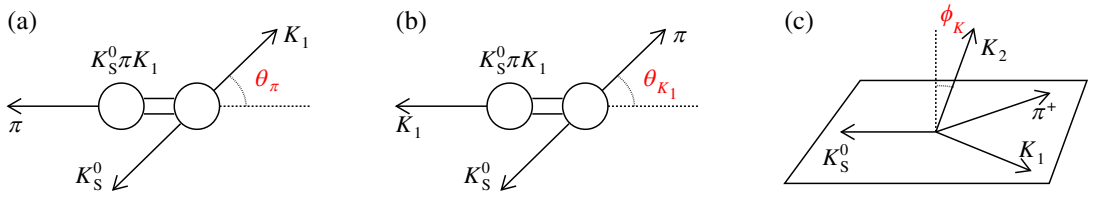

FIG. 7. Definition of the angles (a) θ_π, (b) θ_{K_1}, and (c) ϕ_K.

ratio of selected over generated distributions projected over the relevant kinematic variables.

The choice of the phase-space variables which describe the efficiency is somewhat arbitrary, and a mixture of two-body and three-body invariant-mass projections is used, together with variables related to the angular distributions. A comparison between the p_T distributions of the B^+ candidates in simulated samples and in data shows a small disagreement, which is corrected by weighting the former to match the latter.

A. Total efficiency

To study efficiencies, simulated events are generated according to a four-body phase-space model. Since the physics of the $K^0_S K\pi$ system is of interest, the charged kaon participating in the decay under study is labeled K_1, while the second charged kaon behaves as a spectator and is labeled K_2. Therefore, the reaction can be written

$$B \to (K^0_S K_1 \pi) K_2. \tag{10}$$

Only $B^+ \to K^0_S K^+ K^- \pi^+$ decays are generated because the efficiency for $B^+ \to K^0_S K^+ K^+ \pi^-$ is expected to be the same. The generated angular distributions are all uniform; therefore, any observed variation is due to inefficiency. The efficiencies are evaluated separately for the $K^0_{\rm SLL}$ and $K^0_{\rm SDD}$ samples. In both cases the resulting distributions have only a mild dependence on the $K^0_S K\pi$ invariant mass.

The kinematics of a four-body decay are fully described by five independent variables. Different invariant-mass combinations have different kinematic bounds, so mass-reduced variables are used instead because they always range between 0 and 1. They are defined as [36]

$$m_x = \frac{1}{\pi}\arccos\left(2\frac{m - m_{\rm min}}{m_{\rm max} - m_{\rm min}} - 1\right), \tag{11}$$

where m, $m_{\rm min}$ and $m_{\rm max}$ indicate the invariant mass and its minimum and maximum kinematically allowed values, respectively. As an example in the above equation, $m_x(K^0_S K)$ for the three-body $K^0_S K\pi$ system is computed as

$$m_x(K^0_S K) = \frac{1}{\pi}\arccos\left(2\frac{m(K^0_S K) - m_{\rm min}}{m_{\rm max} - m_{\rm min}} - 1\right), \tag{12}$$

and $m_{\rm min} = m_{K^0_S} + m_K$ and $m_{\rm max} = m(K^0_S K\pi) - m_\pi$, similarly for other two-body mass combinations. The angular distributions make use of helicity angles defined as follows. In the $K^0_S K\pi$ rest frame, shown in Figs. 7(a) and 7(b), θ_π (θ_{K_1}) indicates the angle formed by the K_1 (π) with respect to the $K^0_S K_1$ ($K^0_S\pi$) direction in the $K^0_S K_1$ ($K^0_S\pi$) rest frame. Similarly, the angle θ_{K_2} is defined by exchanging K_1 with K_2. Figure 7(c) shows the definition of ϕ_K, the angle formed by the spectator K_2 with the normal to the $K^0_S K_1\pi$ plane.

The model used to describe the efficiency is obtained in an iterative manner. First, the variables showing the strongest deviation from uniformity in the simulation are chosen. The efficiency projection as a function of the first chosen variable, $m_x(K^0_S K_1)$, is fitted using a seventh-order polynomial labeled as $\epsilon_1(m_x(K^0_S K_1))$. Figure 8 shows the

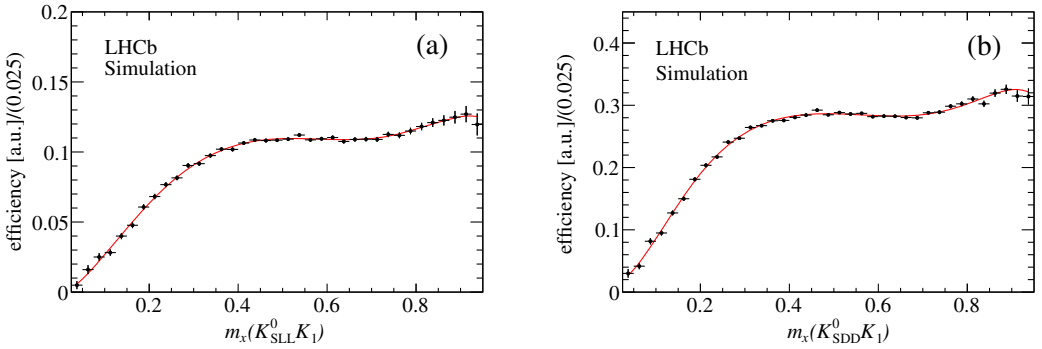

FIG. 8. Efficiency projections (in arbitrary units) on $m_x(K^0_S K_1)$ for the (a) $K^0_{\rm SLL}$ and (b) $K^0_{\rm SDD}$ samples for the total $B^+ \to K^0_S K^+ K^- \pi^+$ dataset. The curves are the results of fits made using seventh-order polynomials.

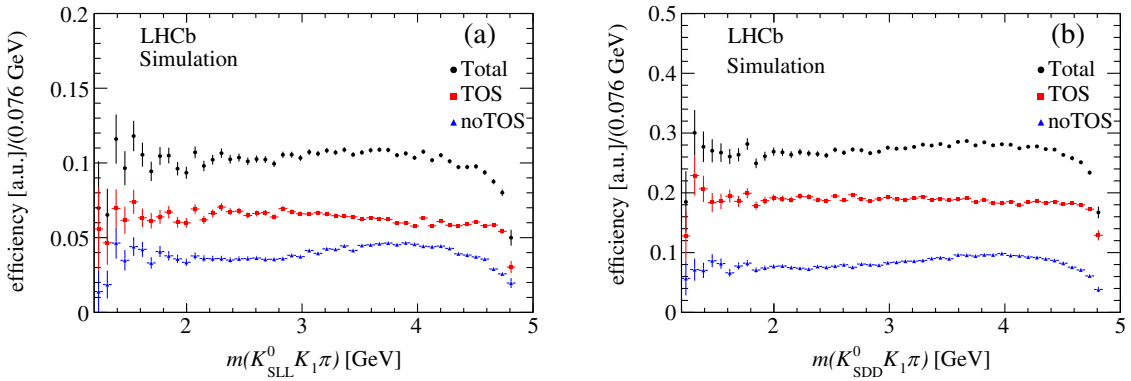

FIG. 9. Efficiency projections (in arbitrary units) on $m(K^0_S K_1\pi)$ for the (a) K^0_{SLL} and (b) K^0_{SDD} simulation samples separated for trigger conditions.

efficiency projected on $m_x(K^0_S K_1)$ separately for the K^0_{SLL} and K^0_{SDD} samples.

The events are then weighted by the inverse of the efficiency $1/\epsilon_1(m_x(K^0_S K_1))$ and a second variable $(m_x(K^0_S\pi))$ is chosen which is itself fitted by a seventh-order polynomial labeled as $\epsilon_2(m_x(K^0_S\pi))$. The events are then weighted by $1/(\epsilon_1(m_x(K^0_S K_1))\cdot\epsilon_2(m_x(K^0_S\pi)))$. The process continues in this fashion, terminating when, after weighting, the efficiency is consistent with being uniform across all the nine considered variables, both on one- and two-dimensional projections. The total efficiency for each K^0_S category, ϵ_{LL} and ϵ_{DD}, is found to be well described by

$$\begin{aligned}\epsilon_{LL} &= \epsilon_1(m_x(K^0_S K_1))\cdot\epsilon_2(m_x(K^0_S\pi))\cdot\epsilon_3(m(K^0_S K_1\pi))\\ &\quad\cdot\epsilon_4(m_x(K_1\pi))\cdot\epsilon_5(\cos\theta_{K_2})),\\ \epsilon_{DD} &= \epsilon_1(m_x(K^0_S K_1))\cdot\epsilon_2(m_x(K^0_S\pi))\cdot\epsilon_3(m(K^0_S K_1\pi))\\ &\quad\cdot\epsilon_4(m_x(K_1\pi)).\end{aligned} \tag{13}$$

1. Efficiency for different trigger conditions

As described in Sec. II, the reconstructed events belong to two trigger categories: TOS and no TOS. Separate efficiencies are needed for each trigger condition, further divided into K^0_{SLL} and K^0_{SDD} categories. Figure 9 shows the efficiency distributions as functions of the $K^0_S K\pi$ invariant mass, separated by trigger condition and K^0_S type. The efficiency evaluations are performed using the same sample of generated events and therefore the scale of the distributions also gives the fraction of the simulation samples belonging to each category. It is found that the efficiency has a weak dependence on $m(K^0_S K_1\pi)$ for all the considered samples.

B. Local efficiencies

1. Efficiency in the η_c–J/ψ and χ_{c1}–$\eta_c(2S)$ mass regions

The efficiency in the η_c–J/ψ mass region is evaluated from a dedicated sample of simulated $B^+\to\eta_c K^+$ decays, where the η_c decays to a $K^0_S K\pi$ state, in which the η_c is generated according to a BW function and decays uniformly in its three-body phase space. These simulations are used to evaluate the efficiency across the Dalitz plot, which can be described in terms of two independent variables, chosen to be $m_x(K^0_S K_1)$ and $\cos\theta_\pi$. Labeling $x = m_x(K^0_S K_1)$ and $y=\cos\theta_\pi$, the efficiency map is smoothed by fitting with a two-dimensional polynomial

$$\begin{aligned}\varepsilon(x,y) = c_0(1 &+ c_1x + c_2y + c_3xy + c_4x^2 + c_5y^2 + c_6x^2y\\ &+ c_7xy^2 + c_8x^3 + c_9y^3 + c_{10}x^4 + c_{11}y^4 + c_{12}x^3y\\ &+ c_{13}x^2y^2 + c_{14}xy^3 + c_{15}x^5 + c_{16}x^6 + c_{17}x^6y),\end{aligned} \tag{14}$$

separately for the K^0_{SLL} and K^0_{SDD} samples. Figure 10 shows the fitted two-dimensional efficiency distributions with the fit projections on $m_x(K^0_S K_1)$ and $\cos\theta_\pi$.

The efficiency in the χ_{c1}–$\eta_c(2S)$ mass region is computed from the sample of simulated $B\to K^0_S KK\pi$ decays by selecting events in the [3.46–3.70] GeV mass region. Due to the size of the simulated sample and because of the weak dependence of the efficiency on $\cos\theta_\pi$, the efficiency model is obtained from fits with seventh-order polynomials to the efficiency projections on $m_x(K^0_S K_1)$ and $\cos\theta_\pi$, as shown in Fig. 11. The efficiency is then parametrized as $\epsilon = \epsilon_1(m_x(K^0_S K_1))\cdot\epsilon_2(\cos\theta_\pi)$.

VII. DALITZ PLOT ANALYSIS OF THE η_c DECAY TO $K^0_S K\pi$

A. Data selection for the $B^+\to K^0_S K^+K^-\pi^+$ final state

This section is devoted to the study of the decay

$$\begin{aligned}B^+ &\to \eta_c K^+,\\ \eta_c &\to K^0_S K^-\pi^+,\end{aligned} \tag{15}$$

where the K^+ meson is considered a spectator. For simplicity here and in the following, kaons are labeled using their charge.

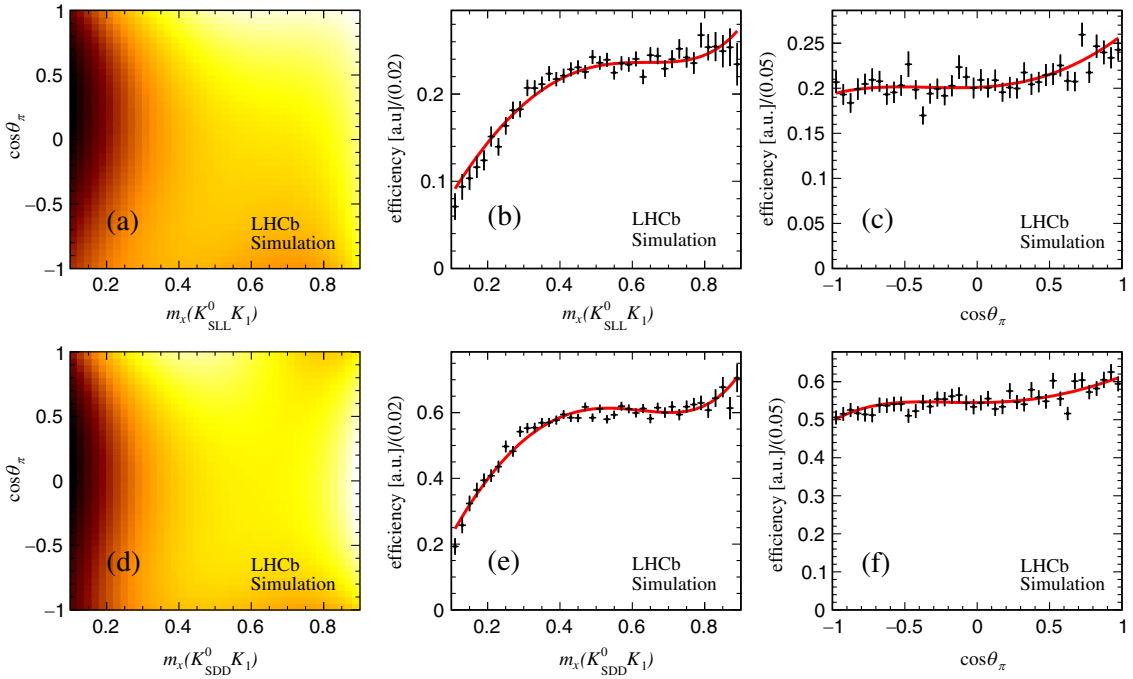

FIG. 10. Two-dimensional efficiency fitted distributions in the η_c mass region for the (a) $K^0_{\rm SLL}$ and (d) $K^0_{\rm SDD}$ samples. Efficiency projections (in arbitrary units) for (b)–(c) $K^0_{\rm SLL}$ and (e)–(f) $K^0_{\rm SDD}$ simulation. The curves are the results from the fits according to Eq. (14).

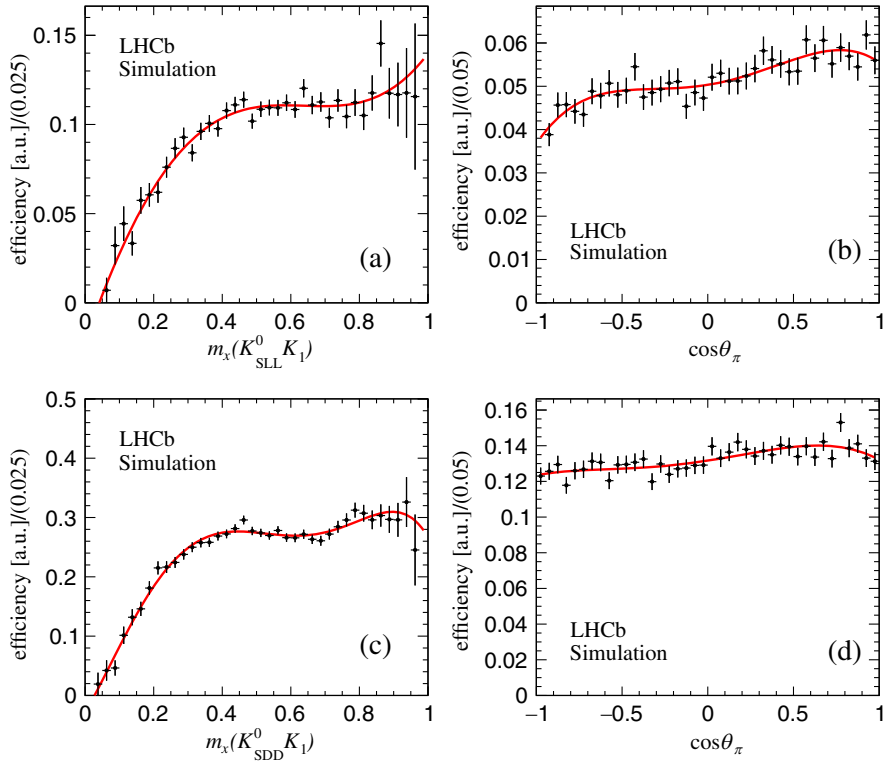

FIG. 11. Efficiency projections (in arbitrary units) in the χ_{c1}–$\eta_c(2S)$ mass region for the (a)–(b) $K^0_{\rm SLL}$ and (c)–(d) $K^0_{\rm SDD}$ simulation. The curves are the results from fits performed using seventh-order polynomials.

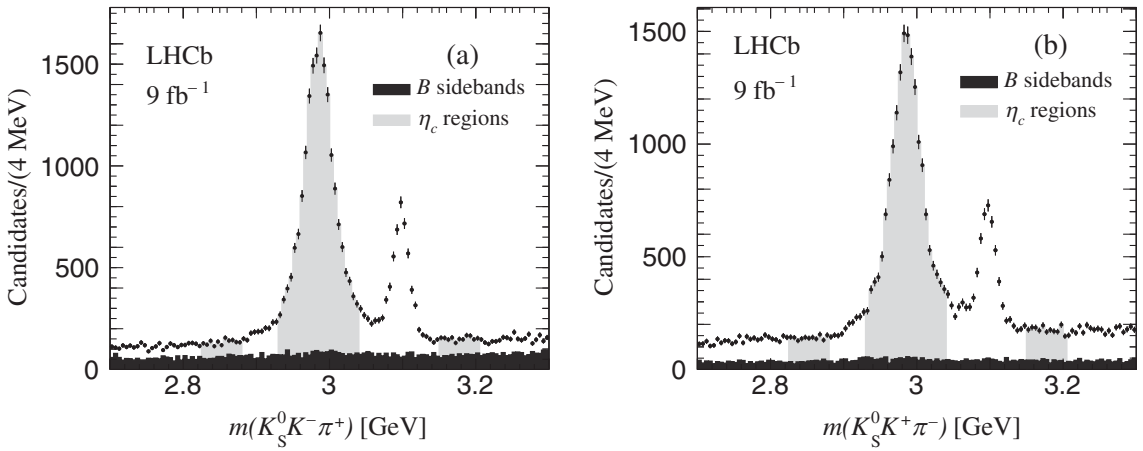

FIG. 12. Invariant $K^0_S K\pi$ mass distributions in the η_c–J/ψ signal region combining the $K^0_{\rm SLL}$ and $K^0_{\rm SDD}$ data for (a) $B^+ \to K^0_S K^+ K^- \pi^+$ and (b) $B^+ \to K^0_S K^+ K^+ \pi^-$ decays. The dark-gray area represents the $K^0_S K\pi$ invariant-mass spectrum from the B^+ sideband; the light-gray areas indicate the η_c signal and sideband regions.

Possible backgrounds originating from charm decays to particles amongst the $\eta_c \to K^0_S K^- \pi^+$ decay products and the spectator K^+ are investigated, and no open charm production is observed in any two-body or three-body mass combinations. The absence of significant structures ensures that the η_c signal is decoupled from the K^+ and the η_c analysis can be considered as a simple study of the three-body η_c decay.

The $\pi^- K^+$ invariant-mass spectrum, where the π^- comes from the K^0_S decay, shows no evidence of a D^0 background. Possible backgrounds from pions misidentified as kaons are considered by assigning the pion mass to each of the two kaons in the final state. Except for the small $D^0 \to K^0_S \pi^+ \pi^-$ signal observed in the B^+ sidebands, discussed in Sec. IV, no charm signal is observed in the resulting two-body or three-body mass combinations. Also, no evidence for the B^+ decay to the $K^0_S K^+ \pi^+ \pi^-$ state is observed.

The η_c signal region is defined as [2.935–3.035] GeV while the sideband regions are defined as [2.83–2.88] GeV and [3.15–3.20] GeV as shown in Fig. 12. The background under the η_c signal peak has two components: (1) from B^+ background, estimated from B^+ sidebands, labeled in the following as incoherent and shown as dark-gray areas in Fig. 12; (2) from B^+ signal, labeled as coherent and indicated by light-gray shading in Fig. 12. The relative fraction of these two components is estimated by integrating the contents of the dark- and light-gray areas in the η_c lower and higher sidebands. The resulting incoherent backgrounds fractions, labeled as f_B, are listed in Table V together with the η_c event yields in the signal region and purities, separated for the $K^0_{\rm SLL}$ and $K^0_{\rm SDD}$ data.

B. Data selection for the $B^+ \to K^0_S K^+ K^+ \pi^-$ final state

This section is devoted to the selection of the decay

$$B^+ \to \eta_c K^+, \quad \eta_c \to K^0_S K^+ \pi^-, \tag{16}$$

where two identical K^+ mesons are present. Because of this, the two K^+ mesons are alternately considered as part of the η_c signal decay or as a spectator to it, and every candidate decay therefore appears twice in the sample under study. This final state is affected by a significant background from $\bar{D}^0 \to K^+ \pi^-$ decays, which is removed as discussed in Sec. III. Labeling the spectator K^+ as K^+_2, the

TABLE V. Candidate events and purities in the η_c signal region and fractions of B^+ sideband contributions in the η_c sideband regions for $B^+ \to K^0_S K^+ K^- \pi^+$ and $B^+ \to K^0_S K^+ K^+ \pi^-$ decays. Low and high indicate the lower and higher sideband candidates. Because of the limited statistics, the values of f_B are summed for the $K^0_{\rm SLL}$ and $K^0_{\rm SDD}$ data.

Final state	K^0_S type	Candidates	Purity [%]	Low f_B [%]	High f_B [%]
$B^+ \to K^0_S K^+ K^- \pi^+$	$K^0_{\rm SLL}$	4622	91.8 ± 0.4		
	$K^0_{\rm SDD}$	11101	89.0 ± 0.3		
	Combined K^0_S			29.6 ± 2.0	31.5 ± 2.0
$B^+ \to K^0_S K^+ K^+ \pi^-$	$K^0_{\rm SLL}$	5034	84.3 ± 0.5		
	$K^0_{\rm SDD}$	11439	83.5 ± 0.3		
	Combined K^0_S			25.5 ± 1.5	22.0 ± 1.2

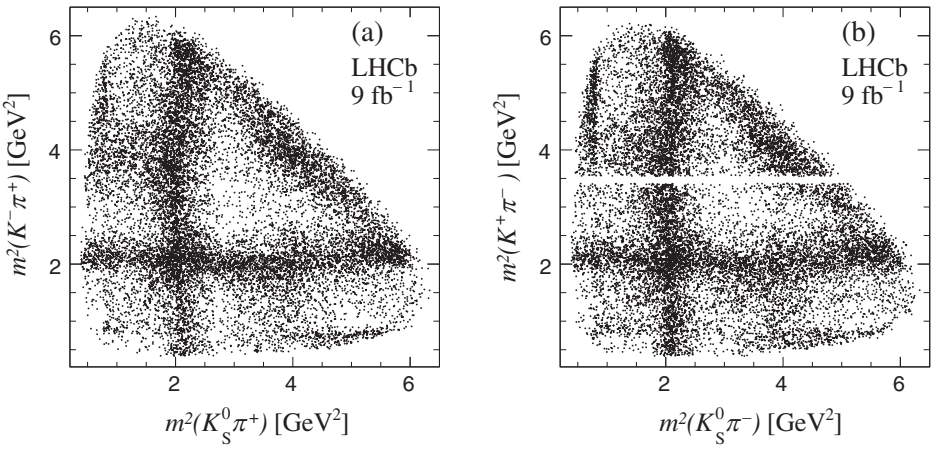

FIG. 13. Dalitz plot of $\eta_c \to K^0_S K\pi$ decays for (a) $B^+ \to K^0_S K^+ K^-\pi^+$ and (b) $K^0_S K^+ K^+\pi^-$. The empty horizontal band in (b) is due to the removal of the $\bar{D}^0 \to K^+\pi^-$ channel.

$K^0_S K^+_2 \pi^-$ invariant-mass spectrum shows a small D^0 signal, and events are removed if they lie within ± 26 MeV of the D^0 mass. No other open-charm signal is observed in other two-body or three-body mass combinations. The $K^0_S K\pi$ mass spectrum is shown in Fig. 12(b) with indications of background, signal and sideband regions. Table V gives information about the event yields, purities and background composition.

C. Dalitz plot analysis

The η_c Dalitz plot is shown in Fig. 13, for (a) $B^+ \to K^0_S K^+ K^-\pi^+$ and (b) $B^+ \to K^0_S K^+ K^+\pi^-$ data. It is dominated by horizontal and vertical bands due to the presence of the $K^*_0(1430)^{+,0}$ resonances.

1. Dalitz plot analysis method

An amplitude analysis of the $K^0_S K\pi$ final state in the η_c mass region is performed, using unbinned maximum-likelihood fits. The likelihood function is written as

$$\mathcal{L} = \prod_{n=1}^{N} \left[P \cdot \epsilon(x'_n, y'_n) \frac{\sum_{i,j} c_i c_j^* A_i(x_n, y_n) A_j^*(x_n, y_n)}{\sum_{i,j} c_i c_j^* I_{A_i A_j^*}} + (1-P) \frac{\sum_i k_i B_i(x_n, y_n)}{\sum_i k_i I_{B_i}} \right], \quad (17)$$

where N is the number of events in the signal region. For the nth event, $x_n = m^2(K^0\pi^+)$ and $y_n = m^2(K^-\pi^+)$. The signal purity (P) is obtained from the fit to the $K^0_S K\pi$ invariant-mass spectrum (see Fig. 4) and listed in Table V. The efficiency $\epsilon(x'_n, y'_n)$ is parametrized as a function of $x'_n = m(K^0_S K)$ and $y'_n = \cos\theta_\pi$ and described in Sec. VI. The complex signal-amplitude contribution for the ith signal component is indicated as $A_i(x_n, y_n)$. The corresponding complex parameter c_i is allowed to vary in the fit, except for the largest amplitude, the $(K\pi$ S-wave$)K$ [labeled in the following as $(K\pi)_S K$] in the quasi-model-independent (QMI) analysis (Sec. VII D) or the $K^*_0(1430)K$ in the isobar model analysis (Sec. VII E), which is taken as the reference, setting the modulus $|c_1| = 1$ and phase $\phi_1 = 0$. The background probability density function for the ith background component is indicated as $B_i(x_n, y_n)$, and it is assumed that interference between signal and background amplitudes can be ignored. The magnitude of the ith background component is indicated by k_i and is obtained by fitting to the sideband regions and interpolating linearly in the signal region. The expressions $I_{A_i A_j^*} = \int A_i(x,y) A_j^*(x,y) \epsilon(x',y') \mathrm{d}x\mathrm{d}y$ and $I_{B_i} = \int B_i(x,y) \mathrm{d}x\mathrm{d}y$ represent normalization integrals for signal and background. Numerical integration is performed on phase-space generated events [37] with η_c signal and background generated according to their experimental distributions. For resonances with free parameters, integrals are recomputed at each minimization step. Integrals corresponding to the background components, and fits involving amplitudes with fixed resonance parameters, are computed only once. Both the K^0_{SLL} and K^0_{SDD} data are included in the likelihood function, each dataset with its own efficiency and purity. The A_i amplitudes are taken from Refs. [38,39]. The standard Blatt-Weisskopf [40] form factors are used at the resonance vertices with radius r fixed to 1.5 GeV^{-1}. The decay of the η_c to $K\bar{K}\pi$ is governed by strong interactions with two allowed processes: $\eta_c \to a_L \pi$ and $\eta_c \to K^*_L \bar{K}$, where a_L indicates an isospin-1 spin-L resonance and K^*_L indicates an isospin-1/2 spin-L resonance. Conservation of G-parity for the $\eta_c \to a_L\pi$ case implies L to be even. For the decay $\eta_c \to K^*_L \bar{K}$, G parity relates the final states $K^*_L \bar{K}$ and $\bar{K}^*_L K$ as $(K^*_L \bar{K} + G \bar{K}^*_L K)/\sqrt{2}$. Since G parity is positive, it follows that in the Dalitz plot, the $K^*_L \bar{K}$ and $\bar{K}^*_L K$ bands will interfere constructively and all values of L are in principle allowed. In particular, the

$a_0(980)$ resonance is described by a coupled-channel Breit-Wigner function as measured in Ref. [41]. In the following, all resonances listed in Ref. [3] and satisfying the above criteria are included or tested in the Dalitz-plot analysis. The two-body invariant-mass resolution varies with invariant-mass and is approximately 7 MeV in the $K\pi$ mass region between 1 and 2 GeV, much smaller than the width of the resonances present in this analysis. Therefore, resolution effects are ignored. The efficiency-corrected fractional contribution f_i, due to resonant or nonresonant contribution i, is defined as follows:

$$f_i = \frac{|c_i|^2 \int |A_i(x,y)|^2 \mathrm{d}x\mathrm{d}y}{\int |\sum_j c_j A_j(x,y)|^2 \mathrm{d}x\mathrm{d}y}, \tag{18}$$

where x and y indicate the Dalitz-plot variables and the integrals in the numerator and denominator are computed on a large sample of simulated events generated uniformly in the decay phase space. The f_i do not necessarily sum to 100% because of interference effects. The uncertainty for each f_i is evaluated by propagating the full covariance matrix obtained from the fit. Interference fractions between amplitudes i and j are evaluated as

$$f_{ij} = \frac{\int c_i c_j^* A_i(x,y) A_j^*(x,y) \mathrm{d}x\mathrm{d}y}{\int |\sum_j c_j A_j(x,y)|^2 \mathrm{d}x\mathrm{d}y}. \tag{19}$$

After the fit, a large simulated sample is prepared, where events are generated uniformly in the decay phase space [37]. These events are weighted by the fitted likelihood function, normalized to the data-event yields and compared to the data on several invariant-mass and angular projections. To assess the fit quality, the Dalitz plot is divided into a grid of $n \times n$ cells (n depends on the event yields and Dalitz-plot size) and only those cells containing at least two simulated events are considered. A χ^2 estimator is used, defined as $\chi^2 = \sum_{i=1}^{N_{\text{cells}}} (N^i_{\text{obs}} - N^i_{\text{exp}})^2/\varepsilon^2$, where N^i_{obs} and N^i_{exp} are event yields from data and simulation, respectively. Here $\varepsilon = \sqrt{N^i_{\text{exp}}}$ for cells containing more than 9 entries, while it is approximated as the average of the lower and upper Poisson 68% C.L. errors for lower statistics cells. The figure of merit is defined as χ^2/ndf where ndf is computed as $N_{\text{cells}} - n_{\text{par}}$ and n_{par} is the number of free parameters.

Two amplitude fits are then performed. The first employs a QMI description of the $K\pi$ S-wave (Sec. VII D) and the second uses an isobar model (Sec. VII E).

2. Fits to the η_c sidebands

The background model is obtained by fitting the η_c sidebands. An unbinned maximum-likelihood fit is performed by inserting, one by one, all possible a_0 and a_2 resonances decaying to a $K^0_S K$ state and all possible K^* resonances decaying to a $K\pi$ state [3] which could contribute to the $K^0_S K\pi$ final state. To describe the fraction of background candidates associated to the B^+ decay (see Table V), resonances are described by relativistic Breit-Wigner functions with appropriate Blatt-Weisskopf [40] form factors using angular terms just as for the η_c decay but, for K^* resonances, there is no symmetrization requirement for charged and neutral contributions. Interference is also allowed between all the contributing amplitudes. The fraction of background not associated to the B^+ decay is assumed to be uniform, except for a small contribution from $K^*(892)$ resonances, described only by relativistic Breit-Wigner functions. Small open-charm contributions are described by simple Gaussian functions with parameters fitted to the data. No efficiency is included in the description of the sidebands. The amplitudes are numerically integrated using a phase-space simulation generated according to the $K^0_S K\pi$ invariant-mass distributions in the sidebands shown in Fig. 12. Contributions which are uniform in the phase space of the decay, having fixed fractions f_B (given in Table V), are included. Due to the limited sample size in the sideband regions, the K^0_{SLL} and K^0_{SDD} data are combined.

D. Fit using a QMI description of the $K\pi$ S-wave

To measure the $I = 1/2$ $K\pi$ S-wave, the QMI technique described in Refs. [11,42] is used. In this fit, the $K\pi$ S-wave, being the largest contribution, is taken as the reference amplitude. The $K\pi$ invariant-mass spectrum is divided into 37 equally spaced mass intervals each 50 MeV wide, and two new fit parameters are added for each interval: the amplitude and the phase of the $K\pi$ S-wave. The amplitude is fixed to 1.0 and its phase to $\pi/2$ at an arbitrary point in the mass spectrum, chosen to be interval 16, corresponding to a mass of 1.45 GeV. The number of free parameters associated to the description of the QMI $K\pi$ S-wave is therefore 72. The $K\pi$ S-wave amplitude in bin j is written as

$$A^j_{S\text{-wave}} = \frac{1}{\sqrt{2}}(a_j^{K\pi} e^{i\phi_j^{K\pi}} + a_j^{K^0\pi} e^{i\phi_j^{K^0\pi}}), \tag{20}$$

where the amplitude $a_j^{K\pi}(m) = a_j^{K^0\pi}(m)$ and the phase $\phi_j^{K\pi}(m) = \phi_j^{K^0\pi}(m)$ at the $K\pi$ mass m. All the $K^*_L(1430)\bar{K}$ contributions with $L = 0, 2$ are symmetrized in the same way as for the S-wave amplitude.

The fit is initiated by performing a randomized scan for the $K\pi$ S-wave solution with arbitrary start values of parameters. In addition, expected contributions from known resonances such as $a_0(980)$, $a_2(1320)$, $K^*_2(1430)$, $a_0(1450)$, $a_2(1750)$, and $K^*_2(1900)$ are included. The $a_0(1700)$ resonance, recently observed in the Dalitz-plot analysis of $\eta_c \to \eta\pi^+\pi^-$ [14] is also included and found to be significant. The presence of an $a_0(1950)$ resonance, for which some evidence was found in the η_c Dalitz-plot analysis Ref. [11], is tested, but its contribution is found to be consistent with zero. In the search for the best solution, the fit is iterated from the first found solution and

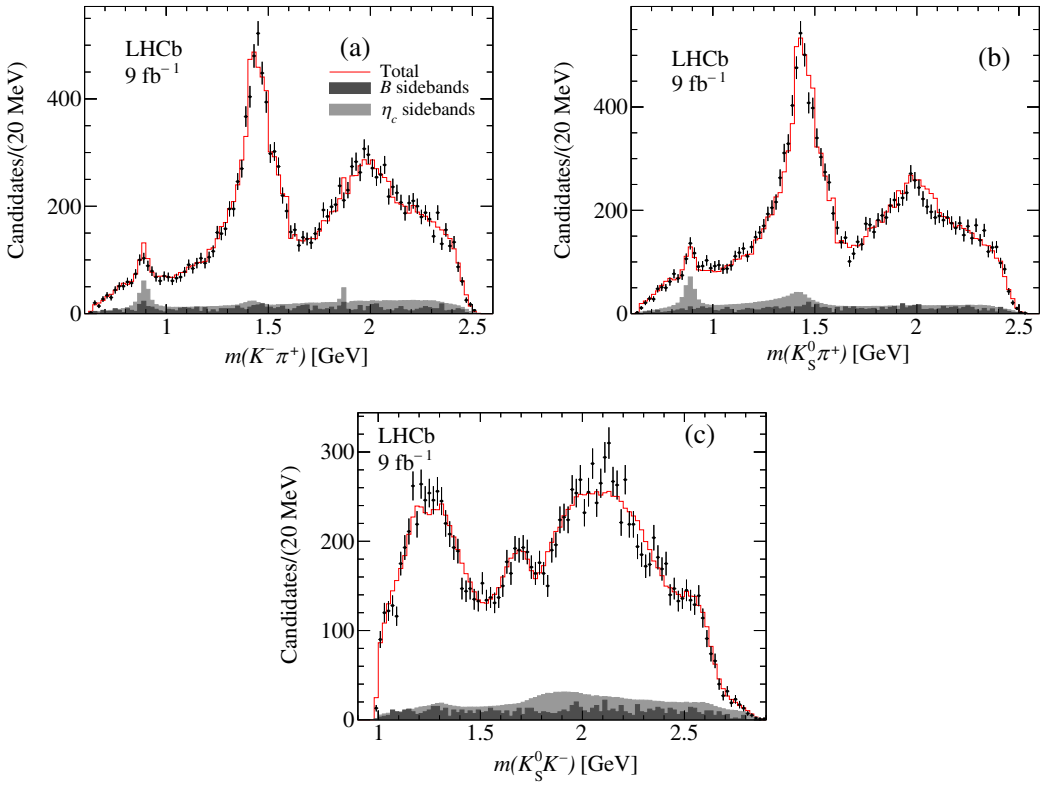

FIG. 14. Fit projections on the $K^-\pi^+$, $K^0_S\pi^+$ and $K^0_S K^-$ invariant-mass distributions from the Dalitz-plot analysis of the η_c decay using the QMI model for $B^+ \to K^0_S K^+ K^-\pi^+$ data.

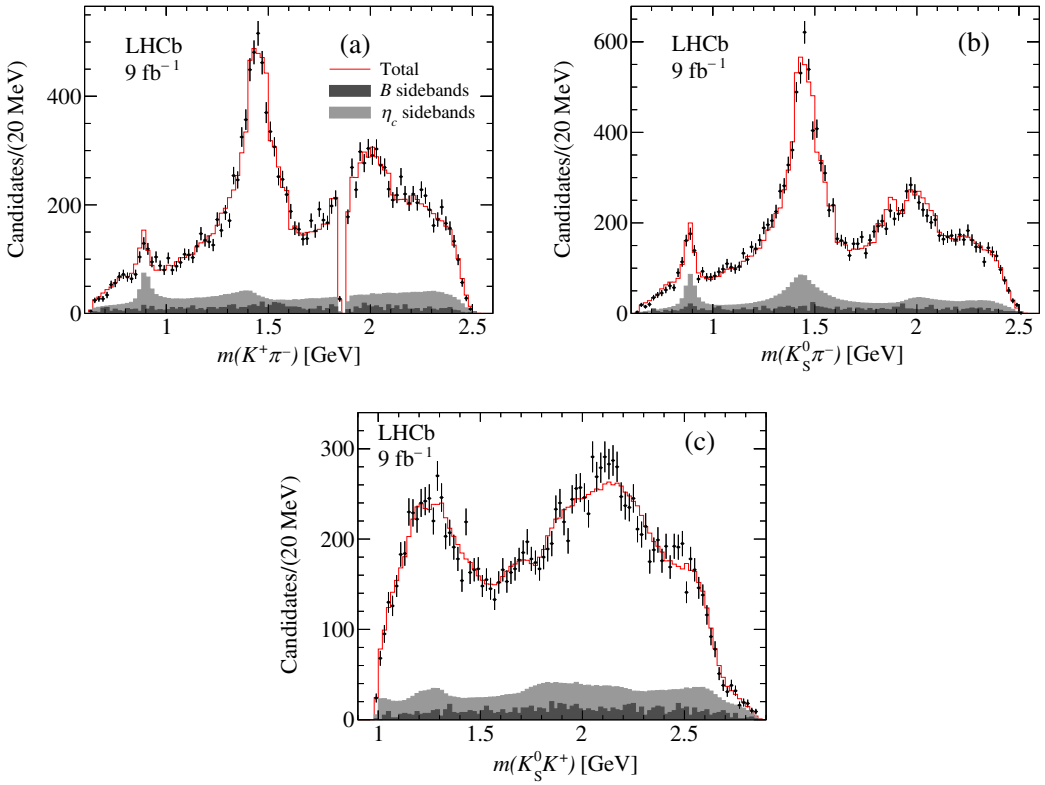

FIG. 15. Fit projections on the $K^+\pi^-$, $K^0_S\pi^-$ and $K^0_S K^+$ invariant-mass distributions from the Dalitz-plot analysis of η_c decay using the QMI model for the $B^+ \to K^0_S K^+ K^+\pi^-$ data.

TABLE VI. Results from the Dalitz-plot analysis of the η_c decay in (top) $B^+ \to K^0_S K^+ K^- \pi^+$, (center) $B^+ \to K^0_S K^+ K^+ \pi^-$ and (bottom) inverse-variance-weighted averages. The QMI model is used for the $K\pi$ S-wave.

Final state	Fraction [%]	Phase [rad]
	$B^+ \to K^0_S K^+ K^- \pi^+$	
$(K\pi)_S K$	$120.6 \pm 2.4 \pm 5.4$	0.
$a_0(1450)\pi$	$2.4 \pm 0.4 \pm 0.8$	$2.48 \pm 0.07 \pm 0.09$
$K^*_2(1430)K$	$16.6 \pm 0.8 \pm 0.9$	$4.31 \pm 0.03 \pm 0.11$
$a_2(1320)\pi$	$0.7 \pm 0.2 \pm 0.5$	$4.18 \pm 0.10 \pm 0.27$
$a_0(980)\pi$	$11.3 \pm 0.6 \pm 0.9$	$-2.93 \pm 0.03 \pm 0.03$
$a_0(1700)\pi$	$1.5 \pm 0.2 \pm 0.2$	$2.00 \pm 0.08 \pm 0.14$
$K^*_2(1980)K$	$2.8 \pm 0.3 \pm 1.0$	$-0.08 \pm 0.07 \pm 0.14$
$a_2(1750)\pi$	$0.2 \pm 0.1 \pm 0.1$	$-3.56 \pm 0.20 \pm 0.24$
Sum	$156.1 \pm 2.7 \pm 11.4$	
$\chi^2/\text{ndf} = 1706/(1597-17) = 1.08$		
	$B^+ \to K^0_S K^+ K^+ \pi^-$	
$(K\pi)_S K$	$106.0 \pm 2.8 \pm 8.5$	0.
$a_0(1450)\pi$	$0.8 \pm 0.3 \pm 0.4$	$1.64 \pm 0.14 \pm 0.47$
$K^*_2(1430)K$	$17.8 \pm 0.9 \pm 1.0$	$4.32 \pm 0.03 \pm 0.13$
$a_2(1320)\pi$	$0.7 \pm 0.2 \pm 0.5$	$4.22 \pm 0.11 \pm 0.93$
$a_0(980)\pi$	$9.7 \pm 0.6 \pm 0.3$	$-3.02 \pm 0.04 \pm 0.05$
$a_0(1700)\pi$	$0.8 \pm 0.2 \pm 0.2$	$2.10 \pm 0.11 \pm 0.24$
$K^*_2(1980)K$	$6.3 \pm 0.6 \pm 1.9$	$0.13 \pm 0.05 \pm 0.08$
$a_2(1750)\pi$	$0.2 \pm 0.2 \pm 0.3$	$-3.87 \pm 0.22 \pm 0.16$
Sum	$143.7 \pm 2.9 \pm 8.8$	
$\chi^2/\text{ndf} = 1686/(1589-17) = 1.07$		
	$B \to K^0_S K K \pi$	
$(K\pi)_S K$	$114.4 \pm 1.8 \pm 4.6$	0.
$a_0(1450)\pi$	$1.4 \pm 0.2 \pm 0.4$	$2.31 \pm 0.06 \pm 0.09$
$K^*_2(1430)K$	$17.1 \pm 0.6 \pm 0.7$	$4.32 \pm 0.02 \pm 0.08$
$a_2(1320)\pi$	$0.7 \pm 0.1 \pm 0.4$	$4.20 \pm 0.08 \pm 0.26$
$a_0(980)\pi$	$10.5 \pm 0.4 \pm 0.4$	$-2.97 \pm 0.02 \pm 0.03$
$a_0(1700)\pi$	$1.0 \pm 0.1 \pm 0.1$	$2.04 \pm 0.06 \pm 0.12$
$K^*_2(1980)K$	$3.5 \pm 0.3 \pm 0.9$	$0.06 \pm 0.04 \pm 0.07$
$a_2(1750)\pi$	$0.2 \pm 0.1 \pm 0.1$	$-3.69 \pm 0.15 \pm 0.16$
Sum	$148.8 \pm 2.0 \pm 4.8$	

TABLE VII. Fractional interference contributions from the Dalitz-plot analysis of the η_c decay in $B^+ \to K^0_S K^+ K^- \pi^+$ decays using the QMI model. Absolute values less than 3% are not listed.

Amplitude 1	Amplitude 2	Fraction [%]
$(K\pi)_S K$	$a_0(1450)\pi$	-14.1 ± 1.1
$(K\pi)_S K$	$K^*_2(1430)K$	-27.8 ± 1.0
$(K\pi)_S K$	$a_0(980)\pi$	-9.2 ± 1.3
$a_0(980)\pi$	$a_0(1450)\pi$	-3.7 ± 0.3

TABLE VIII. Systematic uncertainties on (left) fractional contributions (%) and (right) phases (rad) in the η_c Dalitz-plot analysis in the $B^+ \to K^0_S K^+ K^- \pi^+$ decay using the QMI model for the $K\pi$ S-wave.

Final state	Efficiency	Trigger	Purity	r	Back	Total	Efficiency	Trigger	Purity	r	Back	Tot
$(K\pi)_S K$	3.27	0.89	1.03	4.01	0.48	5.37						
$a_0(1450)\pi$	0.65	0.29	0.24	0.16	0.06	0.77	0.04	0.07	0.03	0.00	0.03	0.09
$K^*_2(1430)K$	0.02	0.17	0.04	0.86	0.48	1.00	0.08	0.06	0.03	0.05	0.01	0.11
$a_2(1320)\pi$	0.38	0.10	0.34	0.04	0.08	0.53	0.21	0.08	0.14	0.05	0.01	0.27
$a_0(980)\pi$	0.70	0.05	0.47	0.12	0.34	0.92	0.01	0.02	0.02	0.00	0.02	0.04
$a_0(1700)\pi$	0.12	0.05	0.05	0.08	0.01	0.16	0.10	0.08	0.02	0.00	0.00	0.14
$K^*_2(1980)K$	0.04	0.08	0.19	0.96	0.16	1.00	0.10	0.06	0.04	0.08	0.01	0.14
$a_2(1750)\pi$	0.05	0.01	0.05	0.03	0.03	0.09	0.04	0.14	0.05	0.11	0.06	0.20

additional resonances are added one by one; the process is completed when additional contributions give fit fractions consistent with zero. Spin-1 K^* resonances [$K^*(892)$, $K^*(1410)$ and $K^*(1680)$] are also tested but their contributions are found to be consistent with zero. The inclusion of additional spin-0 and spin-2 resonance components with unconstrained resonance parameters leads to no improvement of the fit quality.

Figures 14 and 15 show the Dalitz-plot projections with superimposed projections of the fit function for $B^+ \to K^0_S K^+ K^- \pi^+$ and $B^+ \to K^0_S K^+ K^+ \pi^-$ data, respectively. The distributions of the fitted background, interpolated from the η_c and B^+ sidebands, are also included. The fractional contributions and relative phases from the fit are given in Table VI. There is a significant contribution from interference terms, evidenced by a sum of fractions much larger than 100%. This is a common feature of Dalitz-plot analyses dealing with several broad resonances having the same quantum numbers [43]. Interferences between amplitudes are listed in Table VII for absolute values above 3%.

To test the fit quality, the efficiency-uncorrected Legendre-polynomial moments P_L are computed in each $K^-\pi^+$, $K^0_S\pi^+$ and $K^0_S K^-$ mass interval by weighting each event by a $P_L(\cos\theta)$ function, where θ is the corresponding helicity angle [44]. These distributions are shown in Figs. 26–28 of the Appendix as functions of the $K^-\pi^+$, $K^0_S\pi^+$ and $K^0_S K^-$ invariant masses, respectively. The extracted moment distributions are compared with the expected Legendre polynomial moment distributions obtained from simulated data weighted by the fit results. Good agreement for all the distributions is observed, which indicates that the fit is able to reproduce the local structures apparent in the Dalitz plot.

Systematic uncertainties, evaluated separately for the $B^+ \to K^0_S K^+ K^- \pi^+$ and $B^+ \to K^0_S K^+ K^+ \pi^-$ final states, are summarized in Tables VIII and IX, respectively. The effect of the efficiency correction, labeled as "Efficiency" in Table VIII, is evaluated by replacing the two-dimensional fitted efficiency $\epsilon(m_x(K^0_S K), \cos\theta_\pi))$ with the product of the fits to the efficiency projections $\epsilon = \epsilon_1(m_x(K^0_S K)) \cdot \epsilon_2(\cos\theta_\pi)$. The uncertainty related to trigger effects (Trigger) is estimated by performing separate Dalitz-plot analyses of the TOS and no TOS data samples using appropriate efficiency evaluations. The inverse-variance-weighted averages are compared with the values from the reference fit, and the absolute values of the deviations are taken as systematic uncertainties. The uncertainty on the signal purity (Purity) is evaluated by performing Dalitz-plot analyses on datasets selected varying the BDT classifier requirement, which changes the purity by ±5%. Their inverse-variance-weighted averages are compared with the values from the reference fit, and the absolute deviations are taken as systematic uncertainties. The radius r of the Blatt-Weisskopf factor, by default fixed to 1.5 GeV^{-1}, is varied

TABLE IX. Systematic uncertainties on (left) fractional contributions (%) and (right) phases (rad) in the η_c Dalitz-plot analysis in the $B^+ \to K^0_S K^+ K^+ \pi^-$ decay using the QMI model for the $K\pi$ S-wave.

Final state	Efficiency	Trigger	Purity	r	Back	Total	Efficiency	Trigger	Purity	r	Back	Tot
$(K\pi)_S K$	6.06	2.94	2.80	4.39	0.20	8.52						
$a_0(1450)\pi$	0.30	0.12	0.24	0.14	0.06	0.43	0.31	0.35	0.08	0.01	0.01	0.47
$K^*_2(1430)K$	0.32	0.08	0.30	0.88	0.54	1.13	0.09	0.07	0.04	0.06	0.01	0.13
$a_2(1320)\pi$	0.32	0.09	0.30	0.08	0.11	0.47	0.27	0.13	0.19	0.05	0.86	0.93
$a_0(980)\pi$	0.01	0.17	0.02	0.22	0.26	0.46	0.02	0.02	0.03	0.02	0.02	0.06
$a_0(1700)\pi$	0.12	0.00	0.08	0.08	0.01	0.17	0.18	0.15	0.03	0.00	0.01	0.24
$K^*_2(1980)K$	0.46	0.11	0.43	1.77	0.22	1.89	0.04	0.01	0.06	0.05	0.01	0.08
$a_2(1750)\pi$	0.21	0.10	0.13	0.02	0.03	0.27	0.09	0.02	0.06	0.11	0.19	0.25

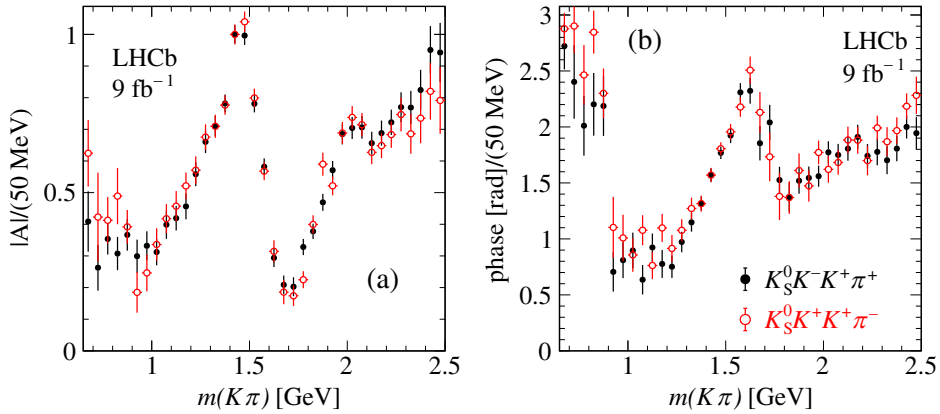

FIG. 16. Comparisons between the fitted $K\pi$ S-wave (a) amplitude and (b) phase obtained from the (black) $B^+ \to K^0_S K^+K^-\pi^+$ and (red) $B^+ \to K^0_S K^+K^+\pi^-$ data. Note that the point at 1.425 GeV is fixed at values 1.0 and 1.57 for amplitude and phase, respectively, and therefore there is no associated uncertainty. The plotted uncertainties are obtained averaging the uncertainties on the two adjacent mass measurements.

between 0.5 and 2.5 GeV^{-1}. The uncertainty due to the background model (Back) is evaluated by performing 100 fits to the same dataset, where in each fit all the parameters describing the background model are randomly varied within their statistical uncertainties according to a Gaussian distribution. The absolute values of the averages of the differences with respect to the reference values are taken as systematic uncertainties on amplitudes and phases. Possible fit biases are evaluated by generating, from the solution found by the fit, 100 pseudoexperiments having the same size as the data. The average of the differences between the reference solution and that from the pseudoexperiments gives an evaluation of the fit bias. It is found that this contribution is not significant and it is not included in the list of the systematic uncertainties. The effect of varying the position of the sidebands, from which the background model is derived, is investigated and found to have negligible impact on the total systematic uncertainty, and is therefore ignored. All the contributions are added in quadrature (Total).

Figure 16 shows the fitted $K\pi$ S-wave amplitude and phase obtained from the QMI analysis for both the $B^+ \to K^0_S K^+K^-\pi^+$ and $B^+ \to K^0_S K^+K^+\pi^-$ data, which agree well. The data show a dominance of the $K^*_0(1430)$ resonant contribution followed by a sharp drop and a subsequent signal of the $K^*_0(1950)$ resonance. A contribution in the phase motion not continuous with the rest of the distribution is present in the threshold region of Fig. 16(b). This behavior may be attributed to the inability of the algorithm to obtain a correct phase motion in this region of the phase space due to the absence, in this mass region, of additional significant resonant contributions in addition to that of the $K^*_0(1430)$ resonance.

The inverse-variance-weighted average of the $K\pi$ S-wave from the $B^+ \to K^0_S K^+K^-\pi^+$ and $B^+ \to K^0_S K^+K^+\pi^-$ data is shown in terms of the real and imaginary parts of its amplitude in the Argand diagram of Fig. 17. The plot shows the expected anticlockwise phase motion due to the $K^*_0(1430)$ resonance and a second loop due to the presence of the $K^*_0(1950)$ resonance, observed here for the first time. Note that it was not possible to observe this behavior in Ref. [6] due to the presence of two solutions above the mass of 1.6 GeV.

Systematic uncertainties on the QMI $K\pi$ S-wave amplitudes are evaluated as follows. The $B^+ \to K^0_S K^+K^-\pi^+$ and $B^+ \to K^0_S K^+K^+\pi^-$ datasets are each fitted independently using QMI for lower and higher purity selections, averaging the results; this is also done separately for TOS and no TOS selections. The four solutions are compared with the reference solution and the absolute values of the deviations are added in quadrature. The effect on the QMI $K\pi$ S-wave due to the variation of the resonance parameters fixed to

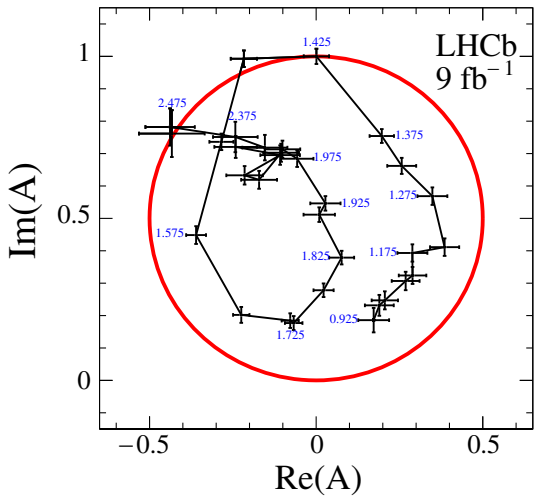

FIG. 17. Argand diagram for the $K\pi$ S-wave averaged over the QMI results from $B^+ \to K^0_S K^+K^-\pi^+$ and $B^+ \to K^0_S K^+K^+\pi^-$ data.

known values, in particular those for the $a_0(980)$ and $K^*_2(1430)$ resonances, is tested and found to be negligible. The numerical values of the resulting QMI $K\pi$ S-wave amplitudes and phases are listed in the Appendix, and this topic is further discussed in Sec. VII E.

E. Isobar model η_c Dalitz plot analysis

The QMI method used in the previous section has allowed information to be obtained about the $K\pi$ S-wave which is produced by a combination of several scalar resonances. However, the procedure does not give insight into the parameters of the contributing resonances. An additional description of the data is therefore performed, known as the isobar model, which fits the data with a superposition of known resonances and additional (unknown or poorly known) states. Both methods are expected to give similar descriptions of the data.

The fitting method is the same as that described in Sec. VII D, but in this case all the resonances are described by relativistic Breit-Wigner functions with parameters initially fixed to their default values [3]. The search for the best solution is performed by adding resonances one by one, using the $K^*_0(1430)$ resonance as the reference amplitude, and considering as figures of merit, the likelihood and χ^2/ndf behavior, as discussed in Sec. VII D. It is found that, using only the list of the known resonances [3], a poor description of the data is obtained. A large improvement [increased likelihood $\Delta(2\log\mathcal{L}) = 1338$ and decreased χ^2/ndf] is obtained by adding an additional scalar $K\pi$ resonance with free parameters, labeled in the following as $\kappa(2600)$ and included in the fit using the simple nonrelativistic BW function of Eq. (5). Resonances having poorly known parameters, namely the $K^*_0(1430)$, $K^*_0(1950)$ and $a_0(1700)$ resonances, are allowed to have free parameters. The significance of the $K^*_2(1980)$ is found to be consistent with zero and its contribution is removed from the fit. The procedure is developed on the $B^+ \to K^0_S K^+ K^- \pi^+$ data, because of the better quality of this final state due to reduced combinatorial background, and is then tested on the $B^+ \to K^0_S K^+ K^+ \pi^-$ final state. The fit projections are shown in Fig. 18 for the $B^+ \to K^0_S K^+ K^- \pi^+$ data; they are similar for the $B^+ \to K^0_S K^+ K^+ \pi^-$ data and are shown in Fig. 29 of the Appendix.

The resulting fitted parameters are listed in Table X together with the estimated significances, evaluated using Wilks's theorem [45]. A test is made for the presence of the low-mass $\kappa/K^*_0(700)$ resonance, with parameters fixed to average values [3]. The resulting likelihood variation is $\Delta(2\log\mathcal{L}) = 6.6$ for the difference of two parameters which corresponds to a significance of 1.8σ. The same is true for the $B^+ \to K^0_S K^+ K^+ \pi^-$ decay where $\Delta(2\log\mathcal{L}) = 12.6$, corresponding to a significance of 2.9σ. Replacing the broad $\kappa(2600)$ resonance with a uniform nonresonant contribution results in a decrease of the likelihood function by $\Delta(2\log\mathcal{L}) = 254$.

The fitted resonance contributions and relative phases are given in Table XI. Interferences between amplitudes are listed in Table XII and shown in Fig. 18 for absolute values above 3%.

Systematic uncertainties on fractions and relative phases are evaluated as in Sec. VII D with the addition of an alternative model for the $K^*_0(1430)$ resonance: a simplified coupled-channel Breit-Wigner function, which ignores the small $K\eta$ coupling. Its line shape is parametrized as

$$\mathrm{BW}(m) = \frac{1}{m_0^2 - m^2 - i(\rho_1(m) g^2_{K\pi} + \rho_2(m) g^2_{K\eta'})}, \tag{21}$$

where m_0 is the resonance mass, $g_{K\pi}$ and $g_{K\eta'}$ are the couplings to the $K\pi$ and $K\eta'$ final states and $\rho_j(m) = 2p/m$ are the respective Lorentz-invariant phase-space factors, with p the decay-particle momentum in the $K^*_0(1430)$ rest frame. The $\rho_2(m)$ function becomes imaginary below the $K\eta'$ threshold. The Dalitz-plot analysis is insensitive to the $g_{K\eta'}$ parameter, which has been fixed to $g^2_{K\eta'} = 0.197\ \mathrm{GeV}^2/c^4$ [14]. A similar method is used for the evaluation of the systematic uncertainties on the resonance parameters.

The isobar model allows the separation of the resonance composition of the $K\pi$ S-wave obtained from the QMI method. A fit to the $K\pi$ S-wave amplitude and phase is performed using the sum of three interfering spin-0 relativistic Breit-Wigner amplitudes:

$$\begin{aligned} f(m) = {} & c_1 \mathrm{BW}_{K^*(1430)}(m) e^{i\phi_1} + c_2 \mathrm{BW}_{K^*(1950)}(m) e^{i\phi_2} \\ & + c_3 \mathrm{BW}_{\kappa(2600)}(m) e^{i\phi_3}, \end{aligned} \tag{22}$$

where m indicates the $K\pi$ mass. In this fit, the mass and width of the three resonances are fixed to the results obtained in the isobar model analysis while their coefficients and relative phases are left as free parameters. The fitted $K\pi$ S-wave used in the fit is obtained from the inverse-variance-weighted averages from the $B^+ \to K^0_S K^+ K^- \pi^+$ and $B^+ \to K^0_S K^+ K^+ \pi^-$ data. The QMI amplitude and phase, together with the squared amplitude, are shown in Fig. 19, where the statistical and systematic uncertainties are added in quadrature and the phase measurements in the $K\pi$ mass region below 0.90 GeV are not included in the fit. The amplitude and phase of the data point at a mass of 1.425 GeV are fixed in the QMI analysis and the reported uncertainties are obtained from the averages of the two adjacent mass values. The fit has a p value of 63% and is shown in Fig. 19, together with the

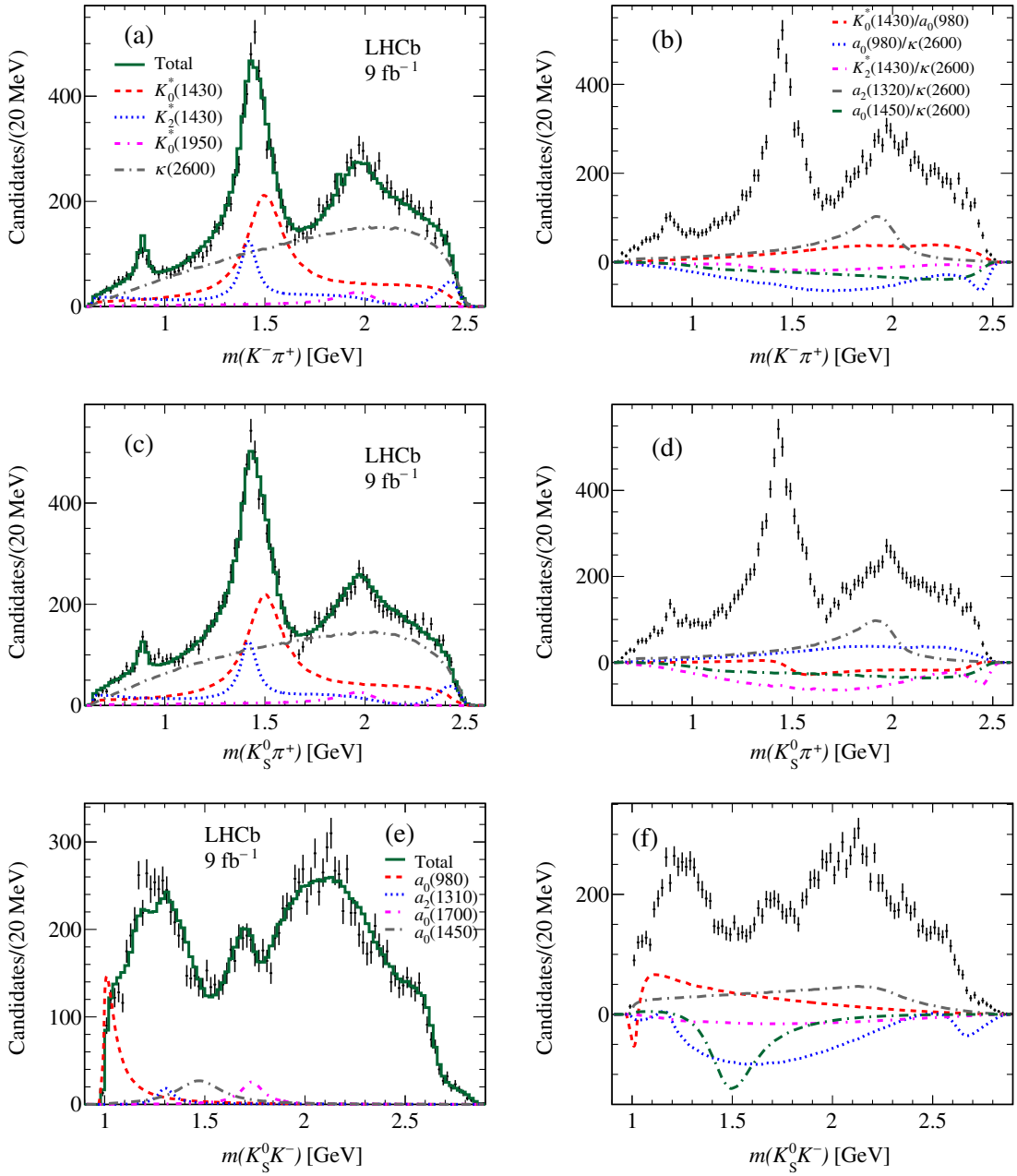

FIG. 18. Fit projections on the $K^-\pi^+$, $K^0_S\pi^+$ and $K^0_SK^-$ invariant-mass distributions from the Dalitz-plot analysis of the η_c decay using the isobar model for the $B^+ \to K^0_SK^+K^-\pi^+$ data. Panels (a), (c), (e) show the most important resonant contributions. To simplify the plots, only resonant contributions relative to that mass projection are shown. Panels (b), (d), (f) show the interference terms for contributions greater than 3%. The legend in (a) also applies to (c) and the legend in (b) also applies to (d) and (f).

TABLE X. Fitted parameters and significances of the resonances observed in the η_c Dalitz-plot analysis. Significances larger than 10σ are evaluated as $\sqrt{\Delta(2\log\mathcal{L})}$.

Resonance	Mass [MeV]	Γ [MeV]	$\Delta(2\log\mathcal{L})$	Significance
$K_0^*(1430)$	$1493 \pm 4 \pm 7$	$215 \pm 7 \pm 4$	...	...
$K_0^*(1950)$	$1980 \pm 14 \pm 19$	$229 \pm 26 \pm 16$	316	17.8σ
$a_0(1700)$	$1736 \pm 10 \pm 12$	$134 \pm 17 \pm 61$	161	12.7σ
$\kappa(2600)$	$2662 \pm 59 \pm 201$	$480 \pm 47 \pm 72$	1338	36.6σ

TABLE XI. Results from the Dalitz-plot analysis of the η_c using the isobar model for (top) $B^+ \to K^0_S K^+ K^- \pi^+$ decays, $B^+ \to K^0_S K^+ K^+ \pi^-$ decays (center) and their inverse-variance-weighted averages (bottom).

Final state	Fraction [%]	Phase [rad]
	$B^+ \to K^0_S K^+ K^- \pi^+$	
$K^*_0(1430)K$	$35.1 \pm 1.3 \pm 2.9$	0.
$a_0(980)\pi$	$5.6 \pm 0.8 \pm 1.6$	$-3.39 \pm 0.08 \pm 0.13$
$K^*_2(1430)K$	$15.4 \pm 1.0 \pm 1.1$	$3.53 \pm 0.03 \pm 0.10$
$a_2(1320)\pi$	$1.1 \pm 0.2 \pm 0.3$	$-2.90 \pm 0.11 \pm 0.26$
$K^*_0(1950)K$	$3.9 \pm 0.4 \pm 0.3$	$-0.46 \pm 0.06 \pm 0.63$
$a_0(1700)\pi$	$1.7 \pm 0.3 \pm 0.4$	$1.00 \pm 0.08 \pm 0.17$
$a_0(1450)\pi$	$3.4 \pm 0.5 \pm 0.8$	$-4.78 \pm 0.08 \pm 0.17$
$a_2(1750)\pi$	$0.3 \pm 0.1 \pm 0.1$	$2.43 \pm 0.17 \pm 0.17$
$\kappa(2600)K$	$63.9 \pm 3.4 \pm 8.1$	$-0.42 \pm 0.05 \pm 0.14$
Sum	$130.5 \pm 4.0 \pm 8.9$	
$\chi^2/\text{ndf} = 1798/(1589-19) = 1.15$		
	$B^+ \to K^0_S K^+ K^+ \pi^-$	
$K^*_0(1430)K$	$32.0 \pm 1.2 \pm 2.8$	0.
$a_0(980)\pi$	$4.9 \pm 0.6 \pm 1.0$	$-3.37 \pm 0.08 \pm 0.11$
$K^*_2(1430)K$	$13.8 \pm 1.0 \pm 1.2$	$3.56 \pm 0.03 \pm 0.11$
$a_2(1320)\pi$	$1.2 \pm 0.2 \pm 0.3$	$-2.82 \pm 0.11 \pm 0.24$
$K^*_0(1950)K$	$3.4 \pm 0.4 \pm 0.3$	$-0.42 \pm 0.06 \pm 0.64$
$a_0(1700)\pi$	$0.7 \pm 0.2 \pm 0.2$	$1.18 \pm 0.11 \pm 0.28$
$a_0(1450)\pi$	$2.0 \pm 0.4 \pm 0.7$	$-4.86 \pm 0.10 \pm 0.22$
$a_2(1750)\pi$	$0.3 \pm 0.1 \pm 0.1$	$2.24 \pm 0.18 \pm 0.17$
$\kappa(2600)K$	$59.8 \pm 3.4 \pm 7.3$	$-0.32 \pm 0.05 \pm 0.12$
Sum	$118.1 \pm 2.7 \pm 8.0$	
$\chi^2/\text{ndf} = 1738/(1584-21) = 1.11$		
	$B \to K^0_S K K \pi$	
$K^*_0(1430)K$	$33.4 \pm 0.9 \pm 2.0$	0.
$a_0(980)\pi$	$5.1 \pm 0.5 \pm 0.8$	$-3.38 \pm 0.06 \pm 0.08$
$K^*_2(1430)K$	$14.6 \pm 0.7 \pm 0.8$	$3.54 \pm 0.02 \pm 0.07$
$a_2(1320)\pi$	$1.1 \pm 0.1 \pm 0.2$	$-2.89 \pm 0.08 \pm 0.18$
$K^*_0(1950)K$	$3.7 \pm 0.3 \pm 0.2$	$-0.44 \pm 0.04 \pm 0.45$
$a_0(1700)\pi$	$1.1 \pm 0.2 \pm 0.2$	$1.05 \pm 0.06 \pm 0.15$
$a_0(1450)\pi$	$2.6 \pm 0.3 \pm 0.5$	$-4.82 \pm 0.06 \pm 0.13$
$a_2(1750)\pi$	$0.3 \pm 0.1 \pm 0.1$	$2.33 \pm 0.12 \pm 0.11$
$\kappa(2600)K$	$61.8 \pm 2.4 \pm 5.4$	$-0.37 \pm 0.03 \pm 0.09$
Sum	$123.7 \pm 2.7 \pm 4.7$	

TABLE XII. Fractional interference contributions from the Dalitz-plot analysis of the η_c decay in $B^+ \to K^0_S K^+ K^- \pi^+$ decays using the isobar model. Absolute values less than 3% are not listed.

Amplitude 1	Amplitude 2	Fraction [%]
$K^*_0(1430)K$	$a_0(980)\pi$	-6.1 ± 0.5
$a_0(980)\pi$	$a_0(1450)\pi$	-3.6 ± 0.4
$a_0(980)\pi$	$\kappa(2600)K$	14.4 ± 1.9
$K^*_2(1430)K$	$K^*_0(1950)K$	-3.7 ± 0.3
$K^*_2(1430)K$	$\kappa(2600)K$	-26.2 ± 1.1
$a_2(1320)\pi$	$\kappa(2600)K$	-6.5 ± 0.7
$K^*_0(1950)K$	$\kappa(2600)K$	18.6 ± 1.5
$a_0(1700)\pi$	$\kappa(2600)K$	-4.6 ± 0.7
$a_0(1450)\pi$	$\kappa(2600)K$	-14.5 ± 1.0

composition of the fitted resonances. The relative phases are $\phi_1 = 0.66 \pm 0.03$ rad, $\phi_2 = -0.08 \pm 0.09$ rad and $\phi_3 = 0.61 \pm 0.05$ rad. These values can be used to compare relative phases with respect to the $K^*_0(1430)$ resonance, yielding $\phi_2 - \phi_1 = -0.74 \pm 0.09$ rad and $\phi_3 - \phi_1 = -0.05 \pm 0.06$ rad. These differences are within 0.65σ and 2.8σ, respectively, with respect to the values obtained from the isobar model listed in Table XI. This test shows that the $K\pi$ S-wave obtained using the QMI method can be interpreted as due to the sum of the three interfering K^*_0 resonances observed with the isobar model. This result is similar to what was observed in the $\pi\pi$ final state in Ref. [46], where the $f_0(980)$ resonance was found to interfere with the broad $\sigma/f_0(500)$ resonance.

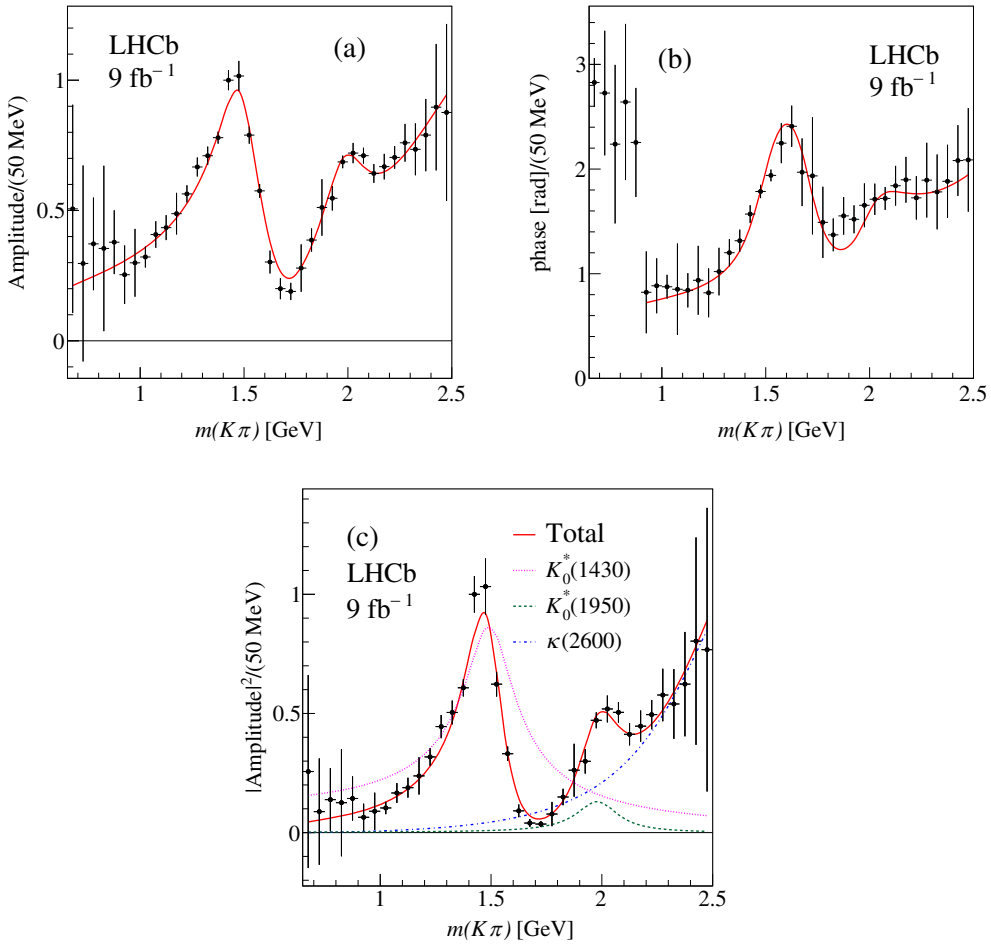

FIG. 19. Fit to the (a) amplitude, (b) phase, and (c) squared amplitude from the η_c QMI analysis using the results from the isobar-model analysis. The black points are obtained using the inverse-variance-weighted averages of the $B^+ \to K^0_S K^+ K^- \pi^+$ and $B^+ \to K^0_S K^+ K^+ \pi^-$ data. The error bars are computed as the quadratic sum of the statistical and systematic uncertainties. The phase measurements in the $K\pi$ mass region below 0.90 GeV are not included in the fit.

VIII. DALITZ-PLOT ANALYSIS OF $\eta_c(2S)$ DECAY TO $K^0_S K\pi$

In this section a Dalitz-plot analysis of the $\eta_c(2S)$ decay to the final state

$$B^+ \to \eta_c(2S) K^+,$$
$$\eta_c(2S) \to K^0_S K^- \pi^+, \tag{23}$$

is described. Figure 5 shows the $K^0_S K\pi$ mass spectra for the $B^+ \to K^0_S K^+ K^- \pi^+$ and $B^+ \to K^0_S K^+ K^+ \pi^-$ data. The $\eta_c(2S)$ signal is accompanied by a significant background contribution which is especially large in the $B^+ \to K^0_S K^+ K^+ \pi^-$ data by virtue of the two indistinguishable particles in the final state. Therefore, only the $B^+ \to K^0_S K^+ K^- \pi^+$ data are used for the $\eta_c(2S)$ Dalitz-plot analysis. In addition to the background from $D^0 \to K^0_S K^+ K^-$ (see Sec. III), additional backgrounds involving the spectator K^+ are removed. A significant contribution from $\phi(1020) \to K^+ K^-$ decays is removed by selecting events outside the $1.01 < m(K^+K^-) < 1.03$ GeV mass region, and a small contribution from $D_s^+ \to K^+ K^- \pi^+$ decays is removed in the $\pm 2\sigma$ ($\sigma = 7.8$ MeV) mass region close to the known D_s^+ mass. Finally, a significant contribution from $D_s^- \to K^0_S K^-$ decays is removed within $\pm 2.5\sigma$ ($\sigma = 7.8$ MeV) from the known D_s^+ mass [3].

Figure 20 shows the resulting $K^0_S K^- \pi^+$ invariant-mass spectrum in the $\eta_c(2S)$ region with the signal [3.61–3.67] GeV and sideband [3.42–3.45] GeV, [3.70–3.73] GeV regions indicated. Table XIII shows the $\eta_c(2S)$ event yields in the signal region, purities and background compositions. Figure 21 shows the $\eta_c(2S)$ Dalitz plot. The distribution is dominated by the $K_0^*(1430)$ resonance with bands due to the $K^*(892)$ resonance originating from background.

The decay of the $\eta_c(2S)$ to $K^0_S K\pi$ is expected to be very similar to that of the η_c, except for the different size of the

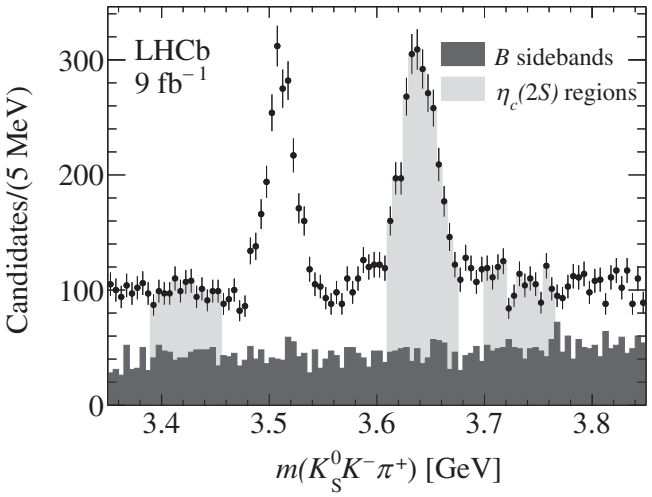

FIG. 20. Invariant $K^0_S K\pi$ mass distribution in the region of the $\eta_c(2S)$ resonance for $B^+ \to K^0_S K^+ K^-\pi^+$. The $\eta_c(2S)$ signal and sideband regions are indicated in light gray, while the incoherent background estimated from the B^+ sidebands is shown in dark gray.

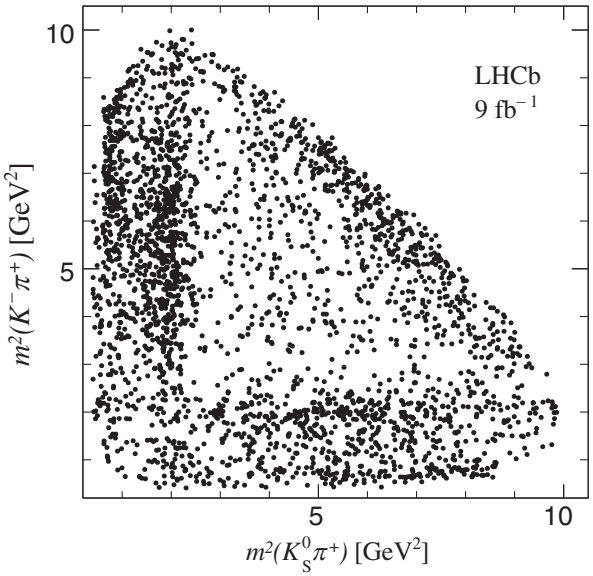

FIG. 21. Dalitz plot of $\eta_c(2S) \to K^0_S K\pi$ decays for the $B^+ \to K^0_S K^+ K^-\pi^+$ sample.

available phase space. Therefore, the Dalitz-plot analysis follows closely the method used for the η_c analysis, except that, due to the limited statistics and the significant background, only the isobar model is used. In addition, all resonance parameters are fixed to those extracted from the η_c isobar model. The efficiency model used for the $\eta_c(2S)$ Dalitz-plot analysis has been described in Sec. VI B 1. The resulting fitted amplitudes and phases are listed in Table XV. The Dalitz-plot projections, together with the fitted background interpolated from the sidebands and the superimposed fit, are shown in Fig. 22. Large interference effects are observed, evidenced by the high value of the sum of the fractions. Systematic uncertainties are evaluated in a similar way as for the η_c Dalitz-plot analysis. In particular, the effect of the efficiency model is evaluated by replacing the fitted efficiencies by two-dimensional binned numerical maps. The effects of the uncertainties on the resonance parameters are evaluated by varying masses and widths by their statistical uncertainties according to a Gaussian distribution and averaging the absolute values of the deviations from the reference fit. The effects of the different sources of systematic uncertainties on the fitted fractions and phases are listed in Table XIV. Interferences between amplitudes are listed in Table XVI for absolute values above 5%.

TABLE XIII. Candidate events in the signal region, purities and B^+ background contributions to the $\eta_c(2S) \to K^0_S K\pi$ Dalitz-plot analysis separated for K^0_S types. The incoherent background fractions f_B in the low and high sidebands refer to the sum of the K^0_{SLL} and K^0_{SDD} data.

K^0_S type	Candidates	Purity [%]	Low f_B [%]	High f_B [%]
K^0_{SLL}	781	63.0 ± 1.7		
K^0_{SDD}	2008	55.2 ± 1.1		
Combined K^0_S			54.0 ± 1.4	55.1 ± 1.4

IX. STUDY OF THE χ_{c1} DECAY TO $K^0_S K\pi$

In this section a study is performed of the χ_{c1} decay in the final states:

$$B^+ \to \chi_{c1} K^+, \quad \chi_{c1} \to K^0_S K^-\pi^+, \tag{24}$$

and

$$B^+ \to \chi_{c1} K^+, \quad \chi_{c1} \to K^0_S K^+\pi^-. \tag{25}$$

The $K^0_S K\pi$ invariant-mass spectrum in the $\chi_{c1} - \eta_c(2S)$ mass region, summed over the K^0_{SLL} and K^0_{SDD} data, is shown in Fig. 23 for the $B^+ \to K^0_S K^+ K^-\pi^+$ and $B^+ \to K^0_S K^+ K^+\pi^-$ final states. The signal region is [3.48–3.54] GeV and the lower and upper sidebands are [3.39–3.45] GeV and [3.70–3.76] GeV, respectively. Table XVII reports the χ_{c1} event yields, purities and background compositions, separated for the K^0_{SLL} and K^0_{SDD} data, for the $B^+ \to K^0_S K^+ K^-\pi^+$ and $B^+ \to K^0_S K^+ K^+\pi^-$ decays.

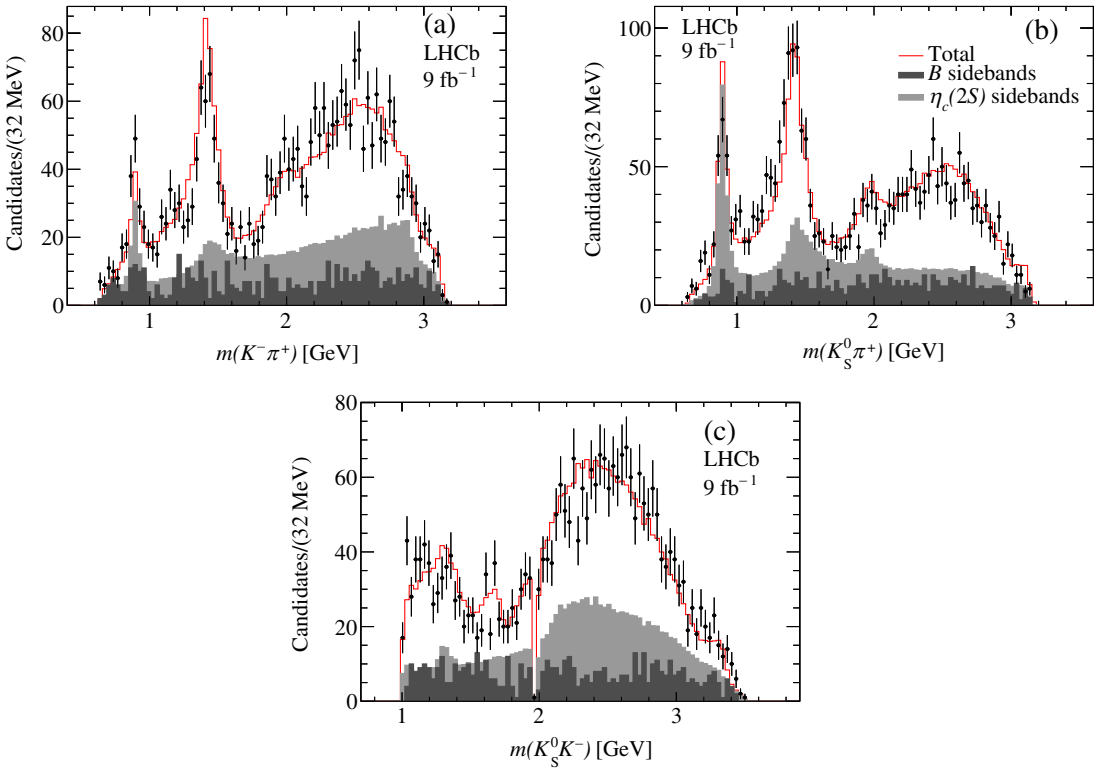

FIG. 22. Dalitz-plot projections of the $\eta_c(2S) \to K^0_S K\pi$ decays from the $B^+ \to K^0_S K^+ K^- \pi^+$ sample. The solid red line shows the fit result, the light gray shaded area is the contribution from the fitted sidebands and the dark shaded gray area is the contribution from the B^+ sidebands. The empty region in the $K^0_S K^-$ invariant-mass projection is due to the removal of the contribution from $D_s^+ \to K^0_S K^-$ decays.

TABLE XIV. Systematic uncertainties on (left) fractional contributions (%) and (right) phases in the $\eta_c(2S)$ Dalitz-plot analysis in $B^+ \to K^0_S K^+ K^- \pi^+$ decay using the isobar model.

Final state	Purity	Par	r	Back	Efficiency	Total	Purity	Par	r	Back	Efficiency	Total
$K_0^*(1430)K$	1.92	1.25	0.17	0.91	3.26	4.1						
$K_2^*(1430)K$	2.47	0.43	1.24	0.86	3.30	4.4	0.06	0.02	0.04	0.02	0.01	0.08
$K_0^*(1950)K$	0.60	0.22	0.37	0.18	0.74	1.1	0.03	0.09	0.08	0.21	0.01	0.24
$a_0(1700)^-\pi^+$	0.32	0.05	0.29	0.13	0.02	0.45	0.18	0.05	0.11	0.87	0.12	0.90
$a_0(1450)^-\pi^+$	0.94	0.04	0.19	0.32	0.19	1.03	0.10	0.04	0.09	0.53	0.09	0.56
$a_2(1750)^-\pi^+$	0.53	0.15	0.42	0.11	0.79	1.05	0.03	0.04	0.08	0.38	0.03	0.39
$\kappa(2600)K$	4.33	3.28	4.97	0.01	2.40	7.74	0.04	0.05	0.04	0.02	0.01	0.08

TABLE XV. Results from the Dalitz-plot analysis of $\eta_c(2S) \to K^0_S K\pi$ in the $B^+ \to K^0_S K^+ K^- \pi^+$ final state using the isobar model.

Final state	Fraction [%]	Phase [rad]
$K_0^*(1430)K$	$25.5 \pm 3.3 \pm 4.1$	0.
$K_2^*(1430)K$	$24.5 \pm 3.3 \pm 4.4$	$3.10 \pm 0.11 \pm 0.08$
$K_0^*(1950)K$	$3.7 \pm 1.3 \pm 1.1$	$-0.82 \pm 0.17 \pm 0.24$
$a_0(1700)^-\pi^+$	$1.7 \pm 1.1 \pm 0.5$	$1.22 \pm 0.32 \pm 0.90$
$a_0(1450)^-\pi^+$	$7.8 \pm 1.9 \pm 1.0$	$1.86 \pm 0.14 \pm 0.56$
$a_2(1750)^-\pi^+$	$4.9 \pm 1.4 \pm 1.1$	$-1.75 \pm 0.15 \pm 0.39$
$\kappa(2600)K$	$124.2 \pm 9.0 \pm 7.7$	$-0.91 \pm 0.10 \pm 0.08$
Sum	$192.3 \pm 10.9 \pm 10.0$	
$\chi^2/\text{ndf} = 578/(591-13) = 1.00$		

TABLE XVI. Fractional interference contributions from the Dalitz plot analysis of the $\eta_c(2S)$ decay in $B^+ \to K^0_S K^+ K^- \pi^+$ decays using the isobar model. Absolute values less than 5% are not listed.

Amplitude 1	Amplitude 2	Fraction [%]
$K_0^*(1430)K$	$\kappa(2600)K$	-23.1 ± 4.7
$K_2^*(1430)K$	$\kappa(2600)K$	-40.3 ± 5.0
$K_0^*(1950)K$	$\kappa(2600)K$	16.0 ± 4.9
$a_0(1700)\pi$	$\kappa(2600)K$	-6.1 ± 1.8
$a_0(1450)\pi$	$\kappa(2600)K$	-21.1 ± 3.0
$a_2(1750)\pi$	$\kappa(2600)K$	-15.8 ± 3.8

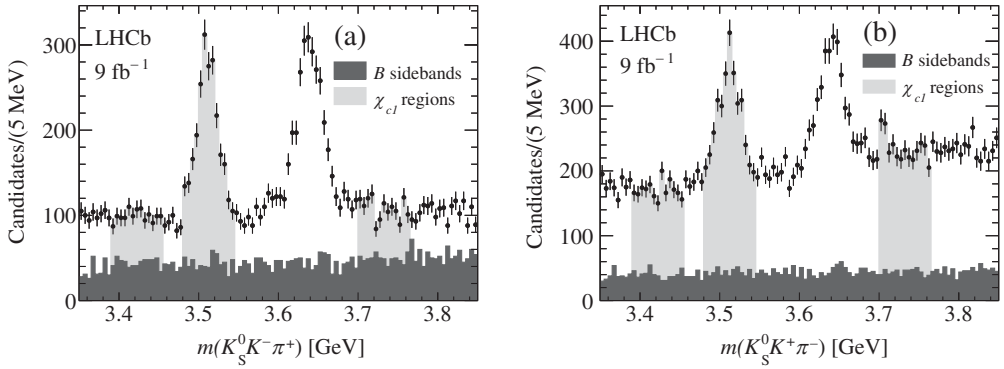

FIG. 23. Invariant $K^0_S K\pi$ mass distribution in the region of the $\chi_{c1}/\eta_c(2S)$ resonances for (a) $B^+ \to K^0_S K^+ K^-\pi^+$ and (b) $B^+ \to K^0_S K^+ K^+\pi^-$ decays. In light gray are indicated the χ_{c1} signal region and sidebands. In dark gray is indicated the incoherent background estimated from the B^+ sidebands.

The χ_{c1} Dalitz plot for $B^+ \to K^0_S K^+ K^-\pi^+$ data, shown in Fig. 24, is dominated by horizontal and vertical bands due to the presence of $K^*(892)$ and $K^*_2(1430)$ resonances. A Dalitz-plot analysis of the χ_{c1} decay to the $K^0_S K\pi$ state is not feasible with the present dataset due to its limited sample size and the high level of background; therefore a simplified approach, similar to that used in Ref. [16], is taken where fits are applied to the $K\pi$ invariant-mass projections. The efficiency distribution as a function of the $K\pi$ and $K^0_S\pi$ invariant masses is computed using the method described in Sec. VI B 1 and expressed in terms of $m_x(K^0_S K)$ and $\cos\theta_\pi$. Each event in the χ_{c1} mass region is weighted by the inverse of the efficiency. The ratios of the unweighted over weighted $K\pi$ and $K^0_S\pi$ invariant-mass distributions are then computed, yielding the efficiency as functions of the $K\pi$ and $K^0_S\pi$ invariant masses. These efficiencies are consistent with being uniform, so no efficiency correction is used in fitting to the $K\pi$ or $K^0_S\pi$ mass projections.

The background contribution is evaluated using the sidebands shown in Fig. 23. For each K^0_S category, the $K\pi$ and $K^0_S\pi$ invariant-mass distributions from the χ_{c1} signal region and from the sidebands are obtained. The $K\pi$ and $K^0_S\pi$ invariant-mass distributions in the sidebands are normalized to the χ_{c1} fitted purity, and subtracted from the invariant-mass spectra in the χ_{c1} signal region, obtaining the distributions shown in Fig. 25. Prominent $K^*(892)$ and $K^*_2(1430)$ resonances are observed. A fit to the $K\pi$ and $K^0_S\pi$ invariant-mass distributions is performed using an empirical and flexible background shape in addition to two relativistic Breit-Wigner functions describing the $K^*(892)$ and $K^*_2(1430)$ resonances with parameters fixed to their known values [3]. The background is parametrized as

$$B(m) = P(m)e^{a_1 m + a_2 m^2} \quad \text{for } m < m_0, \quad \text{and}$$
$$B(m) = P(m)e^{b_0 + b_1 m + b_2 m^2} \quad \text{for } m > m_0, \tag{26}$$

where $P(m)$ is the two-body phase space

$$P(m) = \frac{1}{2m}\sqrt{[m^2-(m_K-m_\pi)^2][m^2-(m_K+m_\pi)^2]} \tag{27}$$

and m_0, a_1, a_2, b_0, b_1, b_2 are free parameters. The two functions and their first derivatives are required to be continuous at $m = m_0$, and this constraint reduces the

TABLE XVII. Candidate events and purities of χ_{c1} for the $B^+ \to K^0_S K^+ K^-\pi^+$ and $B^+ \to K^0_S K^+ K^+\pi^-$ final states separated for the K^0_{SLL} and K^0_{SDD} data. The incoherent background fractions f_B values for the lower and higher sideband regions are computed for the sum of the K^0_{SLL} and K^0_{SDD} data.

B^+ decay mode	K^0_S type	Candidates	Purity [%]	Low f_B [%]	High f_B [%]
$K^0_S K^+ K^-\pi^+$	K^0_{SLL}	695	61.3 ± 1.8		
	K^0_{SDD}	1726	48.4 ± 1.2		
	Combined K^0_S			46.0 ± 2.4	44.9 ± 2.2
$K^0_S K^+ K^+\pi^-$	K^0_{SLL}	1031	34.8 ± 1.5		
	K^0_{SDD}	2443	36.2 ± 1.0		
	Combined K^0_S			23.1 ± 1.2	18.6 ± 0.9

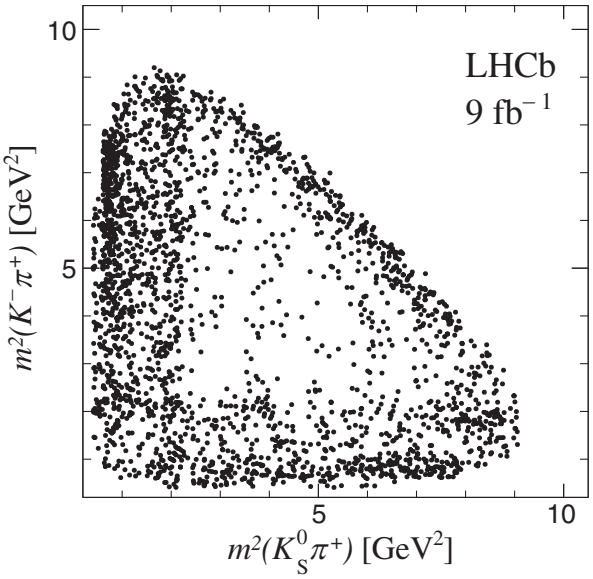

FIG. 24. Dalitz plot of $\chi_{c1} \to K^0_S K^- \pi^+$ decays for the $B^+ \to K^0_S K^+ K^- \pi^+$ sample.

number of freely varying parameters to four. Figure 25 shows the fits to the background-subtracted $K\pi$ and $K^0_S\pi$ invariant-mass distributions in the χ_{c1} signal region for both the $B^+ \to K^0_S K^+ K^- \pi^+$ and $B^+ \to K^0_S K^+ K^+ \pi^-$ data. Table XVIII reports candidate yields and fractional contributions obtained from the fits.

The inverse-variance-weighted averages of the fractional $K^*(892)$ and $K^*_2(1430)$ contributions obtained from the fits to the $B^+ \to K^0_S K^+ K^- \pi^+$ and $B^+ \to K^0_S K^+ K^+ \pi^-$ data are listed in Table XIX. The fractional $K^*(892)$ and $K^*_2(1430)$ contributions are converted into $\chi_{c1} \to K^* \bar{K}$ branching fractions (listed in Table XIX) by multiplying the fractional contributions by the known χ_{c1} branching fraction [3],

$$\mathcal{B}(\chi_{c1} \to \bar{K}^0 K^+ \pi^-) = (7.0 \pm 0.6) \times 10^{-3}, \qquad (28)$$

and correcting for unseen K^* decay modes. A comparison with Ref. [16] shows good agreement, while improving the statistical uncertainties and significances.

Systematic uncertainties are evaluated as follows. The deviations using different BDT classifier selections are evaluated by fitting the lower- and higher-purity datasets and averaging the absolute values of the deviations of the fitted fractions in comparing to the values obtained from the default fit. The differences resulting from the use of the $B^+ \to K^0_S K^+ K^- \pi^+$ or $B^+ \to K^0_S K^+ K^+ \pi^-$ decay modes are also included as systematic uncertainties. The Blatt-Weisskopf radius r entering in the description of the $K^*(892)$ and the $K^*_2(1430)$ resonances, fixed at 1.5 GeV^{-1}, is varied between 0.5 and 2.5 GeV^{-1}.

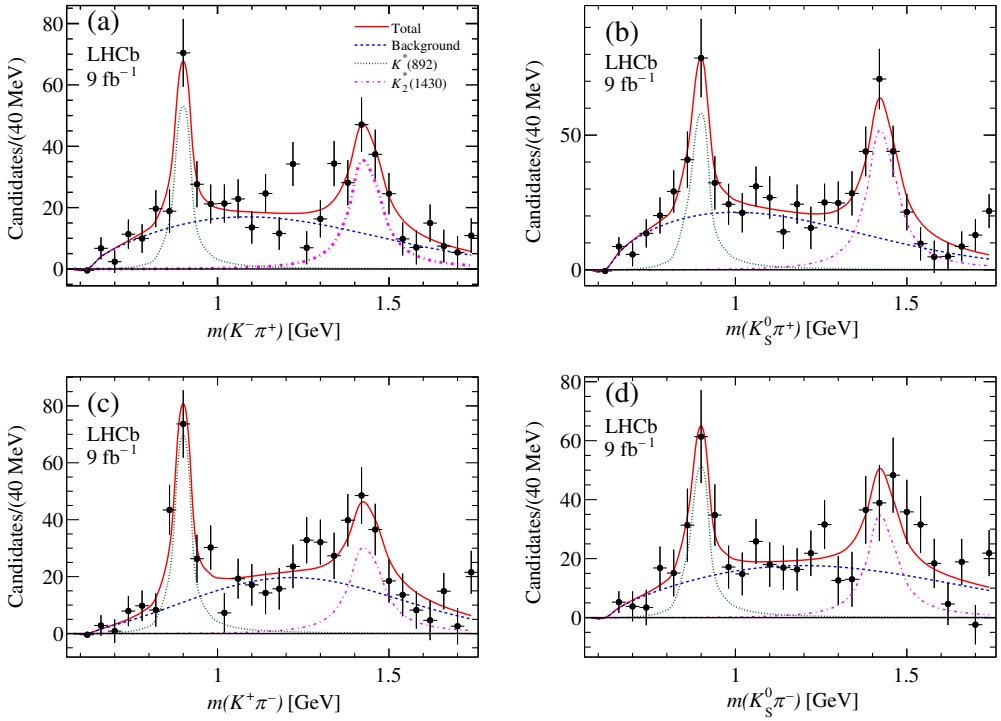

FIG. 25. Background-subtracted $K\pi$ and $K^0_S\pi$ invariant-mass spectra from $\chi_{c1} \to K^0_S K\pi$ decays for the (a)–(b) $B^+ \to K^0_S K^+ K^- \pi^+$ and (c)–(d) $B^+ \to K^0_S K^+ K^+ \pi^-$ data. The results of the fits are overlaid.

TABLE XVIII. Results from the fits to the $K\pi$ and $K^0_S\pi$ background-subtracted invariant-mass distributions in the χ_{c1} decay for the (top) $B^+ \to K^0_S K^+ K^- \pi^+$ and (bottom) $K^0_S K^+ K^+ \pi^-$ data.

Resonance	p value [%]	χ_{c1} Yield	Events	Fraction
$B^+ \to K^0_S K^+ K^- \pi^+$				
$\bar{K}^*(892)^0$	30	1262 ± 54	101 ± 19	0.080 ± 0.015
$\bar{K}^*_2(1430)^0$			140 ± 23	0.111 ± 0.019
$K^*(892)^+$	56		125 ± 26	0.099 ± 0.021
$K^*_2(1430)^+$			188 ± 26	0.149 ± 0.022
$B^+ \to K^0_S K^+ K^+ \pi^-$				
$K^*(892)^0$	64	1244 ± 72	161 ± 22	0.129 ± 0.019
$K^*_2(1430)^0$			138 ± 31	0.111 ± 0.026
$K^*(892)^-$	35		163 ± 29	0.131 ± 0.025
$K^*_2(1430)^-$			163 ± 36	0.131 ± 0.030

TABLE XIX. Inverse-variance-weighted averages of the fractional contributions for χ_{c1} decays to $K^*\bar{K}$ resonances from the $B^+ \to K^0_S K^+ K^- \pi^+$ and $B^+ \to K^0_S K^+ K^+ \pi^-$ final states. The branching fractions of the $\chi_{c1} \to K^0_S K\pi$ decays to $K^*(892)$ and the $K^*_2(1430)$ resonances are also included. The reported uncertainties are statistical, systematic and from the uncertainty on the χ_{c1} branching fraction (see text) [3].

Decay mode	Fraction	Branching fraction ($\times 10^{-3}$)
$\mathcal{B}(\chi_{c1} \to K^*(892)^0 \bar{K}^0)$	$0.099 \pm 0.012 \pm 0.004$	$1.04 \pm 0.13 \pm 0.04 \pm 0.09$
$\mathcal{B}(\chi_{c1} \to K^*_2(1430)^0 \bar{K}^0)$	$0.111 \pm 0.015 \pm 0.005$	$1.17 \pm 0.16 \pm 0.05 \pm 0.10$
$\mathcal{B}(\chi_{c1} \to K^*(892)^+ K^-)$	$0.112 \pm 0.016 \pm 0.013$	$1.18 \pm 0.17 \pm 0.14 \pm 0.10$
$\mathcal{B}(\chi_{c1} \to K^*_2(1430)^+ K^-)$	$0.143 \pm 0.018 \pm 0.006$	$1.61 \pm 0.19 \pm 0.19 \pm 0.14$

X. MEASUREMENT OF THE BRANCHING FRACTIONS OF B^+ DECAYS TO CHARMONIUM RESONANCES

This section is devoted to the extraction of the branching fractions

$$\mathcal{B}(B^+ \to (c\bar{c})X^+), \tag{29}$$

where $c\bar{c} = \eta_c, J/\psi, \chi_{c0}, \chi_{c1}, \chi_{c2}, \eta_c(2S)$ and X indicates a K^+ or a $K^0_S\pi^+$ system. These measurements are performed with respect to the known η_c and J/ψ branching fractions [3]:

$$\mathcal{B}(B^+ \to \eta_c K^+) \cdot \mathcal{B}(\eta_c \to K^0_S K\pi) = (2.7 \pm 0.6) \times 10^{-5}, \tag{30}$$

and

$$\mathcal{B}(B^+ \to J/\psi K^+) \cdot \mathcal{B}(J/\psi \to K^0_S K\pi) = (5.71 \pm 0.52) \times 10^{-6}. \tag{31}$$

The entire dataset, selected as described in Sec. III is used in this section. Efficiency-corrected invariant-mass distributions are obtained by weighting each event by the inverse of the total efficiency described in Sec. VI. Fits are performed to the resulting efficiency-corrected invariant-mass spectra, and the extracted yields of B^+ decays and of various charmonium resonances are used to obtain efficiency-corrected ratios with respect to the η_c and J/ψ resonances. The procedure is performed separately for K^0_{SLL} and K^0_{SDD} data, which are subsequently combined by means of inverse-variance-weighted averages.

Prior to evaluating the $B^+ \to K^0_S K^+ K^- \pi^+$ and $B^+ \to K^0_S K^+ K^+ \pi^-$ candidate yields, it is necessary to subtract all contributions from open-charm production. These are observed in the two- or three-body invariant-mass spectra of the $B \to D_{(s)}X$ decays, where X represents one or two additional particles. The charmed-meson vetoes from the previous sections are not applied. Since open-charm resonances may also be present in the B^+ -meson background, a background subtraction is performed using the normalized B^+ -candidate invariant-mass sidebands. This is achieved by plotting the different two-body or three-body invariant-mass combinations in each of the two sideband regions, with both halves as wide as the B^+ signal region. The resulting invariant-mass distributions are then subtracted from the corresponding ones in the signal region. In

TABLE XX. Resulting yields and total charm fraction from the fits to the four-body, three-body and two-body invariant-mass spectra uncorrected for efficiency for the (top) $B^+ \to K^0_S K^+ K^- \pi^+$ and (bottom) $B^+ \to K^0_S K^+ K^+ \pi^-$ data, separated by K^0_S category. The quoted uncertainties are statistical only.

Resonance	LL	DD
$B^+ \to K^0_S K^+ K^- \pi^+$	27446 ± 228	67515 ± 426
$D_s^+ \to K^0_S K^+$	423 ± 28	994 ± 49
$D^0 \to K^+ K^-$	99 ± 16	185 ± 26
$D^0 \to K^0_S K^- \pi^+$	116 ± 16	319 ± 28
$D^0 \to K^0_S K^- K^+$	4895 ± 71	11627 ± 109
Sum of charm	5533 ± 80	13125 ± 125
Charm fraction (%)	20.2 ± 0.3	19.4 ± 0.2
B^+ no charm	21913 ± 242	54390 ± 444
$B^+ \to K^0_S K^+ K^+ \pi^-$	20950 ± 221	47154 ± 342
$D_s^+ \to K^0_S K^+$	321 ± 17	726 ± 51
$D^0 \to K^- \pi^+$	1553 ± 49	2798 ± 68
$D^0 \to K^0_S K^- \pi^+$	366 ± 24	390 ± 30
Sum of charm	2210 ± 57	3914 ± 90
Charm fraction (%)	10.6 ± 0.3	8.3 ± 0.2
B^+ no charm	18740 ± 228	43240 ± 354

performing fits to the two- or three-body mass spectra, the charmed mesons are described by two Gaussian functions, sharing the same mean, with first- or second-order polynomials used to model the background. Table XX summarizes the fit results for the $B^+ \to K^0_S K^+ K^- \pi^+$ and $B^+ \to K^0_S K^+ K^+ \pi^-$ data, without efficiency corrections.

The efficiency-corrected $K^0_S K \pi$ and $K^+ K^-$ invariant mass spectra are fitted as described in Sec. V to obtain efficiency-corrected yields for η_c, J/ψ (see Fig. 4), χ_{c1}, $\eta_c(2S)$ (see Fig. 5), χ_{c0} and χ_{c2} (see Fig. 6) resonances. The efficiency corrected $K^0_S K^+ K^- \pi^+$ and $K^0_S K^+ K^+ \pi^-$ invariant-mass spectra are fitted as described in Sec. III (see Fig. 2). These yields are used to compute the ratios with respect to the η_c and J/ψ resonance yields, labeled as

$$\mathcal{R}_1(X) = \frac{N(B^+ \to X K^+)}{N(B^+ \to \eta_c K^+)} \tag{32}$$

and

$$\mathcal{R}_2(X) = \frac{N(B^+ \to X K^+)}{N(B^+ \to J/\psi K^+)}, \tag{33}$$

respectively, where X labels the charmonium resonance. Similar expressions are used to calculate the B^+ four-body decays ratios $\mathcal{R}_1(B^+)$ and $\mathcal{R}_2(B^+)$. Table XXI lists the measurements of the efficiency-corrected relative ratios.

The following systematic uncertainties are considered. In fitting for B^+ -candidate and charmonium-resonance yields, the fit model is varied to use Gaussian functions sharing or not sharing the same mean on a quadratic, linear or cubic polynomial background shape. The maximum deviation from the default fit is taken as the systematic uncertainty for each parameter. The open-charm fraction is reevaluated for efficiency-corrected invariant-mass distributions and the difference with respect to the default fit is considered as a systematic uncertainty. In fitting the $K^0_S K \pi$ invariant-mass spectra, the bin size is changed and the background shape is modified from a linear to quadratic function. To evaluate the size of the fit bias on the resonance yields, starting from the reference fits, 400 randomized pseudoexperiments are generated according to Poissionian statistics, having the same sample size as the original ones, and then fitted. The resonance yields are compared with the reference fits. In all cases, the deviations from the reference fits are included as systematic uncertainties. The entire procedure of fitting the invariant-mass spectra and evaluating the relative ratios is repeated dividing the data into the different trigger conditions, TOS and no TOS, whose results are then averaged and compared with the reference fit. All the systematic uncertainties are added in quadrature to calculate the total systematic uncertainty.

TABLE XXI. Ratios of efficiency-corrected intermediate-resonance yields relative to the yield of the (top) η_c and (bottom) J/ψ resonances. The first uncertainty is statistical, the second systematic.

Resonance	$B^+ \to K^0_S K^+ K^- \pi^+$	$B^+ \to K^0_S K^+ K^+ \pi^-$
$\mathcal{R}_1(B^+)$	$4.14 \pm 0.04 \pm 0.25$	$3.40 \pm 0.04 \pm 0.09$
$\mathcal{R}_1(J/\psi)$	$0.201 \pm 0.005 \pm 0.008$	$0.200 \pm 0.005 \pm 0.013$
$\mathcal{R}_1(\chi_{c1})$	$0.082 \pm 0.004 \pm 0.003$	$0.073 \pm 0.004 \pm 0.007$
$\mathcal{R}_1(\eta_c(2S))$	$0.113 \pm 0.005 \pm 0.004$	$0.109 \pm 0.007 \pm 0.016$
$\mathcal{R}_1(\chi_{c0})$	$0.107 \pm 0.006 \pm 0.009$	
$\mathcal{R}_1(\chi_{c2})$	$0.011 \pm 0.003 \pm 0.001$	
$\mathcal{R}_2(B^+)$	$20.6 \pm 0.5 \pm 0.6$	$17.0 \pm 0.4 \pm 0.8$
$\mathcal{R}_2(\eta_c)$	$4.95 \pm 0.12 \pm 0.23$	$5.26 \pm 0.24 \pm 0.29$
$\mathcal{R}_2(\chi_{c1})$	$0.41 \pm 0.02 \pm 0.02$	$0.36 \pm 0.02 \pm 0.04$
$\mathcal{R}_2(\eta_c(2S))$	$0.56 \pm 0.03 \pm 0.02$	$0.55 \pm 0.04 \pm 0.08$
$\mathcal{R}_2(\chi_{c0})$	$0.53 \pm 0.03 \pm 0.04$	
$\mathcal{R}_2(\chi_{c2})$	$0.06 \pm 0.01 \pm 0.01$	

Using the listed ratios it is possible to evaluate the branching fractions as

$$\mathcal{B}_1(X) = f_1 \cdot \mathcal{R}_1(X) \cdot \mathcal{B}(B^+ \to \eta_c K^+) \cdot \mathcal{B}(\eta_c \to K^0_S K \pi) \tag{34}$$

for the η_c mode and

$$\mathcal{B}_2(X) = f_2 \cdot \mathcal{R}_2(X) \cdot \mathcal{B}(B^+ \to J/\psi K^+) \cdot \mathcal{B}(J/\psi \to K^0_S K \pi) \tag{35}$$

TABLE XXII. Measured branching fractions with the η_c resonance as a reference using the (top) $B^+ \to K^0K^+K^-\pi^+$ and (bottom) $B^+ \to K^0K^+K^+\pi^-$ data. The first uncertainty is statistical, the second systematic and the third due to the PDG uncertainty on the $B^+ \to \eta_c K^+$ branching fraction.

Final state	$\mathcal{B}_1$ $(\times 10^{-5})$	PDG $(\times 10^{-5})$
$B^+ \to K^0K^+K^-\pi^+$	$32.28 \pm 0.33 \pm 1.97 \pm 7.17$	
$B^+ \to J/\psi K^+$	$0.543 \pm 0.012 \pm 0.023 \pm 0.121$	0.571 ± 0.052
$B^+ \to \chi_{c1} K^+$	$0.222 \pm 0.010 \pm 0.009 \pm 0.049$	0.194 ± 0.037
$B^+ \to \eta_c(2S) K^+$	$0.306 \pm 0.014 \pm 0.010 \pm 0.068$	$0.34^{+0.23}_{-0.16}$
$B^+ \to K^0K^+K^+\pi^-$	$26.56 \pm 0.31 \pm 0.68 \pm 5.90$	
$B^+ \to J/\psi K^+$	$0.541 \pm 0.014 \pm 0.035 \pm 0.120$	
$B^+ \to \chi_{c1} K^+$	$0.196 \pm 0.011 \pm 0.018 \pm 0.044$	
$B^+ \to \eta_c(2S) K^+$	$0.295 \pm 0.019 \pm 0.042 \pm 0.066$	

TABLE XXIII. Measured branching fractions with the J/ψ resonance as a reference using the (top) $B^+ \to K^0K^+K^-\pi^+$ and (bottom) $B^+ \to K^0K^+K^+\pi^-$ data. The first uncertainty is statistical, the second systematic, the third due to the PDG uncertainty on the $B^+ \to J/\psi K^+$ branching fraction.

Final state	$\mathcal{B}_2$ $(\times 10^{-5})$	PDG $(\times 10^{-5})$
$B^+ \to K^0K^+K^-\pi^+$	$34.01 \pm 0.74 \pm 0.91 \pm 3.10$	
$B^+ \to \eta_c K^+$	$2.83 \pm 0.07 \pm 0.13 \pm 0.26$	2.7 ± 0.6
$B^+ \to \chi_{c1} K^+$	$0.225 \pm 0.011 \pm 0.006 \pm 0.021$	0.194 ± 0.037
$B^+ \to \eta_c(2S) K^+$	$0.327 \pm 0.017 \pm 0.015 \pm 0.030$	$0.34^{+0.23}_{-0.16}$
$B^+ \to K^0K^+K^+\pi^-$	$28.01 \pm 0.68 \pm 1.35 \pm 2.55$	
$B^+ \to \eta_c K^+$	$3.00 \pm 0.14 \pm 0.16 \pm 0.27$	
$B^+ \to \chi_{c1} K^+$	$0.206 \pm 0.012 \pm 0.023 \pm 0.019$	
$B^+ \to \eta_c(2S) K^+$	$0.313 \pm 0.021 \pm 0.044 \pm 0.028$	

TABLE XXIV. Measured branching fractions using (top) the η_c and (bottom) the J/ψ resonance as reference for $B^+ \to K^0K^+K^-\pi^+$ data. The first uncertainty is statistical, the second systematic, the third due to the PDG uncertainty on the $B^+ \to \eta_c K^+$ or $B^+ \to J/\psi K^+$ branching fraction. The PDG reports an upper limit $B^+ \to \chi_{c0} K^{*+} < 0.21 \times 10^{-3}$.

Final state	$\mathcal{B}_1$ $(\times 10^{-3})$	PDG $(\times 10^{-3})$
$B^+ \to \chi_{c0} K^0\pi^+$	$1.38 \pm 0.07 \pm 0.11 \pm 0.32$	
$B^+ \to \chi_{c2} K^0\pi^+$	$0.87 \pm 0.20 \pm 0.08 \pm 0.20$	0.116 ± 0.025
Final state	$\mathcal{B}_2$ $(\times 10^{-3})$	
$B^+ \to \chi_{c0} K^0\pi^+$	$1.45 \pm 0.08 \pm 0.11 \pm 0.16$	
$B^+ \to \chi_{c2} K^0\pi^+$	$0.92 \pm 0.21 \pm 0.08 \pm 0.10$	

for the J/ψ mode, where the f_i are correction factors for unseen decay modes, including K^0 modes. The resulting measured branching fractions are listed in Table XXII ($\mathcal{B}_1$) and Table XXIII ($\mathcal{B}_2$). For the modes involving χ_{c0} and χ_{c2} resonances, listed in Table XXIV, the f_i parameters also include the corrections for their known branching fractions to the K^+K^- state, $(6.05 \pm 0.31) \times 10^{-3}$ and $(1.01 \pm 0.06) \times 10^{-3}$, respectively [3].

The $B^+ \to K^0K^+K^-\pi^+$ and $B^+ \to K^0K^+K^+\pi^-$ branching fractions are measured here for the first time. Tension is found for the $B^+ \to \chi_{c2} K^0\pi^+$ branching fraction with respect to the PDG value [3], measured only in Ref. [47] to be $(0.116 \pm 0.022 \pm 0.012) \times 10^{-3}$ using the $\chi_{c2} \to J/\psi\gamma$ decay mode as a reference with 76.4 ± 14.7 events and a significance of 4.6σ. This measurement differs from that reported here by 2.6σ (3.2σ), using the η_c (J/ψ) meson as a reference and adding the statistical and systematic uncertainties in quadrature.

XI. SUMMARY

A study is presented of $B^+ \to K^0_S K^+K^-\pi^+$ and $B^+ \to K^0_S K^+K^+\pi^-$ decays at proton-proton collision energies of 7, 8 and 13 TeV using the LHCb detector. The $K^0_S K\pi$ invariant-mass spectra from both B^+ decay modes show a

rich spectrum of charmonium resonances. New measurements of the η_c and $\eta_c(2S)$ masses and widths are performed resulting in the best determinations from a single measurement. Branching fractions are measured for B^+ decays to η_c, J/ψ, $\eta_c(2S)$ and χ_{c1} resonances. Evidence is also found for the $B^+ \to \chi_{c2}K^0\pi^+$ decay. Furthermore, the first observation and branching fraction measurement of $B^+ \to \chi_{c0}K^0\pi^+$ decays is reported. The first measurements of $B^+ \to K^0K^+K^-\pi^+$ and $B^+ \to K^0K^+K^+\pi^-$ branching fractions are also given. A Dalitz-plot analysis of $\eta_c \to K^0_S K\pi$ decay is undertaken using both a quasi-model-independent approach for the $K\pi$ S-wave and an isobar-model approach. The $K_0^*(1950) \to K\pi$ resonance is established and its parameters are measured. A new parametrization of the $K\pi$ S-wave is obtained, which includes $K_0^*(1430)$, $K_0^*(1950)$ and broad $\kappa(2600)$ resonances. No evidence for the $\kappa(700)$ resonance is found in η_c decays. The $a_0(1700)$ resonance as well as its decay to $K^0\bar{K}$ are confirmed, and its parameters are measured. The first Dalitz-plot analysis of the $\eta_c(2S) \to K^0_S K\pi$ decay is performed. Finally, branching fractions of $\chi_{c1} \to K^*(892)^0\bar{K}^0$, $\chi_{c1} \to K_2^*(1430)^0\bar{K}^0$, $\chi_{c1} \to K^*(892)^+K^-$ and $\chi_{c1} \to K_2^*(1430)^+K^-$ decays are measured; these measurements are more precise than previous evaluations and correspond to the first observations of the two $\chi_{c1} \to K_2^*(1430)\bar{K}$ decay modes.

ACKNOWLEDGMENTS

We express our gratitude to our colleagues in the CERN accelerator departments for the excellent performance of the LHC. We thank the technical and administrative staff at the LHCb institutes. We acknowledge support from CERN and from the national agencies: CAPES, CNPq, FAPERJ and FINEP (Brazil); MOST and NSFC (China); CNRS/IN2P3 (France); BMBF, DFG and MPG (Germany); INFN (Italy); NWO (Netherlands); MNiSW and NCN (Poland); MEN/IFA (Romania); MICINN (Spain); SNSF and SER (Switzerland); NASU (Ukraine); STFC (United Kingdom); DOE NP and NSF (USA). We acknowledge the computing resources that are provided by CERN, IN2P3 (France), KIT and DESY (Germany), INFN (Italy), SURF (Netherlands), PIC (Spain), GridPP (United Kingdom), CSCS (Switzerland), IFIN-HH (Romania), CBPF (Brazil), Polish WLCG (Poland) and NERSC (USA). We are indebted to the communities behind the multiple open-source software packages on which we depend. Individual groups or members have received support from ARC and ARDC (Australia); Minciencias (Colombia); AvH Foundation (Germany); EPLANET, Marie Skłodowska-Curie Actions and ERC (European Union); A*MIDEX, ANR, IPhU and Labex P2IO, and Région Auvergne-Rhône-Alpes (France); Key Research Program of Frontier Sciences of CAS, CAS PIFI, CAS CCEPP, Fundamental Research Funds for the Central Universities, and Science and Technical Program of Guangzhou (China); GVA, XuntaGal, GENCAT and Program Atracción Talento, CM (Spain); SRC (Sweden); the Leverhulme Trust, the Royal Society and UKRI (United Kingdom).

APPENDIX

The inverse-variance-weighted averages of the numerical values of the $K\pi$ S-wave as a function of the $K\pi$ mass from the Dalitz plot analysis of η_c mesons in $B^+ \to K^0_S K^+K^-\pi^+$ and $B^+ \to K^0_S K^+K^+\pi^-$ decays are listed in Table XXV.

Figures 26–28 show the $K^-\pi^+$, $K^0_S\pi^+$ and $K^0_S K^-$ invariant mass distributions weighted by Legendre polynomial moments computed as functions of $\cos\theta_{K^0_S}$, $\cos\theta_{K^-}$ and

TABLE XXV. Inverse-variance averaged numerical values of the measured $K\pi$ S-wave as a function of the $K\pi$ mass. The first uncertainty is statistical, the second systematic. The values at $K\pi$ mass of 1.425 GeV (in italics) are fixed.

$K\pi$ mass [GeV]	Amplitude	Phase [rad]
0.675	$0.506 \pm 0.071 \pm 0.393$	$2.827 \pm 0.117 \pm 0.202$
0.725	$0.297 \pm 0.065 \pm 0.370$	$2.726 \pm 0.195 \pm 0.562$
0.775	$0.372 \pm 0.041 \pm 0.173$	$2.238 \pm 0.189 \pm 0.734$
0.825	$0.354 \pm 0.045 \pm 0.314$	$2.641 \pm 0.158 \pm 0.729$
0.875	$0.378 \pm 0.036 \pm 0.117$	$2.254 \pm 0.171 \pm 0.492$
0.925	$0.254 \pm 0.041 \pm 0.105$	$0.823 \pm 0.148 \pm 0.362$
0.975	$0.299 \pm 0.036 \pm 0.125$	$0.885 \pm 0.127 \pm 0.230$
1.025	$0.322 \pm 0.032 \pm 0.024$	$0.875 \pm 0.110 \pm 0.031$
1.075	$0.408 \pm 0.032 \pm 0.039$	$0.852 \pm 0.094 \pm 0.427$
1.125	$0.434 \pm 0.030 \pm 0.037$	$0.842 \pm 0.087 \pm 0.138$
1.175	$0.488 \pm 0.029 \pm 0.074$	$0.937 \pm 0.088 \pm 0.317$
1.225	$0.564 \pm 0.029 \pm 0.017$	$0.818 \pm 0.077 \pm 0.220$
1.275	$0.667 \pm 0.027 \pm 0.025$	$1.021 \pm 0.067 \pm 0.217$
1.325	$0.710 \pm 0.024 \pm 0.025$	$1.201 \pm 0.063 \pm 0.113$
1.375	$0.780 \pm 0.021 \pm 0.010$	$1.315 \pm 0.047 \pm 0.095$
1.425	1.000	1.570
1.475	$1.016 \pm 0.022 \pm 0.054$	$1.786 \pm 0.040 \pm 0.049$
1.525	$0.789 \pm 0.020 \pm 0.026$	$1.939 \pm 0.049 \pm 0.028$
1.575	$0.575 \pm 0.019 \pm 0.018$	$2.248 \pm 0.060 \pm 0.181$
1.625	$0.302 \pm 0.022 \pm 0.038$	$2.409 \pm 0.083 \pm 0.179$
1.675	$0.200 \pm 0.023 \pm 0.033$	$1.970 \pm 0.117 \pm 0.301$
1.725	$0.189 \pm 0.022 \pm 0.025$	$1.935 \pm 0.127 \pm 0.544$
1.775	$0.279 \pm 0.019 \pm 0.089$	$1.491 \pm 0.103 \pm 0.324$
1.825	$0.387 \pm 0.019 \pm 0.040$	$1.371 \pm 0.097 \pm 0.123$
1.875	$0.512 \pm 0.022 \pm 0.106$	$1.553 \pm 0.092 \pm 0.154$
1.925	$0.547 \pm 0.021 \pm 0.042$	$1.520 \pm 0.083 \pm 0.105$
1.975	$0.686 \pm 0.024 \pm 0.005$	$1.654 \pm 0.070 \pm 0.197$
2.025	$0.720 \pm 0.025 \pm 0.030$	$1.712 \pm 0.076 \pm 0.129$
2.075	$0.710 \pm 0.026 \pm 0.016$	$1.719 \pm 0.073 \pm 0.081$
2.125	$0.642 \pm 0.026 \pm 0.025$	$1.841 \pm 0.080 \pm 0.172$
2.175	$0.668 \pm 0.028 \pm 0.040$	$1.898 \pm 0.081 \pm 0.203$
2.225	$0.704 \pm 0.029 \pm 0.033$	$1.725 \pm 0.083 \pm 0.190$
2.275	$0.760 \pm 0.035 \pm 0.063$	$1.894 \pm 0.081 \pm 0.348$
2.325	$0.735 \pm 0.040 \pm 0.091$	$1.782 \pm 0.090 \pm 0.346$
2.375	$0.789 \pm 0.050 \pm 0.130$	$1.883 \pm 0.081 \pm 0.339$
2.425	$0.896 \pm 0.058 \pm 0.236$	$2.081 \pm 0.077 \pm 0.329$
2.475	$0.876 \pm 0.070 \pm 0.332$	$2.088 \pm 0.108 \pm 0.483$

$\cos\theta_{\pi^+}$, respectively, from the Dalitz plot analysis of the η_c decay to $K^0_S K\pi$ using the QMI approach to the fit to $B^+ \to K^0_S K^+ K^- \pi^+$ data.

Figure 29 shows the mass projections from the η_c Dalitz plot analysis using the QMI model from $B^+ \to K^0_S K^+ K^+ \pi^-$ data.

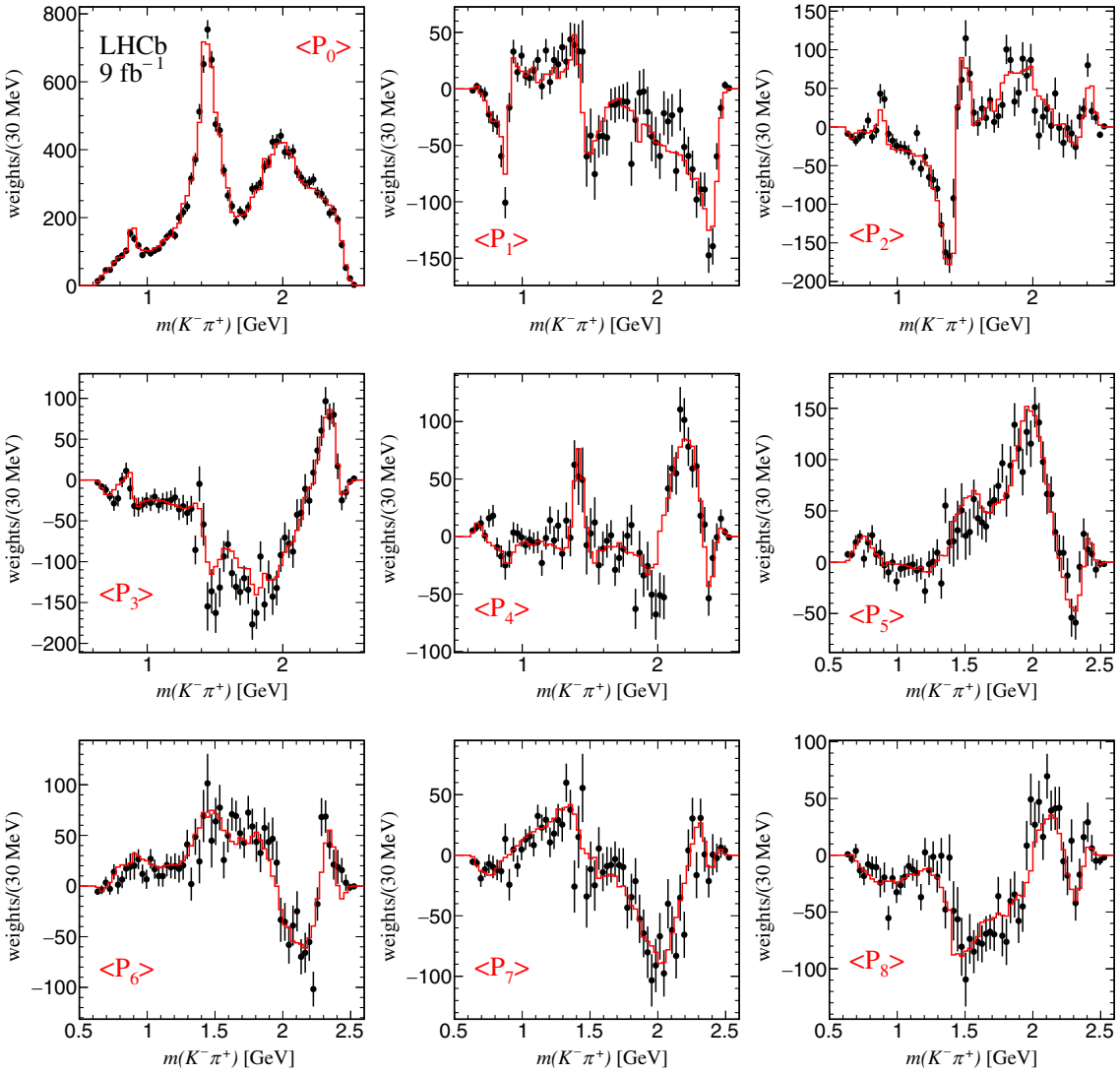

FIG. 26. Projected $K^-\pi^+$ invariant mass spectra weighted by Legendre polynomial moments $P_L(\cos\theta_{K^0_S})$ for $\eta_c \to K^0_S K^-\pi^+$ from $B^+ \to K^0_S K^+ K^-\pi^+$ data. The drawn curves result from the Dalitz plot fit using the QMI method described in the text.

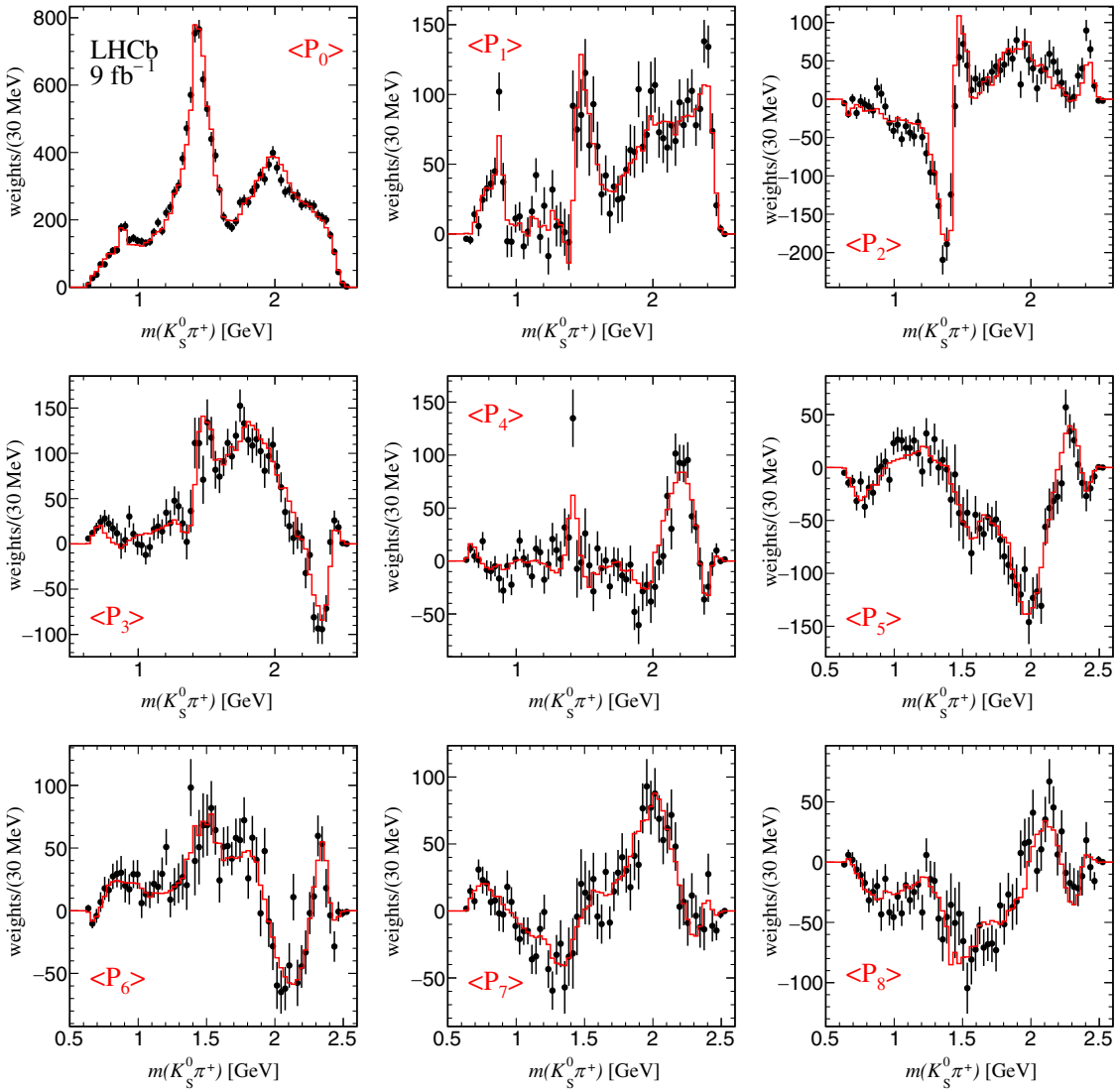

FIG. 27. Projected $K^0_S\pi^+$ invariant mass spectra weighted by Legendre polynomial moments $P_L(\cos\theta_{K^-})$ for $\eta_c \to K^0_S K^-\pi^+$ from $B^+ \to K^0_S K^+ K^-\pi^+$ data. The drawn curves result from the Dalitz plot fit using the QMI method described in the text.

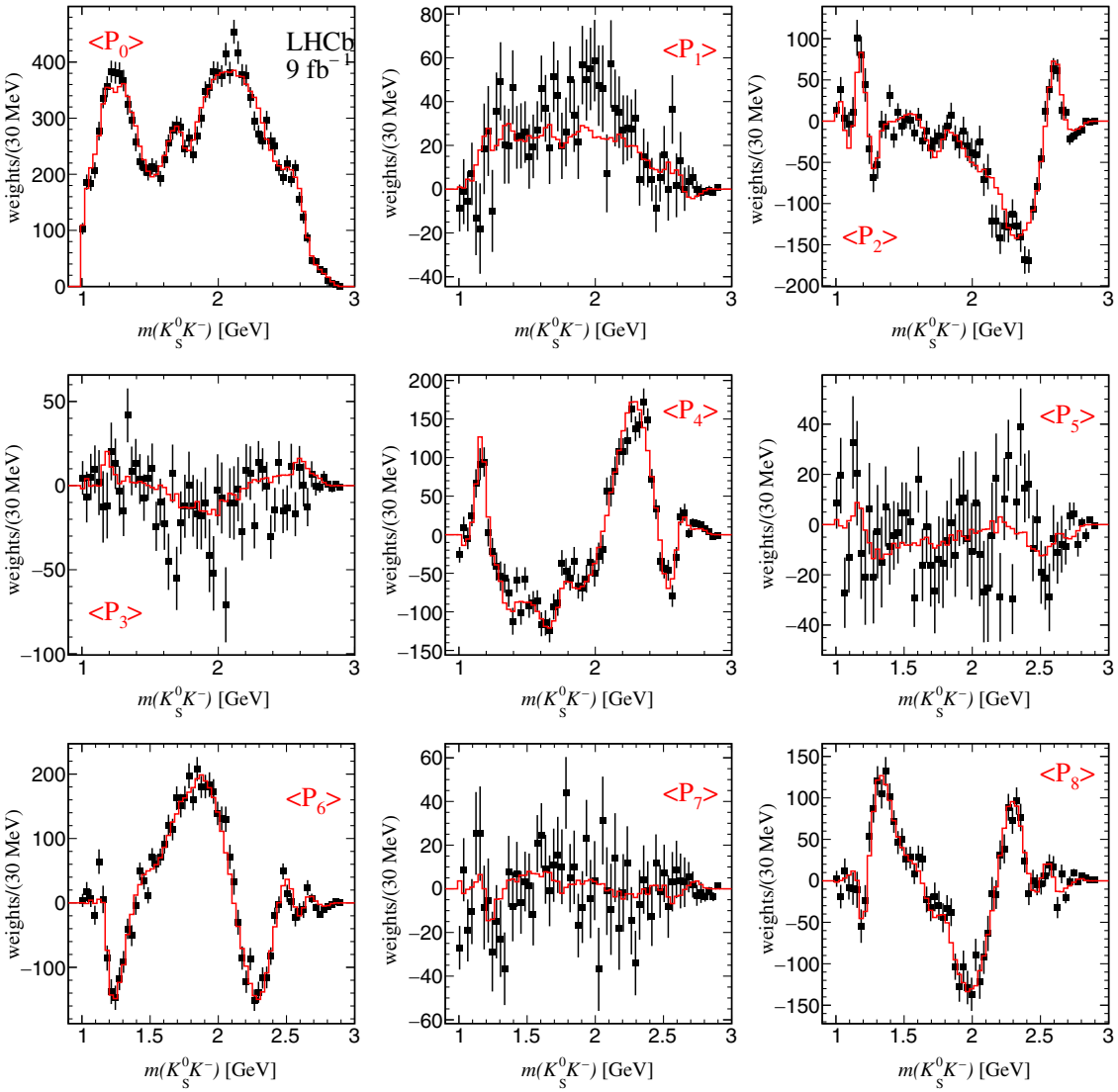

FIG. 28. Projected $K^0_S K^-$ invariant mass spectra weighted by Legendre polynomial moments $P_L(\cos\theta_{\pi^+})$ for $\eta_c \to K^0_S K^-\pi^+$ from $B^+ \to K^0_S K^+ K^-\pi^+$ data. The drawn curves result from the Dalitz plot fit using the QMI method described in the text.

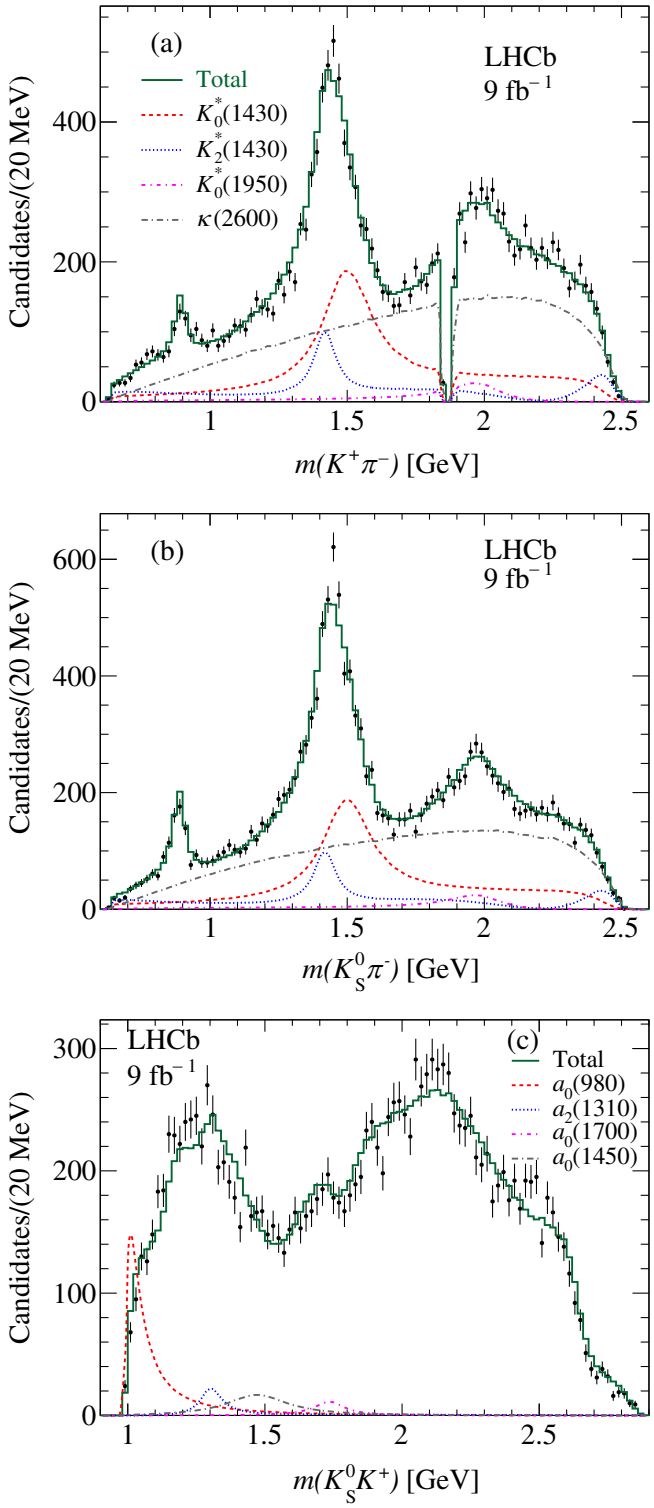

FIG. 29. Fit projections on the (a) $K^+\pi^-$, (b) $K^0_S\pi^-$, and (c) $K^0_SK^+$ invariant mass distributions from the Dalitz-plot analysis of the η_c decay using the isobar model for $B^+ \to K^0_SK^+K^+\pi^-$ data. The curves show the most important resonant contributions. To simplify the plots only resonant contributions relative to that mass projection are shown. The legend in (a) applies also to (b).

[1] M. Neubert and B. Stech, Nonleptonic weak decays of B mesons, Adv. Ser. Dir. High Energy Phys. **15**, 294 (1998).

[2] M. Suzuki, Search of 1P1 charmonium in B decay, Phys. Rev. D **66**, 037503 (2002).

[3] R. L. Workman *et al.* (Particle Data Group), Review of particle physics, Prog. Theor. Exp. Phys. **2022**, 083C01 (2022).

[4] P. Colangelo, F. De Fazio, and T. N. Pham, $B^- \to K^- \chi_{c0}$ decay from charmed meson rescattering, Phys. Lett. B **542**, 71 (2002).

[5] R. Aaij *et al.* (LHCb Collaboration), Model-Independent Observation of Exotic Contributions to $B^0 \to J/\psi K^+ \pi^-$ Decays, Phys. Rev. Lett. **122**, 152002 (2019).

[6] D. Aston *et al.*, A study of $K^- \pi^+$ scattering in the reaction $K^- p \to K^- \pi^+ n$ at 11-GeV/c, Nucl. Phys. **B296**, 493 (1988).

[7] E. M. Aitala *et al.* (E791 Collaboration), Model independent measurement of S-wave $K^- \pi^+$ systems using $D^+ \to K\pi\pi$ decays from Fermilab E791, Phys. Rev. D **73**, 032004 (2006); Phys. Rev. D **74**, 059901(E) (2006).

[8] G. Bonvicini *et al.* (CLEO Collaboration), Dalitz plot analysis of the $D^+ \to K^- \pi^+ \pi^+$ decay, Phys. Rev. D **78**, 052001 (2008).

[9] J. M. Link *et al.* (FOCUS Collaboration), Dalitz plot analysis of the $D^+ \to K^- \pi^+ \pi^+$ decay in the FOCUS experiment, Phys. Lett. B **653**, 1 (2007).

[10] G. 't Hooft, G. Isidori, L. Maiani, A.D. Polosa, and V. Riquer, A theory of scalar mesons, Phys. Lett. B **662**, 424 (2008).

[11] J. P. Lees *et al.* (*BABAR* Collaboration), Measurement of the $I = 1/2$ $K\pi$ $\mathcal{S}$-wave amplitude from Dalitz plot analyses of $\eta_c \to K\bar{K}\pi$ in two-photon interactions, Phys. Rev. D **93**, 012005 (2016).

[12] J. P. Lees *et al.* (*BABAR* Collaboration), Dalitz plot analysis of $\eta_c \to K^+ K^- \eta$ and $\eta_c \to K^+ K^- \pi^0$ in two-photon interactions, Phys. Rev. D **89**, 112004 (2014).

[13] M. Ablikim *et al.* (BESIII Collaboration), Measurement of χ_{cJ} decaying into $\eta' K^+ K^-$, Phys. Rev. D **89**, 074030 (2014).

[14] J. P. Lees *et al.* (*BABAR* Collaboration), Light meson spectroscopy from Dalitz plot analyses of η_c decays to $\eta' K^+ K^-$, $\eta' \pi^+ \pi^-$, and $\eta \pi^+ \pi^-$ produced in two-photon interactions, Phys. Rev. D **104**, 072002 (2021).

[15] M. Ablikim *et al.* (BESIII Collaboration), Observation of an a_0-Like State with Mass of 1.817 GeV in the Study of $D_s^+ \to K_S^0 K^+ \pi^0$ Decays, Phys. Rev. Lett. **129**, 182001 (2022).

[16] M. Ablikim *et al.* (BES Collaboration), Measurements of $\psi(2S)$ decays into $\gamma K\bar{K}\pi$ and $\gamma\eta\pi^+\pi^-$, Phys. Rev. D **74**, 072001 (2006).

[17] B. Aubert *et al.* (*BABAR* Collaboration), Study of B-meson decays to $\eta_c K^{(*)}$, $\eta_c(2S) K^{(*)}$ and $\eta_c \gamma K^{(*)}$, Phys. Rev. D **78**, 012006 (2008).

[18] A. Vinokurova *et al.* (Belle Collaboration), Study of $B^\pm \to K^\pm (K_S K\pi)^0$ decay and determination of η_c and $\eta_c(2S)$ parameters, Phys. Lett. B **706**, 139 (2011).

[19] A. A. Alves Jr. *et al.* (LHCb Collaboration), The LHCb detector at the LHC, J. Instrum. **3**, S08005 (2008).

[20] R. Aaij *et al.* (LHCb Collaboration), LHCb detector performance, Int. J. Mod. Phys. A **30**, 1530022 (2015).

[21] R. Aaij *et al.*, Performance of the LHCb vertex locator, J. Instrum. **9**, P09007 (2014).

[22] R. Aaij *et al.*, The LHCb trigger and its performance in 2011, J. Instrum. **8**, P04022 (2013).

[23] T. Sjöstrand, S. Mrenna, and P. Skands, A brief introduction to PYTHIA 8.1, Comput. Phys. Commun. **178**, 852 (2008); T. Sjöstrand, S. Mrenna, and P. Skands, PYTHIA 6.4 physics and manual, J. High Energy Phys. 05 (2006) 026.

[24] I. Belyaev *et al.*, Handling of the generation of primary events in Gauss, the LHCb simulation framework, J. Phys. Conf. Ser. **331**, 032047 (2011).

[25] D. J. Lange, The EvtGen particle decay simulation package, Nucl. Instrum. Methods Phys. Res., Sect. A **462**, 152 (2001).

[26] N. Davidson, T. Przedzinski, and Z. Was, PHOTOS interface in C++: Technical and physics documentation, Comput. Phys. Commun. **199**, 86 (2016).

[27] J. Allison *et al.* (Geant4 Collaboration), Geant4 developments and applications, IEEE Trans. Nucl. Sci. **53**, 270 (2006); S. Agostinelli *et al.* (Geant4 Collaboration), Geant4: A simulation toolkit, Nucl. Instrum. Methods Phys. Res., Sect. A **506**, 250 (2003).

[28] M. Clemencic, G. Corti, S. Easo, C. R Jones, S. Miglioranzi, M. Pappagallo, and P. Robbe, The LHCb simulation application, Gauss: Design, evolution and experience, J. Phys. Conf. Ser. **331**, 032023 (2011).

[29] L. Breiman, J. H. Friedman, R. A. Olshen, and C. J. Stone, *Classification and Regression Trees* (Wadsworth International Group, Belmont, California, USA, 1984).

[30] Y. Freund and R. E. Schapire, A decision-theoretic generalization of on-line learning and an application to boosting, J. Comput. Syst. Sci. **55**, 119 (1997).

[31] H. Voss, A. Hoecker, J. Stelzer, and F. Tegenfeldt, TMVA—Toolkit for multivariate data analysis with ROOT, Proc. Sci. ACAT2007 (**2007**) 040; A. Hoecker *et al.*, TMVA 4—toolkit for multivariate data analysis with ROOT. Users Guide, arXiv:physics/0703039.

[32] B. P. Roe, H.-J. Yang, J. Zhu, Y. Liu, I. Stancu, and G. McGregor, Boosted decision trees, an alternative to artificial neural networks, Nucl. Instrum. Methods Phys. Res., Sect. A **543**, 577 (2005).

[33] R. Aaij *et al.* (LHCb Collaboration), Measurement of the $\eta_c(1S)$ production cross-section in pp collisions at $\sqrt{s} = 13$ TeV, Eur. Phys. J. C **80**, 191 (2020).

[34] R. Aaij *et al.* (LHCb Collaboration), Precision measurement of D meson mass differences, J. High Energy Phys. 06 (2013) 065.

[35] B. Aubert *et al.* (*BABAR* Collaboration), Observation of $B^0 \to \chi_{c0} K^{*0}$ and evidence for $B^+ \to \chi_{c0} K^{*+}$, Phys. Rev. D **78**, 091101 (2008).

[36] R. Aaij *et al.* (LHCb Collaboration), Amplitude analysis of $B_s^0 \to K_S^0 K^\pm \pi^\mp$ decays, J. High Energy Phys. 06 (2019) 114.

[37] F. James, Monte-Carlo phase space, CERN program library (1968).

[38] S. Kopp *et al.* (CLEO Collaboration), Dalitz analysis of the decay $D^0 \to K^- \pi^+ \pi^0$, Phys. Rev. D **63**, 092001 (2001).

[39] P. del Amo Sanchez *et al.* (*BABAR* Collaboration), Dalitz plot analysis of $D_s^+ \to K^+ K^- \pi^+$, Phys. Rev. D **83**, 052001 (2011).

[40] J. M. Blatt and V. F. Weisskopf, *Theoretical Nuclear Physics* (Springer, New York, 1952).

[41] A. Abele *et al.* (Crystal Barrel Collaboration), $p\bar{p}$ annihilation at rest into $K_L K^+ \pi^-$, Phys. Rev. D **57**, 3860 (1998).

[42] E. M. Aitala *et al.* (E791 Collaboration), Dalitz Plot Analysis of the Decay $D^+ \to K^-\pi^+\pi^+$ and the Study of the $K\pi$ Scalar Amplitudes, Phys. Rev. Lett. **89**, 121801 (2002).
[43] B. Aubert *et al.* (*BABAR* Collaboration), Dalitz plot analysis of the decay $B^\pm \to K^\pm K^\pm K^\mp$, Phys. Rev. D **74**, 032003 (2006).
[44] B. Aubert *et al.* (*BABAR* Collaboration), Measurement of the spin of the $\Xi(1530)$ resonance, Phys. Rev. D **78**, 034008 (2008).
[45] S. S. Wilks, The large-sample distribution of the likelihood ratio for testing composite hypotheses, Ann. Math. Stat. **9**, 60 (1938).
[46] T. A. Armstrong *et al.* (WA76 Collaboration), Study of the centrally produced $\pi\pi$ and $K\bar{K}$ systems at 85-GeV/c and 300-GeV/c, Z. Phys. C **51** (1991) 351.
[47] V. Bhardwaj *et al.* (Belle Collaboration), Inclusive and exclusive measurements of B decays to χ_{c1} and χ_{c2} at Belle, Phys. Rev. D **93**, 052016 (2016).

R. Aaij,[32] A. S. W. Abdelmotteleb,[50] C. Abellan Beteta,[44] F. Abudinén,[50] T. Ackernley,[54] B. Adeva,[40] M. Adinolfi,[48] P. Adlarson,[77] H. Afsharnia,[9] C. Agapopoulou,[13] C. A. Aidala,[78] Z. Ajaltouni,[9] S. Akar,[59] K. Akiba,[32] P. Albicocco,[23] J. Albrecht,[15] F. Alessio,[42] M. Alexander,[53] A. Alfonso Albero,[39] Z. Aliouche,[56] P. Alvarez Cartelle,[49] R. Amalric,[13] S. Amato,[2] J. L. Amey,[48] Y. Amhis,[11,42] L. An,[42] L. Anderlini,[22] M. Andersson,[44] A. Andreianov,[38] M. Andreotti,[21] D. Andreou,[62] D. Ao,[6] F. Archilli,[31,b] A. Artamonov,[38] M. Artuso,[62] E. Aslanides,[10] M. Atzeni,[44] B. Audurier,[79] I. B Bachiller Perea,[8] S. Bachmann,[17] M. Bachmayer,[43] J. J. Back,[50] A. Bailly-reyre,[13] P. Baladron Rodriguez,[40] V. Balagura,[12] W. Baldini,[21,42] J. Baptista de Souza Leite,[1] M. Barbetti,[22,c] R. J. Barlow,[56] S. Barsuk,[11] W. Barter,[52] M. Bartolini,[49] F. Baryshnikov,[38] J. M. Basels,[14] G. Bassi,[29,d] B. Batsukh,[4] A. Battig,[15] A. Bay,[43] A. Beck,[50] M. Becker,[15] F. Bedeschi,[29] I. B. Bediaga,[1] A. Beiter,[62] S. Belin,[40] V. Bellee,[44] K. Belous,[38] I. Belov,[38] I. Belyaev,[38] G. Benane,[10] G. Bencivenni,[23] E. Ben-Haim,[13] A. Berezhnoy,[38] R. Bernet,[44] S. Bernet Andres,[76] D. Berninghoff,[17] H. C. Bernstein,[62] C. Bertella,[56] A. Bertolin,[28] C. Betancourt,[44] F. Betti,[42] Ia. Bezshyiko,[44] J. Bhom,[35] L. Bian,[68] M. S. Bieker,[15] N. V. Biesuz,[21] P. Billoir,[13] A. Biolchini,[32] M. Birch,[55] F. C. R. Bishop,[49] A. Bitadze,[56] A. Bizzeti, M. P. Blago,[49] T. Blake,[50] F. Blanc,[43] J. E. Blank,[15] S. Blusk,[62] D. Bobulska,[53] V. B Bocharnikov,[38] J. A. Boelhauve,[15] O. Boente Garcia,[12] T. Boettcher,[59] A. Boldyrev,[38] C. S. Bolognani,[74] R. Bolzonella,[21,e] N. Bondar,[38,42] F. Borgato,[28] S. Borghi,[56] M. Borsato,[17] J. T. Borsuk,[35] S. A. Bouchiba,[43] T. J. V. Bowcock,[54] A. Boyer,[42] C. Bozzi,[21] M. J. Bradley,[55] S. Braun,[60] A. Brea Rodriguez,[40] N. Breer,[15] J. Brodzicka,[35] A. Brossa Gonzalo,[40] J. Brown,[54] D. Brundu,[27] A. Buonaura,[44] L. Buonincontri,[28] A. T. Burke,[56] C. Burr,[42] A. Bursche,[66] A. Butkevich,[38] J. S. Butter,[32] J. Buytaert,[42] W. Byczynski,[42] S. Cadeddu,[27] H. Cai,[68] R. Calabrese,[21,e] L. Calefice,[15] S. Cali,[23] M. Calvi,[26,f] M. Calvo Gomez,[76] P. Campana,[23] D. H. Campora Perez,[74] A. F. Campoverde Quezada,[6] S. Capelli,[26,f] L. Capriotti,[20] A. Carbone,[20,g] R. Cardinale,[24,h] A. Cardini,[27] P. Carniti,[26,f] L. Carus,[14] A. Casais Vidal,[40] R. Caspary,[17] G. Casse,[54] M. Cattaneo,[42] G. Cavallero,[55,42] V. Cavallini,[21,e] S. Celani,[43] J. Cerasoli,[10] D. Cervenkov,[57] A. J. Chadwick,[54] I. C Chahrour,[78] M. G. Chapman,[48] M. Charles,[13] Ph. Charpentier,[42] C. A. Chavez Barajas,[54] M. Chefdeville,[8] C. Chen,[10] S. Chen,[4] A. Chernov,[35] S. Chernyshenko,[46] V. Chobanova,[40] S. Cholak,[43] M. Chrzaszcz,[35] A. Chubykin,[38] V. Chulikov,[38] P. Ciambrone,[23] M. F. Cicala,[50] X. Cid Vidal,[40] G. Ciezarek,[42] P. Cifra,[42] G. Ciullo,[21,e] P. E. L. Clarke,[52] M. Clemencic,[42] H. V. Cliff,[49] J. Closier,[42] J. L. Cobbledick,[56] V. Coco,[42] J. Cogan,[10] E. Cogneras,[9] L. Cojocariu,[37] P. Collins,[42] T. Colombo,[42] L. Congedo,[19] A. Contu,[27] N. Cooke,[47] I. Corredoira,[40] G. Corti,[42] B. Couturier,[42] D. C. Craik,[44] M. Cruz Torres,[1,i] R. Currie,[52] C. L. Da Silva,[61] S. Dadabaev,[38] L. Dai,[65] X. Dai,[5] E. Dall'Occo,[15] J. Dalseno,[40] C. D'Ambrosio,[42] J. Daniel,[9] A. Danilina,[38] P. d'Argent,[19] J. E. Davies,[56] A. Davis,[56] O. De Aguiar Francisco,[56] J. de Boer,[42] K. De Bruyn,[73] S. De Capua,[56] M. De Cian,[43] U. De Freitas Carneiro Da Graca,[1] E. De Lucia,[23] J. M. De Miranda,[1] L. De Paula,[2] M. De Serio,[19,j] D. De Simone,[44] P. De Simone,[23] F. De Vellis,[15] J. A. de Vries,[74] C. T. Dean,[61] F. Debernardis,[19,j] D. Decamp,[8] V. Dedu,[10] L. Del Buono,[13] B. Delaney,[58] H.-P. Dembinski,[15] V. Denysenko,[44] O. Deschamps,[9] F. Dettori,[27,k] B. Dey,[71] P. Di Nezza,[23] I. Diachkov,[38] S. Didenko,[38] L. Dieste Maronas,[40] S. Ding,[62] V. Dobishuk,[46] A. Dolmatov,[38] C. Dong,[3] A. M. Donohoe,[18] F. Dordei,[27] A. C. dos Reis,[1] L. Douglas,[53] A. G. Downes,[8] P. Duda,[75] M. W. Dudek,[35] L. Dufour,[42] V. Duk,[72] P. Durante,[42] M. M. Duras,[75] J. M. Durham,[61] D. Dutta,[56] A. Dziurda,[35] A. Dzyuba,[38] S. Easo,[51] U. Egede,[63] V. Egorychev,[38] C. Eirea Orro,[40] S. Eisenhardt,[52] E. Ejopu,[56]

S. Ek-In,[43] L. Eklund,[77] M. E Elashri,[59] J. Ellbracht,[15] S. Ely,[55] A. Ene,[37] E. Epple,[59] S. Escher,[14] J. Eschle,[44] S. Esen,[44] T. Evans,[56] F. Fabiano,[27,k] L. N. Falcao,[1] Y. Fan,[6] B. Fang,[11,68] L. Fantini,[72,l] M. Faria,[43] S. Farry,[54] D. Fazzini,[26,f] L. F Felkowski,[75] M. Feo,[42] M. Fernandez Gomez,[40] A. D. Fernez,[60] F. Ferrari,[20] L. Ferreira Lopes,[43] F. Ferreira Rodrigues,[2] S. Ferreres Sole,[32] M. Ferrillo,[44] M. Ferro-Luzzi,[42] S. Filippov,[38] R. A. Fini,[19] M. Fiorini,[21,e] M. Firlej,[34] K. M. Fischer,[57] D. S. Fitzgerald,[78] C. Fitzpatrick,[56] T. Fiutowski,[34] F. Fleuret,[12] M. Fontana,[13] F. Fontanelli,[24,h] R. Forty,[42] D. Foulds-Holt,[49] V. Franco Lima,[54] M. Franco Sevilla,[60] M. Frank,[42] E. Franzoso,[21,e] G. Frau,[17] C. Frei,[42] D. A. Friday,[56] L. F Frontini,[25,m] J. Fu,[6] Q. Fuehring,[15] T. Fulghesu,[13] E. Gabriel,[32] G. Galati,[19,j] M. D. Galati,[32] A. Gallas Torreira,[40] D. Galli,[20,g] S. Gambetta,[52,42] M. Gandelman,[2] P. Gandini,[25] H. G Gao,[6] Y. Gao,[7] Y. Gao,[5] M. Garau,[27,k] L. M. Garcia Martin,[50] P. Garcia Moreno,[39] J. García Pardiñas,[42] B. Garcia Plana,[40] F. A. Garcia Rosales,[12] L. Garrido,[39] C. Gaspar,[42] R. E. Geertsema,[32] D. Gerick,[17] L. L. Gerken,[15] E. Gersabeck,[56] M. Gersabeck,[56] T. Gershon,[50] L. Giambastiani,[28] V. Gibson,[49] H. K. Giemza,[36] A. L. Gilman,[57] M. Giovannetti,[23] A. Gioventù,[40] P. Gironella Gironell,[39] C. Giugliano,[21,e] M. A. Giza,[35] K. Gizdov,[52] E. L. Gkougkousis,[42] V. V. Gligorov,[13,42] C. Göbel,[64] E. Golobardes,[76] D. Golubkov,[38] A. Golutvin,[55,38] A. Gomes,[1,n] S. Gomez Fernandez,[39] F. Goncalves Abrantes,[57] M. Goncerz,[35] G. Gong,[3] I. V. Gorelov,[38] C. Gotti,[26] J. P. Grabowski,[70] T. Grammatico,[13] L. A. Granado Cardoso,[42] E. Graugés,[39] E. Graverini,[43] G. Graziani, A. T. Grecu,[37] L. M. Greeven,[32] N. A. Grieser,[59] L. Grillo,[53] S. Gromov,[38] B. R. Gruberg Cazon,[57] C. Gu,[3] M. Guarise,[21,e] M. Guittiere,[11] P. A. Günther,[17] E. Gushchin,[38] A. Guth,[14] Y. Guz,[5,38,42] T. Gys,[42] T. Hadavizadeh,[63] C. Hadjivasiliou,[60] G. Haefeli,[43] C. Haen,[42] J. Haimberger,[42] S. C. Haines,[49] T. Halewood-leagas,[54] M. M. Halvorsen,[42] P. M. Hamilton,[60] J. Hammerich,[54] Q. Han,[7] X. Han,[17] S. Hansmann-Menzemer,[17] L. Hao,[6] N. Harnew,[57] T. Harrison,[54] C. Hasse,[42] M. Hatch,[42] J. He,[6,o] K. Heijhoff,[32] F. H Hemmer,[42] C. Henderson,[59] R. D. L. Henderson,[63,50] A. M. Hennequin,[58] K. Hennessy,[54] L. Henry,[42] J. H Herd,[55] J. Heuel,[14] A. Hicheur,[2] D. Hill,[43] M. Hilton,[56] S. E. Hollitt,[15] J. Horswill,[56] R. Hou,[7] Y. Hou,[8] J. Hu,[17] J. Hu,[66] W. Hu,[5] X. Hu,[3] W. Huang,[6] X. Huang,[68] W. Hulsbergen,[32] R. J. Hunter,[50] M. Hushchyn,[38] D. Hutchcroft,[54] P. Ibis,[15] M. Idzik,[34] D. Ilin,[38] P. Ilten,[59] A. Inglessi,[38] A. Iniukhin,[38] A. Ishteev,[38] K. Ivshin,[38] R. Jacobsson,[42] H. Jage,[14] S. J. Jaimes Elles,[41] S. Jakobsen,[42] E. Jans,[32] B. K. Jashal,[41] A. Jawahery,[60] V. Jevtic,[15] E. Jiang,[60] X. Jiang,[4,6] Y. Jiang,[6] M. John,[57] D. Johnson,[58] C. R. Jones,[49] T. P. Jones,[50] S. J Joshi,[36] B. Jost,[42] N. Jurik,[42] I. Juszczak,[35] S. Kandybei,[45] Y. Kang,[3] M. Karacson,[42] D. Karpenkov,[38] M. Karpov,[38] J. W. Kautz,[59] F. Keizer,[42] D. M. Keller,[62] M. Kenzie,[50] T. Ketel,[32] B. Khanji,[15] A. Kharisova,[38] S. Kholodenko,[38] G. Khreich,[11] T. Kirn,[14] V. S. Kirsebom,[43] O. Kitouni,[58] S. Klaver,[33] N. Kleijne,[29,d] K. Klimaszewski,[36] M. R. Kmiec,[36] S. Koliiev,[46] L. Kolk,[15] A. Kondybayeva,[38] A. Konoplyannikov,[38] P. Kopciewicz,[34] R. Kopecna,[17] P. Koppenburg,[32] M. Korolev,[38] I. Kostiuk,[32] O. Kot,[46] S. Kotriakhova, A. Kozachuk,[38] P. Kravchenko,[38] L. Kravchuk,[38] M. Kreps,[50] S. Kretzschmar,[14] P. Krokovny,[38] W. Krupa,[34] W. Krzemien,[36] J. Kubat,[17] S. Kubis,[75] W. Kucewicz,[35] M. Kucharczyk,[35] V. Kudryavtsev,[38] E. K Kulikova,[38] A. Kupsc,[77] D. Lacarrere,[42] G. Lafferty,[56] A. Lai,[27] A. Lampis,[27,k] D. Lancierini,[44] C. Landesa Gomez,[40] J. J. Lane,[56] R. Lane,[48] C. Langenbruch,[14] J. Langer,[15] O. Lantwin,[38] T. Latham,[50] F. Lazzari,[29,p] C. Lazzeroni,[47] R. Le Gac,[10] S. H. Lee,[78] R. Lefèvre,[9] A. Leflat,[38] S. Legotin,[38] P. Lenisa,[21,e] O. Leroy,[10] T. Lesiak,[35] B. Leverington,[17] A. Li,[3] H. Li,[66] K. Li,[7] P. Li,[42] P.-R. Li,[67] S. Li,[7] T. Li,[4] T. Li,[66] Y. Li,[4] Z. Li,[62] X. Liang,[62] C. Lin,[6] T. Lin,[51] R. Lindner,[42] V. Lisovskyi,[15] R. Litvinov,[27,k] G. Liu,[66] H. Liu,[6] K. Liu,[67] Q. Liu,[6] S. Liu,[4,6] A. Lobo Salvia,[39] A. Loi,[27] R. Lollini,[72] J. Lomba Castro,[40] I. Longstaff,[53] J. H. Lopes,[2] A. Lopez Huertas,[39] S. López Soliño,[40] G. H. Lovell,[49] Y. Lu,[4,q] C. Lucarelli,[22,c] D. Lucchesi,[28,r] S. Luchuk,[38] M. Lucio Martinez,[74] V. Lukashenko,[32,46] Y. Luo,[3] A. Lupato,[56] E. Luppi,[21,e] A. Lusiani,[29,d] K. Lynch,[18] X.-R. Lyu,[6] R. Ma,[6] S. Maccolini,[15] F. Machefert,[11] F. Maciuc,[37] I. Mackay,[57] V. Macko,[43] L. R. Madhan Mohan,[49] A. Maevskiy,[38] D. Maisuzenko,[38] M. W. Majewski,[34] J. J. Malczewski,[35] S. Malde,[57] B. Malecki,[35,42] A. Malinin,[38] T. Maltsev,[38] G. Manca,[27,k] G. Mancinelli,[10] C. Mancuso,[11,25,m] R. Manera Escalero,[39] D. Manuzzi,[20] C. A. Manzari,[44] D. Marangotto,[25,m] J. M. Maratas,[9,s] J. F. Marchand,[8] U. Marconi,[20] S. Mariani,[42] C. Marin Benito,[39] J. Marks,[17] A. M. Marshall,[48] P. J. Marshall,[54] G. Martelli,[72,l] G. Martellotti,[30] L. Martinazzoli,[42,f] M. Martinelli,[26,f] D. Martinez Santos,[40] F. Martinez Vidal,[41] A. Massafferri,[1] M. Materok,[14] R. Matev,[42] A. Mathad,[44] V. Matiunin,[38] C. Matteuzzi,[26] K. R. Mattioli,[12]

A. Mauri,[55] E. Maurice,[12] J. Mauricio,[39] M. Mazurek,[42] M. McCann,[55] L. Mcconnell,[18] T. H. McGrath,[56] N. T. McHugh,[53] A. McNab,[56] R. McNulty,[18] B. Meadows,[59] G. Meier,[15] D. Melnychuk,[36] S. Meloni,[26,f] M. Merk,[32,74] A. Merli,[25] L. Meyer Garcia,[2] D. Miao,[4,6] H. Miao,[6] M. Mikhasenko,[70,t] D. A. Milanes,[69] E. Millard,[50] M. Milovanovic,[42] M.-N. Minard,[8,a] A. Minotti,[26,f] E. Minucci,[62] T. Miralles,[9] S. E. Mitchell,[52] B. Mitreska,[15] D. S. Mitzel,[15] A. Modak,[51] A. Mödden,[15] R. A. Mohammed,[57] R. D. Moise,[14] S. Mokhnenko,[38] T. Mombächer,[40] M. Monk,[50,63] I. A. Monroy,[69] S. Monteil,[9] G. Morello,[23] M. J. Morello,[29,d] M. P. Morgenthaler,[17] J. Moron,[34] A. B. Morris,[42] A. G. Morris,[10] R. Mountain,[62] H. Mu,[3] E. Muhammad,[50] F. Muheim,[52] M. Mulder,[73] K. Müller,[44] C. H. Murphy,[57] D. Murray,[56] R. Murta,[55] P. Muzzetto,[27,k] P. Naik,[48] T. Nakada,[43] R. Nandakumar,[51] T. Nanut,[42] I. Nasteva,[2] M. Needham,[52] N. Neri,[25,m] S. Neubert,[70] N. Neufeld,[42] P. Neustroev,[38] R. Newcombe,[55] J. Nicolini,[15,11] D. Nicotra,[74] E. M. Niel,[43] S. Nieswand,[14] N. Nikitin,[38] N. S. Nolte,[58] C. Normand,[8,27,k] J. Novoa Fernandez,[40] G. N Nowak,[59] C. Nunez,[78] A. Oblakowska-Mucha,[34] V. Obraztsov,[38] T. Oeser,[14] S. Okamura,[21,e] R. Oldeman,[27,k] F. Oliva,[52] C. J. G. Onderwater,[73] R. H. O'Neil,[52] J. M. Otalora Goicochea,[2] T. Ovsiannikova,[38] P. Owen,[44] A. Oyanguren,[41] O. Ozcelik,[52] K. O. Padeken,[70] B. Pagare,[50] P. R. Pais,[42] T. Pajero,[57] A. Palano,[19] M. Palutan,[23] G. Panshin,[38] L. Paolucci,[50] A. Papanestis,[51] M. Pappagallo,[19,j] L. L. Pappalardo,[21,e] C. Pappenheimer,[59] W. Parker,[60] C. Parkes,[56] B. Passalacqua,[21] G. Passaleva,[22] A. Pastore,[19] M. Patel,[55] C. Patrignani,[20,g] C. J. Pawley,[74] A. Pellegrino,[32] M. Pepe Altarelli,[42] S. Perazzini,[20] D. Pereima,[38] A. Pereiro Castro,[40] P. Perret,[9] K. Petridis,[48] A. Petrolini,[24,h] S. Petrucci,[52] M. Petruzzo,[25] H. Pham,[62] A. Philippov,[38] R. Piandani,[6] L. Pica,[29,d] M. Piccini,[72] B. Pietrzyk,[8] G. Pietrzyk,[11] M. Pili,[57] D. Pinci,[30] F. Pisani,[42] M. Pizzichemi,[26,42,f] V. Placinta,[37] J. Plews,[47] M. Plo Casasus,[40] F. Polci,[13,42] M. Poli Lener,[23] A. Poluektov,[10] N. Polukhina,[38] I. Polyakov,[42] E. Polycarpo,[2] S. Ponce,[42] D. Popov,[6,42] S. Poslavskii,[38] K. Prasanth,[35] L. Promberger,[17] C. Prouve,[40] V. Pugatch,[46] V. Puill,[11] G. Punzi,[29,p] H. R. Qi,[3] W. Qian,[6] N. Qin,[3] S. Qu,[3] R. Quagliani,[43] N. V. Raab,[18] B. Rachwal,[34] J. H. Rademacker,[48] R. Rajagopalan,[62] M. Rama,[29] M. Ramos Pernas,[50] M. S. Rangel,[2] F. Ratnikov,[38] G. Raven,[33] M. Rebollo De Miguel,[41] F. Redi,[42] J. Reich,[48] F. Reiss,[56] C. Remon Alepuz,[41] Z. Ren,[3] P. K. Resmi,[57] R. Ribatti,[29,d] A. M. Ricci,[27] S. Ricciardi,[51] K. Richardson,[58] M. Richardson-Slipper,[52] K. Rinnert,[54] P. Robbe,[11] G. Robertson,[52] E. Rodrigues,[54,42] E. Rodriguez Fernandez,[40] J. A. Rodriguez Lopez,[69] E. Rodriguez Rodriguez,[40] D. L. Rolf,[42] A. Rollings,[57] P. Roloff,[42] V. Romanovskiy,[38] M. Romero Lamas,[40] A. Romero Vidal,[40] J. D. Roth,[78,a] M. Rotondo,[23] M. S. Rudolph,[62] T. Ruf,[42] R. A. Ruiz Fernandez,[40] J. Ruiz Vidal,[41] A. Ryzhikov,[38] J. Ryzka,[34] J. J. Saborido Silva,[40] N. Sagidova,[38] N. Sahoo,[47] B. Saitta,[27,k] M. Salomoni,[42] C. Sanchez Gras,[32] I. Sanderswood,[41] R. Santacesaria,[30] C. Santamarina Rios,[40] M. Santimaria,[23] L. Santoro,[1] E. Santovetti,[31,b] D. Saranin,[38] G. Sarpis,[14] M. Sarpis,[70] A. Sarti,[30] C. Satriano,[30,u] A. Satta,[31] M. Saur,[15] D. Savrina,[38] H. Sazak,[9] L. G. Scantlebury Smead,[57] A. Scarabotto,[13] S. Schael,[14] S. Scherl,[54] A. M. Schertz,[71] M. Schiller,[53] H. Schindler,[42] M. Schmelling,[16] B. Schmidt,[42] S. Schmitt,[14] O. Schneider,[43] A. Schopper,[42] M. Schubiger,[32] N. Schulte,[15] S. Schulte,[43] M. H. Schune,[11] R. Schwemmer,[42] B. Sciascia,[23] A. Sciuccati,[42] S. Sellam,[40] A. Semennikov,[38] M. Senghi Soares,[33] A. Sergi,[24,h] N. Serra,[44] L. Sestini,[28] A. Seuthe,[15] Y. Shang,[5] D. M. Shangase,[78] M. Shapkin,[38] I. Shchemerov,[38] L. Shchutska,[43] T. Shears,[54] L. Shekhtman,[38] Z. Shen,[5] S. Sheng,[4,6] V. Shevchenko,[38] B. Shi,[6] E. B. Shields,[26,f] Y. Shimizu,[11] E. Shmanin,[38] R. Shorkin,[38] J. D. Shupperd,[62] B. G. Siddi,[21,e] R. Silva Coutinho,[62] G. Simi,[28] S. Simone,[19,j] M. Singla,[63] N. Skidmore,[56] R. Skuza,[17] T. Skwarnicki,[62] M. W. Slater,[47] J. C. Smallwood,[57] J. G. Smeaton,[49] E. Smith,[44] K. Smith,[61] M. Smith,[55] A. Snoch,[32] L. Soares Lavra,[9] M. D. Sokoloff,[59] F. J. P. Soler,[53] A. Solomin,[38,48] A. Solovev,[38] I. Solovyev,[38] R. Song,[63] F. L. Souza De Almeida,[2] B. Souza De Paula,[2] B. Spaan,[15,a] E. Spadaro Norella,[25,m] E. Spedicato,[20] J. G. Speer,[15] E. Spiridenkov,[38] P. Spradlin,[53] V. Sriskaran,[42] F. Stagni,[42] M. Stahl,[42] S. Stahl,[42] S. Stanislaus,[57] E. N. Stein,[42] O. Steinkamp,[44] O. Stenyakin,[38] H. Stevens,[15] D. Strekalina,[38] Y. S Su,[6] F. Suljik,[57] J. Sun,[27] L. Sun,[68] Y. Sun,[60] P. N. Swallow,[47] K. Swientek,[34] A. Szabelski,[36] T. Szumlak,[34] M. Szymanski,[42] Y. Tan,[3] S. Taneja,[56] M. D. Tat,[57] A. Terentev,[44] F. Teubert,[42] E. Thomas,[42] D. J. D. Thompson,[47] H. Tilquin,[55] V. Tisserand,[9] S. T'Jampens,[8] M. Tobin,[4] L. Tomassetti,[21,e] G. Tonani,[25,m] X. Tong,[5] D. Torres Machado,[1] D. Y. Tou,[3] C. Trippl,[43] G. Tuci,[6] N. Tuning,[32] A. Ukleja,[36] D. J. Unverzagt,[17] A. Usachov,[33] A. Ustyuzhanin,[38] U. Uwer,[17] V. Vagnoni,[20] A. Valassi,[42] G. Valenti,[20] N. Valls Canudas,[76] M. Van Dijk,[43] H. Van Hecke,[61] E. van Herwijnen,[55] C. B. Van Hulse,[40,v] M. van Veghel,[32]

R. Vazquez Gomez,[39] P. Vazquez Regueiro,[40] C. Vázquez Sierra,[42] S. Vecchi,[21] J. J. Velthuis,[48] M. Veltri,[22,w] A. Venkateswaran,[43] M. Veronesi,[32] M. Vesterinen,[50] D. Vieira,[59] M. Vieites Diaz,[43] X. Vilasis-Cardona,[76] E. Vilella Figueras,[54] A. Villa,[20] P. Vincent,[13] F. C. Volle,[11] D. vom Bruch,[10] V. Vorobyev,[38] N. Voropaev,[38] K. Vos,[74] C. Vrahas,[52] J. Walsh,[29] E. J. Walton,[63] G. Wan,[5] C. Wang,[17] G. Wang,[7] J. Wang,[5] J. Wang,[4] J. Wang,[3] J. Wang,[68] M. Wang,[25] R. Wang,[48] X. Wang,[66] Y. Wang,[7] Z. Wang,[44] Z. Wang,[3] Z. Wang,[6] J. A. Ward,[50,63] N. K. Watson,[47] D. Websdale,[55] Y. Wei,[5] B. D. C. Westhenry,[48] D. J. White,[56] M. Whitehead,[53] A. R. Wiederhold,[50] D. Wiedner,[15] G. Wilkinson,[57] M. K. Wilkinson,[59] I. Williams,[49] M. Williams,[58] M. R. J. Williams,[52] R. Williams,[49] F. F. Wilson,[51] W. Wislicki,[36] M. Witek,[35] L. Witola,[17] C. P. Wong,[61] G. Wormser,[11] S. A. Wotton,[49] H. Wu,[62] J. Wu,[7] K. Wyllie,[42] Z. Xiang,[6] Y. Xie,[7] A. Xu,[5] J. Xu,[6] L. Xu,[3] L. Xu,[3] M. Xu,[50] Q. Xu,[6] Z. Xu,[9] Z. Xu,[6] D. Yang,[3] S. Yang,[6] X. Yang,[5] Y. Yang,[6] Z. Yang,[5] Z. Yang,[60] L. E. Yeomans,[54] V. Yeroshenko,[11] H. Yeung,[56] H. Yin,[7] J. Yu,[65] X. Yuan,[62] E. Zaffaroni,[43] M. Zavertyaev,[16] M. Zdybal,[35] M. Zeng,[3] C. Zhang,[5] D. Zhang,[7] J. Zhang,[6] L. Zhang,[3] S. Zhang,[65] S. Zhang,[5] Y. Zhang,[5] Y. Zhang,[57] Y. Zhao,[17] A. Zharkova,[38] A. Zhelezov,[17] Y. Zheng,[6] T. Zhou,[5] X. Zhou,[7] Y. Zhou,[6] V. Zhovkovska,[11] X. Zhu,[3] X. Zhu,[7] Z. Zhu,[6] V. Zhukov,[14,38] Q. Zou,[4,6] S. Zucchelli,[20,g] D. Zuliani,[28] and G. Zunica[56]

(LHCb Collaboration)

[1]*Centro Brasileiro de Pesquisas Físicas (CBPF), Rio de Janeiro, Brazil*
[2]*Universidade Federal do Rio de Janeiro (UFRJ), Rio de Janeiro, Brazil*
[3]*Center for High Energy Physics, Tsinghua University, Beijing, China*
[4]*Institute Of High Energy Physics (IHEP), Beijing, China*
[5]*School of Physics State Key Laboratory of Nuclear Physics and Technology, Peking University, Beijing, China*
[6]*University of Chinese Academy of Sciences, Beijing, China*
[7]*Institute of Particle Physics, Central China Normal University, Wuhan, Hubei, China*
[8]*Université Savoie Mont Blanc, CNRS, IN2P3-LAPP, Annecy, France*
[9]*Université Clermont Auvergne, CNRS/IN2P3, LPC, Clermont-Ferrand, France*
[10]*Aix Marseille Univ, CNRS/IN2P3, CPPM, Marseille, France*
[11]*Université Paris-Saclay, CNRS/IN2P3, IJCLab, Orsay, France*
[12]*Laboratoire Leprince-Ringuet, CNRS/IN2P3, Ecole Polytechnique, Institut Polytechnique de Paris, Palaiseau, France*
[13]*LPNHE, Sorbonne Université, Paris Diderot Sorbonne Paris Cité, CNRS/IN2P3, Paris, France*
[14]*I. Physikalisches Institut, RWTH Aachen University, Aachen, Germany*
[15]*Fakultät Physik, Technische Universität Dortmund, Dortmund, Germany*
[16]*Max-Planck-Institut für Kernphysik (MPIK), Heidelberg, Germany*
[17]*Physikalisches Institut, Ruprecht-Karls-Universität Heidelberg, Heidelberg, Germany*
[18]*School of Physics, University College Dublin, Dublin, Ireland*
[19]*INFN Sezione di Bari, Bari, Italy*
[20]*INFN Sezione di Bologna, Bologna, Italy*
[21]*INFN Sezione di Ferrara, Ferrara, Italy*
[22]*INFN Sezione di Firenze, Firenze, Italy*
[23]*INFN Laboratori Nazionali di Frascati, Frascati, Italy*
[24]*INFN Sezione di Genova, Genova, Italy*
[25]*INFN Sezione di Milano, Milano, Italy*
[26]*INFN Sezione di Milano-Bicocca, Milano, Italy*
[27]*INFN Sezione di Cagliari, Monserrato, Italy*
[28]*Università degli Studi di Padova, Università e INFN, Padova, Padova, Italy*
[29]*INFN Sezione di Pisa, Pisa, Italy*
[30]*INFN Sezione di Roma La Sapienza, Roma, Italy*
[31]*INFN Sezione di Roma Tor Vergata, Roma, Italy*
[32]*Nikhef National Institute for Subatomic Physics, Amsterdam, Netherlands*
[33]*Nikhef National Institute for Subatomic Physics and VU University Amsterdam, Amsterdam, Netherlands*
[34]*AGH—University of Science and Technology, Faculty of Physics and Applied Computer Science, Kraków, Poland*

[35]*Henryk Niewodniczanski Institute of Nuclear Physics Polish Academy of Sciences, Kraków, Poland*
[36]*National Center for Nuclear Research (NCBJ), Warsaw, Poland*
[37]*Horia Hulubei National Institute of Physics and Nuclear Engineering, Bucharest-Magurele, Romania*
[38]*Affiliated with an institute covered by a cooperation agreement with CERN*
[39]*ICCUB, Universitat de Barcelona, Barcelona, Spain*
[40]*Instituto Galego de Física de Altas Enerxías (IGFAE), Universidade de Santiago de Compostela, Santiago de Compostela, Spain*
[41]*Instituto de Fisica Corpuscular, Centro Mixto Universidad de Valencia—CSIC, Valencia, Spain*
[42]*European Organization for Nuclear Research (CERN), Geneva, Switzerland*
[43]*Institute of Physics, Ecole Polytechnique Fédérale de Lausanne (EPFL), Lausanne, Switzerland*
[44]*Physik-Institut, Universität Zürich, Zürich, Switzerland*
[45]*NSC Kharkiv Institute of Physics and Technology (NSC KIPT), Kharkiv, Ukraine*
[46]*Institute for Nuclear Research of the National Academy of Sciences (KINR), Kyiv, Ukraine*
[47]*University of Birmingham, Birmingham, United Kingdom*
[48]*H.H. Wills Physics Laboratory, University of Bristol, Bristol, United Kingdom*
[49]*Cavendish Laboratory, University of Cambridge, Cambridge, United Kingdom*
[50]*Department of Physics, University of Warwick, Coventry, United Kingdom*
[51]*STFC Rutherford Appleton Laboratory, Didcot, United Kingdom*
[52]*School of Physics and Astronomy, University of Edinburgh, Edinburgh, United Kingdom*
[53]*School of Physics and Astronomy, University of Glasgow, Glasgow, United Kingdom*
[54]*Oliver Lodge Laboratory, University of Liverpool, Liverpool, United Kingdom*
[55]*Imperial College London, London, United Kingdom*
[56]*Department of Physics and Astronomy, University of Manchester, Manchester, United Kingdom*
[57]*Department of Physics, University of Oxford, Oxford, United Kingdom*
[58]*Massachusetts Institute of Technology, Cambridge, Massachusetts, USA*
[59]*University of Cincinnati, Cincinnati, Ohio, USA*
[60]*University of Maryland, College Park, Maryland, USA*
[61]*Los Alamos National Laboratory (LANL), Los Alamos, New Mexico, USA*
[62]*Syracuse University, Syracuse, New York, USA*
[63]*School of Physics and Astronomy, Monash University, Melbourne, Australia (associated with Department of Physics, University of Warwick, Coventry, United Kingdom)*
[64]*Pontifícia Universidade Católica do Rio de Janeiro (PUC-Rio), Rio de Janeiro, Brazil (associated with Universidade Federal do Rio de Janeiro (UFRJ), Rio de Janeiro, Brazil)*
[65]*Physics and Micro Electronic College, Hunan University, Changsha City, China (associated with Institute of Particle Physics, Central China Normal University, Wuhan, Hubei, China)*
[66]*Guangdong Provincial Key Laboratory of Nuclear Science, Guangdong-Hong Kong Joint Laboratory of Quantum Matter, Institute of Quantum Matter, South China Normal University, Guangzhou, China (associated with Center for High Energy Physics, Tsinghua University, Beijing, China)*
[67]*Lanzhou University, Lanzhou, China (associated with Institute Of High Energy Physics (IHEP), Beijing, China)*
[68]*School of Physics and Technology, Wuhan University, Wuhan, China (associated with Center for High Energy Physics, Tsinghua University, Beijing, China)*
[69]*Departamento de Fisica, Universidad Nacional de Colombia, Bogota, Colombia (associated with LPNHE, Sorbonne Université, Paris Diderot Sorbonne Paris Cité, CNRS/IN2P3, Paris, France)*
[70]*Universität Bonn—Helmholtz-Institut für Strahlen und Kernphysik, Bonn, Germany (associated with Physikalisches Institut, Ruprecht-Karls-Universität Heidelberg, Heidelberg, Germany)*
[71]*Eotvos Lorand University, Budapest, Hungary (associated with European Organization for Nuclear Research (CERN), Geneva, Switzerland)*
[72]*INFN Sezione di Perugia, Perugia, Italy (associated with INFN Sezione di Ferrara, Ferrara, Italy)*
[73]*Van Swinderen Institute, University of Groningen, Groningen, Netherlands (associated with Nikhef National Institute for Subatomic Physics, Amsterdam, Netherlands)*
[74]*Universiteit Maastricht, Maastricht, Netherlands (associated with Nikhef National Institute for Subatomic Physics, Amsterdam, Netherlands)*
[75]*Faculty of Material Engineering and Physics, Cracow, Poland (associated with Henryk Niewodniczanski Institute of Nuclear Physics Polish Academy of Sciences, Kraków, Poland)*
[76]*DS4DS, La Salle, Universitat Ramon Llull, Barcelona, Spain (associated with ICCUB, Universitat de Barcelona, Barcelona, Spain)*

[77]*Department of Physics and Astronomy, Uppsala University, Uppsala, Sweden (associated with School of Physics and Astronomy, University of Glasgow, Glasgow, United Kingdom)*
[78]*University of Michigan, Ann Arbor, Michigan, USA (associated with Syracuse University, Syracuse, New York, USA)*
[79]*Departement de Physique Nucleaire (SPhN), Gif-Sur-Yvette, France*

[a]Deceased.
[b]Also at Università di Roma Tor Vergata, Roma, Italy.
[c]Also at Università di Firenze, Firenze, Italy.
[d]Also at Scuola Normale Superiore, Pisa, Italy.
[e]Also at Università di Ferrara, Ferrara, Italy.
[f]Also at Università di Milano Bicocca, Milano, Italy.
[g]Also at Università di Bologna, Bologna, Italy.
[h]Also at Università di Genova, Genova, Italy.
[i]Also at Universidad Nacional Autónoma de Honduras, Tegucigalpa, Honduras.
[j]Also at Università di Bari, Bari, Italy.
[k]Also at Università di Cagliari, Cagliari, Italy.
[l]Also at Università di Perugia, Perugia, Italy.
[m]Also at Università degli Studi di Milano, Milano, Italy.
[n]Also at Universidade de Brasília, Brasília, Brazil.
[o]Also at Hangzhou Institute for Advanced Study, UCAS, Hangzhou, China.
[p]Also at Università di Pisa, Pisa, Italy.
[q]Also at Central South U., Changsha, China.
[r]Also at Università di Padova, Padova, Italy.
[s]Also at MSU—Iligan Institute of Technology (MSU-IIT), Iligan, Philippines.
[t]Also at Excellence Cluster ORIGINS, Munich, Germany.
[u]Also at Università della Basilicata, Potenza, Italy.
[v]Also at Universidad de Alcalá, Alcalá de Henares, Spain.
[w]Also at Università di Urbino, Urbino, Italy.